

Electronic Thesis and Dissertation Repository

9-6-2016 12:00 AM

Fabricating and Characterizing Chalcogenide Thin Films as Light Absorbing Layers in Solar Cells

Daniel Vaccarello, *The University of Western Ontario*

Supervisor: Dr. Zhifeng Ding, *The University of Western Ontario*

A thesis submitted in partial fulfillment of the requirements for the Doctor of Philosophy degree in Chemistry

© Daniel Vaccarello 2016

Follow this and additional works at: <https://ir.lib.uwo.ca/etd>

 Part of the [Analytical Chemistry Commons](#), and the [Materials Chemistry Commons](#)

Recommended Citation

Vaccarello, Daniel, "Fabricating and Characterizing Chalcogenide Thin Films as Light Absorbing Layers in Solar Cells" (2016). *Electronic Thesis and Dissertation Repository*. 4125.
<https://ir.lib.uwo.ca/etd/4125>

This Dissertation/Thesis is brought to you for free and open access by Scholarship@Western. It has been accepted for inclusion in Electronic Thesis and Dissertation Repository by an authorized administrator of Scholarship@Western. For more information, please contact wlsadmin@uwo.ca.

Abstract

Solar cell development has been a focus in energy research, with light-absorbing layers as the key theme. Copper indium disulfide (CuInS_2) and copper zinc tin sulfide ($\text{Cu}_2\text{ZnSnS}_4$ or CZTS) have energy band gaps that are optimal for solar energy conversion. New preparation methods have been developed with practicality, safety, and low costs in mind. The one-pot method developed in this thesis group has been utilized to create nanocrystals that can be used to absorb light and generate current. The use of low temperatures and minimalistic reaction conditions has led to the production of CIS and CZTS nanocrystals that can be made into thin films. In this work, many analytical methods were used to investigate the physical and chemical nature of the synthesized CIS and CZTS nanocrystals to ensure purity and photoactivity. A layer-by-layer approach was used to confirm the optimal configuration for a solar cell physically and chemically. The quality of CIS and CZTS films were assessed by factors such as the production of photocurrent, the band gap, and interfacial chemical reactions. The solar cell layers were examined using a variety of physical, electrochemical and analytical methods in order to determine the effects of the synthesis and deposition on established properties. The electrochemistry of the interface was examined using photoelectrochemical measurements and intensity modulated photocurrent spectroscopy was also performed at the interface to identify relative reaction rates of the photoprocesses. X-ray absorption near-edge, X-ray photoelectron, X-ray diffraction and Raman spectroscopies examined the physical aspects of the films. Insight into the transfer of photogenerated electrons and effects of surface morphology can be elucidated through the combination of these techniques. A systematic approach towards the development of these nanocrystal-based solar cells consisting of CIS or CZTS has shown great progress towards creating low-cost photovoltaics.

Keywords

$\text{Cu}_2\text{ZnSnS}_4$ (CZTS), CuInS_2 (CIS), kesterite, chalcopyrite, chalcogenide, CdS, ZnO, Al-doped ZnO, Al:ZnO, thin films, Solvothermal preparation, chemical bath deposition (CBD), atomic layer deposition (ALD), heterojunctions, photoelectrochemistry, solar cells, photovoltaic cells, solar energy conversion, synchrotron spectroscopy, X-ray absorption near edge structures (XANES), extended X-ray absorption fine structures (EXAFS)

Co-Authorship Statement

The thesis contains the work of three published manuscripts, found in Chapters 2, 3, and 4, while Chapters 5, 6, and 7 represent submitted and in-preparation. Below is a list, by chapter, of the co-authors and their contributions.

Chapter 2: Vaccarello, D.; Tapley, A.; Ding, Z., *RSC Adv.* **2013**, 3, 3512-3515. Experimental approach and design were proposed by ZD and DV. DV synthesized most of the compounds, performed electrochemical analysis and wrote the manuscript. AT provided aid in the synthesis of some of the compounds. The manuscript was edited and finalized by ZD. Reprinted with permission, copyright 2013 Royal Society of Chemistry.

Chapter 3: Vaccarello, D.; Hedges, J.; Tapley, A.; Love, D. A.; Ding, Z., *J. Electroanal. Chem.* **2015**, 738, 35-39. Experimental approach and design were proposed by ZD and DV. DV synthesized most of the compounds, performed electrochemical analysis and wrote the manuscript. JH and AT provided aid in the synthesis of some of the compounds. The manuscript was edited and finalized by ZD. Reprinted with permission, copyright 2015 Elsevier.

Chapter 4: Vaccarello, D.; Liu, L.; Zhou, J.; Sham, T.-K.; Ding, Z., *J. Phys. Chem. C* **2015**, 119, 11922-11928. Experimental approach and design were proposed by ZD and DV. DV synthesized all of the compounds, performed electrochemical analysis and wrote the manuscript. LL and JZ both performed the synchrotron data collecting and provided aid in interpretation. LL performed the preliminary analysis. The manuscript was edited by ZD and TKS and finalized by ZD. Reprinted with permission, copyright 2015 American Chemical Society.

Chapter 5: Vaccarello, D.; Turnbull, M.J.; Yiu, Y.-M.; Sham, T.-K.; Ding, Z., *Submitted* **2016**. Experimental approach and design were proposed by ZD, TK and DV. DV synthesized all of the compounds, performed electrochemical analysis, performed synchrotron analysis and wrote the manuscript. MJT and YMY provided the computational synchrotron files. The manuscript was edited by ZD and TKS and finalized by ZD.

Chapter 6: Vaccarello, D.; Wang, J.; Ding, Z., *In Preparation*. **2016**. Experimental approach and design were proposed by ZD and DV. DV synthesized the compounds, performed

electrochemical and physical analysis and wrote the manuscript. JW performed repeated syntheses. The manuscript was edited and finalized by ZD.

Chapter 7: Vaccarello, D.; Wang, J.; Wang, X.; Ding, Z., *In Preparation*. **2016**. Experimental approach and design were proposed by ZD, XW, and DV. DV and XW co-authored the manuscript. XW performed much of the preliminary basis work of electroplating of CZTS technique. JW performed repeated syntheses. DV refined synthetic approach and added subsequent layers towards completion of a solar device. The manuscript was edited and finalized by ZD.

Acknowledgments

I would like to take this opportunity to thank my supervisor, Dr. Zhifeng Ding. His dedication to science and to teaching are a guiding light in my pursuit towards academic excellence. I will be forever grateful for the opportunities, knowledge, and experiences he has provided me throughout my post-graduate tenure. I appreciate the support from the Electronic Shop and office staff, as well as the funding and scholarship agencies.

Since, I joined Dr. Ding's group I have been privy to have met, collaborated and enjoyed the friendship of all of its members. I would like to say thank you to Jane Stockmann, Kalen Swanick, Amy Tapley, Matthew Turnbull, Kyle Jeffs, Sara Khoshmashrab, Michelle Li, Fraser Filice, Lorenzo Perini and all of the undergraduates whom I had the privilege of helping with their theses. I would also like to thank all those who have had an office in MSA 0205 for their continued patience and help in all aspects of chemistry and life. A thank you to Maxwell Goldman for the continued friendship, the aid in becoming healthier, and for prompting me to seek medical attention, ultimately saving my life.

Special thanks to all of my special friends: Gorman Lam, Kevin Le, Jason Hugh, Nehad Hirmiz, and Duy Le. The memories and fun times we have shared will be stories I may be afraid to tell my children one day, but we wear each and every scar as a badge of honour as gratitude for the enormous smiles we had while achieving them.

My family has been crucial to my development to becoming the person I am today and I will be forever grateful to them for always having my back. My parents were my first teachers, and they still have so much more to teach me no matter how educated I become. I have always felt all my family's love and support in each endeavor I have undertaken.

Words cannot describe the amount of appreciation, acknowledgement and love I have for my wife, Linh Vaccarello. She has been by my side through every major life event and I would not have it any other way. She pushes me to be a better scientist, researcher, and person. She has been my rock and will always be the love of my life. I look forward to achieving every success in life and being by her side for many more milestones.

Table of Contents

Abstract.....	i
Co-Authorship Statement.....	iii
Acknowledgments.....	v
Table of Contents.....	vi
List of Tables.....	xi
List of Figures.....	xii
List of Abbreviations, Symbols, and Nomenclature.....	xvii
1 Introduction.....	1
1.1 The Energy Problem.....	1
1.2 The Sunlight Solution.....	1
1.3 Semiconductors.....	3
1.3.1 Types of Semiconductors.....	4
1.4 Photovoltaics Technologies.....	6
1.5 Thin Film Photovoltaics.....	6
1.5.1 Absorbing Layer.....	7
1.5.2 $\text{Cu}_2\text{ZnSnS}_4$ (CZTS).....	7
1.5.3 CuInS_2 (CIS).....	9
1.5.4 Photoelectrochemistry of Solar Energy Materials.....	10
1.5.5 Synchrotron-Based Spectroscopies.....	14
1.6 Scope of Thesis.....	17
1.7 References.....	20
2 Optimization of $\text{Cu}_2\text{ZnSnS}_4$ Nanocrystal Recipe by means of Photoelectrochemical Measurements.....	27
2.1 Introduction.....	27

2.2	Experimental	28
2.2.1	Nanocrystal Preparation	28
2.2.2	Photoelectrochemical Set-up	29
2.2.3	Characterization	29
2.3	Results and Discussion	29
2.3.1	PECMs and Sample Selection	29
2.3.2	SEM and TEM	31
2.3.3	X-ray Diffraction (XRD)	32
2.3.4	X-ray Photoelectron Spectroscopy (XPS)	34
2.4	Conclusions	36
2.5	References	36
3	Dynamic Aspects of CuInS ₂ Light Absorbing Nanocrystals Thin Films	40
3.1	Introduction	40
3.2	Experimental	41
3.2.1	Nanocrystal Synthesis and PECMs	41
3.2.2	IMPS	42
3.3	Results and Discussion	42
3.3.1	Physical Identification of Films	42
3.3.2	PECMs and Photoreactions	43
3.3.3	IMPS Fitting and Correlation to PECMs	47
3.4	Conclusions	53
3.5	References	54
4	Photoelectrochemical and Physical Insight into Cu ₂ ZnSnS ₄ Nanocrystals Using Synchrotron Spectroscopy	57
4.1	Introduction	57
4.2	Experimental	61

4.2.1	Nanocrystal Preparation.....	61
4.2.2	Photoelectrochemical Set-up	61
4.2.3	Synchrotron Beamlines.....	62
4.2.4	Physical Characterization.....	63
4.3	Results and Discussion	63
4.3.1	Physical and Stoichiometric Evaluation of PECM Response in CZTS Thin Films	63
4.3.2	Zn L ₃ -Edge.....	66
4.3.3	N K-edge.....	68
4.3.4	S K-edge.....	71
4.4	Conclusions.....	75
4.5	References.....	76
5	Probing the CZTS/CdS Heterojunction Utilizing Photoelectrochemistry and X-ray Absorption Spectroscopy	81
5.1	Introduction.....	81
5.2	Experimental.....	84
5.2.1	CZTS Film Preparation.....	84
5.2.2	Chemical Bath Deposition of CdS Films.....	85
5.2.3	Post-Process Annealing	86
5.2.4	Photoelectrochemical Measurements.....	87
5.2.5	XANES and EXAFS Analysis.....	87
5.3	Results and Discussion	89
5.3.1	PECMs	89
5.3.2	EXAFS Analysis.....	92
5.3.3	EXAFS Modelling	93
5.3.4	Post-Process Annealing and L-edge EXAFS.....	97

5.3.5	Copper K- and L-Edge Analysis.....	102
5.4	Conclusions.....	105
5.5	References.....	106
6	Electrophoretically Deposited $\text{Cu}_2\text{ZnSnS}_4$ Thin Films as a Light Absorbing Layer in Solar Cells	112
6.1	Introduction.....	112
6.2	Experimental.....	114
6.2.1	CZTS Film Preparation.....	114
6.2.2	Chemical Bath Deposition (CBD) of CdS Films.....	115
6.2.3	Post-Process Annealing	115
6.2.4	ZnO and Al:ZnO Atomic Layer Deposition	116
6.2.5	Photoelectrochemical Measurements.....	117
6.2.6	Characterization Techniques.....	117
6.3	Results and Discussion	118
6.3.1	PECMs	118
6.3.2	Physical Properties of CZTS NC Solar Cells	120
6.3.3	Absorbance Coefficient and Optical Band Gap of CZTS NC Solar Cells.....	125
6.3.4	Electrical Properties of CZTS NC Solar Cells.....	127
6.4	Conclusions.....	130
6.5	References.....	131
7	Fabricating Low-Cost $\text{Cu}_2\text{ZnSnS}_4$ Thin Films Through Galvanostatic Electroplating and Sulfurization for Solar Cells	135
7.1	Introduction.....	136
7.2	Experimental.....	138
7.2.1	Sample Preparation	138
7.2.2	Sulfurization.....	140

7.2.3	CdS, ZnO, and Al:ZnO Deposition.....	140
7.2.4	Characterization of Metallic Precursors and CZTS Films	141
7.2.5	J-V Curve	141
7.3	Results and Discussion	142
7.3.1	PECM Characterization	142
7.3.2	Raman Spectroscopy of CZTS Films	144
7.3.3	CZTS X-ray Diffraction Patterns.....	146
7.3.4	Absorbance Coefficient and Optical Band Gap.....	148
7.3.5	Solar Cell Construction.....	149
7.4	Conclusions.....	151
7.5	References.....	151
8	Concluding Remarks and Future Works	156
8.1	References.....	161
	Appendices.....	163
	Curriculum Vitae	166

List of Tables

Table 3.1 Average IMPS measurement ratios and their standard deviations for constants of photocurrent across all concentrations of MV^{2+}	49
Table 4.1 Curve fitting analysis of peak positions, widths and areas for the first two peaks at the edge jump.....	75
Table 6.1 Measurement statistics for ITO/CZTS/ZnO/AZO/Ag solar cell devices	129
Table 7.1 Metallic film compositions	143
Table 7.2 Measurement statistics for Mo/CZTS/CdS/ZnO/AZO/Ag solar devices	150

List of Figures

Figure 1.1 The spectral irradiance of a photon at different positions along its path to the earth....	3
Figure 1.2 Band diagrams for a) an intrinsic semiconductor b) a p-type semiconductor c) an n-type semiconductor p-n Junction	5
Figure 1.3 Schematic band diagram of a p-n junction	5
Figure 1.4 Schematic representation of common thin film PV construction.....	7
Figure 1.5 Kesterite crystal structure unit cell of CZTS	8
Figure 1.6 Chalcopyrite crystal structure unit cell for CuInS ₂	10
Figure 1.7 IMPS transients for characteristic rates of product separation and recombination	13
Figure 1.8 Illustrative X-ray absorption spectrum of a transition metal atom.....	15
Figure 1.9 Exemplar metal X-ray absorption edge showing defined regions of analysis	16
Figure 2.1 Current density-potential curves of D70 and A50 during PECMs (top and bottom). The dashed curves are the LSVs in the dark for the two samples.	31
Figure 2.2 SEM with TEM inset of sample a) D70 and sample b) A50.....	32
Figure 2.3 XRD patterns of D70 and A50 compared to JCPDS cards of CZTS, CuS, Cu ₂ SnS ₄ , Cu ₂ S and ZnS	33
Figure 2.4 XPS spectra for D70 (solid lines) and A50 (broken lines). a) 2p _{3/2} Cu peaks, b) 2p _{3/2} Zn peaks, c) 3d _{5/2} Sn peaks and d) 2p _{3/2} S peaks.	35
Figure 3.1 SEM image of a CIS sample dropcast on ITO-PET.....	43
Figure 3.2 Linear sweep voltammograms of CuInS ₂ under alternative illumination, in solutions of a) 0.010 M, b) 0.025 M, c) 0.050 M and d) 0.100 M MV ²⁺ containing 0.1 M KCl. A scan rate of 5 mV/s was used with 1/3 Hz chopped light	44

Figure 3.3 Virtual equivalent electronic circuit of a resistor and capacitor in series used for theoretical calculations.....	48
Figure 3.4 Complex representation of the IMPS data for the CuInS ₂ nanocrystal film in (a) 0.010 M MV ²⁺ , (b) 0.025 M MV ²⁺ , (c) 0.050 M MV ²⁺ , and (d) 0.100 M MV ²⁺ solutions at various applied potentials. The solid lines are the fitted results according to the theoretical calculations	50
Figure 3.5 Graphical representation of the correlational relationship between PECM transients and the IMPS data collected at different applied potentials	53
Figure 4.1 Kesterite CZTS lattice with an I4 space group	59
Figure 4.2 2-mercapto-5-n-propylpyrimidine capping ligand structure	61
Figure 4.3 a) Exemplar PECM photoresponse transients of hp- and lp-CZTS NC films in a linear potential sweep under chopped illumination; and b) ternary contour plot representing the percentages of copper, tin and zinc with respect to the photocurrent of the resultant nanocrystals. The contour is a polynomial interpolation of the data points	64
Figure 4.4 SEM images of (a) hp-CZTS and (b) lp-CZTS	66
Figure 4.5 Zn L3-edge XANES (FY) of lp-CZTS and hp-CZTS in comparison with ZnS	67
Figure 4.6 N K-edge XANES of lp-CZTS, hp-CZTS and MPP. Solid lines: TEY; dashed lines: FY. The spectra are offset vertically for clarity	69
Figure 4.7 S K-edge XANES of lp-CZTS and hp-CZTS in comparison with a series of sulfide references and the capping ligand MPP. The spectra are normalized to unity edge jump and offset vertically for clarity	73
Figure 4.8 Curve fitting results of a) hp-CZTS, b) lp-CZTS and c) MPP overlaid on top of XANES data of S K-edge. The first two peaks are relevant of which the parameters are listed in Table 4.1	75

Figure 5.1 Schematic representation of furnace set-up for post processing. A three-way valve connects the quartz tube to an Ar inlet and a Drierite filled vacuum flask. The outlet is connected to a liquid nitrogen-filled cold trap before entering a vacuum 86

Figure 5.2 PECMs of a CZTS thin film on FTO (black) and CZTS/CdS heterojunction (red). Cathodic reduction of MV^{2+} with higher negative potential reduces with CdS addition and recombination after the photoexcitation can be seen through the sharp decrease in photoresponse 91

Figure 5.3 Zn K-edge data for CZTS (black) and CZTS/CdS (red) thin films a) near-edge normalized absorption profiles with extended absorption fine structures (inset). b) Absorption energies converted into k^3 -space c) R space profiles of the thin films obtained after Fourier transforming using a Hanning window over k-range of 3 to 11, d) and back transformed k-space 93

Figure 5.4 Athena fitting for Zn K-edges of CZTS thin films (red). Fitting was performed with a theoretically pure kesterite crystal (blue) over the windowed area (gray)..... 94

Figure 5.5 Athena fitting for Zn K-edges of CZTS/CdS thin films (red). Fitting was performed with a theoretically pure kesterite crystal in addition to an $-OH_2$ coordination (blue) over the windowed period (gray). The graphs correspond to the a) back transformed k-space and b) R-space of the extended fine structures, respectively 95

Figure 5.6 Schematic diagram of CBD-CdS Growth mechanism and possible Zn-OH/OH₂ coordination. 1) adsorption of CdSO₄ to CZTS in solution 2) $-OH$ substitution 3) formation of metastable dihydroxothiurea-cadmium complex 4) $-OH/OH_2$ co-ordination of Zn 5) formation of CdS 6) CdS deposition on top of the CZTS film..... 97

Figure 5.7 Comparative PECMs for different post-processing steps. After CdS addition the general trend is for the photocurrent to decrease. This is apparent with films deposited using a) only EPD and b) EPD with annealing (denoted by subscript a). Photocurrent returned consistently after a post-CBD annealing step 99

Figure 5.8 Zn L_{3,2}-edge for CZTS thin films. The addition of a CdS layer decreases the intensity of the absorption peak as well as changes the shape of the near-edge absorption. The return in sharpness occurs after annealing in samples that were a) not annealed before CdS and b) samples that were annealed before the CdS addition 101

Figure 5.9 Cu K-edge data for CZTS (black) and CZTS/CdS (red) thin films a) extended absorption fine structures. b) Absorption energies converted into k³-space c) R space profiles of the thin films obtained after Fourier transforming using a Hanning window over k-range of 3 to 11, d) and k-space 103

Figure 5.10 Cu L_{3,2}-edge for CZTS thin films. The addition of a CdS layer decreases the intensity of the absorption peak as well as changes the shape of the near-edge absorption. The return in sharpness occurs after annealing in samples that were a) not annealed before the CdS addition 104

Figure 6.1 Photocurrent response of CZTS NC thin films (black) and the annealed CZTS/CdS thin films (red) along a linear sweep in potential with chopped light 119

Figure 6.2 XRD pattern of EPD CZTS NC thin films (black) on FTO and NC CZTS powder (red). The JCPDS # 026-0575 shows the reference pattern obtained for pure phase kesterite CZTS (blue) 121

Figure 6.3 a) a 25 x 25 μm contour map of summed normalized Raman intensities between 334 and 342 cm⁻¹. b) Raman spectra of highest and lowest normalized Raman intensities from the map. The lowest summed intensity (blue) and highest (black) correspond to Spot 1 and 2 respectively 123

Figure 6.4 a) SEM cross-section of an FTO/CZTS/CdS/ZnO/AZO thin film solar cell b) O K_{α1} map c) Cu L_{α1,2} map d) Zn L_{α1,2} map e) Sn L_{α1} map and f) S K_{α1} map..... 124

Figure 6.5 a) Absorption coefficient of the CZTS NC thin film deposited onto FTO using EPD b) Tauc plot for optical band gap measurement (black) and linear extrapolation between 1.7 and 2.1 eV (red) 126

Figure 6.6 1/C² vs. potential plot obtained from a C-V measurement..... 128

Figure 6.7 J-V curve of an ITO/CZTS/CdS/ZnO/AZO/Ag solar cell device	129
Figure 7.1 PECMs of CZTS samples with different stoichiometries	144
Figure 7.2 a) Average Raman spectra of CZTS1 b) Raman spectra of CZTS3-Sn taken from flat areas (black) versus protrusions (red)	145
Figure 7.3 XRD patterns of Cu-rich CZTS (red), Cu-poor CZTS (black), and kesterite CZTS reference pattern JCPDS 026-0575 (red)	147
Figure 7.4 a) The plots of absorbance as a function of wavelength and $(\alpha h\nu)^2$ vs. $h\nu$ of sulfurized CZTS film at 500 °C with linear extrapolation fit	149
Figure 7.5 J–V characteristic of a CZTS thin film solar cell	150

List of Abbreviations, Symbols, and Nomenclature

2a	Wyckoff position 2a in $I\bar{4}$ space group
2b	Wyckoff position 2b in $I\bar{4}$ space group
2c	Wyckoff position 2c in $I\bar{4}$ space group
2d	Wyckoff position 2d in $I\bar{4}$ space group
8g	Wyckoff position 8g in $I\bar{4}$ space group
\emptyset	glass diameter
α	absorption coefficient
$\beta_{1/2}$	full width at half maximum
ϵ_0	permittivity of free space
ϵ_S	dielectric constant for CZTS
η	efficiency
Λ	wavelength
τ	electron lifetime
Ω	angular frequency
Ω/square	ohms per square
$\mu(E)$	normalized X-ray absorption energy
μA	microamperes
μm	micrometres
μL	microlitres
μ_n	electron mobility
A	area
a	unit cell parameter a
A	absorbance
Å	angstrom
A	symmetric Raman vibrational mode
AC	alternating current
acac	acetylacetonate
A_{e^-}	the electron of an absorber
A_{h^+}	the hole of an absorber
Al:ZnO	aluminum-doped zinc oxide
ALD	atomic layer deposition
AM 1.5D	solar energy spectrum filter
AM0	air-mass zero
AM1.5	air-mass 1.5
APS	Advanced Photon Source
atm	atmospheres
AZO	aluminum-doped zinc oxide
b	unit cell parameter b
B	antisymmetric Raman vibrational mode
BA	benzyl alcohol
C	capacitance
c	unit cell parameter c
c	speed of light in a vacuum
CBD	chemical bath deposition

CCD	charge couple device
CdS _a	annealed CdS
cif	crystallographic information file
CIGS	CuIn _x Ga _(1-x) S/Se ₂
CIS	CuInS ₂
CIS _e -	electron of CIS
CIS _h +	hole of CIS
CLS	Canadian Light Source
cts	counts
C-V	capacitance-voltage
CZTS	Cu ₂ ZnSnS ₄
CZTS _a	annealed CZTS
CZTS _e	Cu ₂ ZnSnSe ₄
CZTS _e -	electron of CZTS
CZTS _h +	hole of CZTS
d	diameter
DC	direct current
E	energy
EDX	energy dispersive X-ray spectroscopy
E _f	fermi level energy
E _g	band gap energy
E _o	X-ray absorption edge energy
EPD	electrophoretic deposition
eV	electron volt
EXAFS	extended X-ray absorption fine structures
F	faraday constant
FEFF	automated program for <i>ab initio</i> multiple scattering calculations of EXAFS
FF	fill factor
FTO	fluorine-doped tin oxide
FY	fluorescence yield
g ₁	Gärtner flux
h	Planck's constant
hp-CZTS	high photoresponse CZTS
<i>i</i>	imaginary component of the photocurrent
I ₄	tetragonal crystal space group
IMPS	intensity modulated photocurrent spectroscopy
int	intermediate
I _o	incident photon flux
I _{sc}	short circuit current
ITO	indium-doped tin oxide
i-type	intrinsic semiconductor
j ₁	AC component of the photocurrent
JCPDS	Joint Committee on Powder Diffraction Standards
J-V	current density-voltage
K	crystallite shape factor

k-space	vector space of possible values of momentum for a particle
K-edge	the binding energy of the K shell electron of an atom
kPa	kiloPascal
k_{PS}	rate of product separation
k_R	rate of recombination
kT/q	thermal voltage at room temperature
L ₁ -edge	the binding energy of the L1 shell electron of an atom
L ₂ -edge	the binding energy of the L2 shell electron of an atom
L ₃ -edge	the binding energy of the L3 shell electron of an atom
L _n	diffusion length
lp-CZTS	low photoresponse CZTS
LSV	linear sweep voltammogram
LUMO	lowest unoccupied molecular orbital
M	mass
M ₁ -edge	the binding energy of the M1 shell electron of an atom
M _{2,3} -edge	the binding energy of the M2 and M3 shell electrons of an atom
M _{4,5} -edges	the binding energy of the M4 and M5 shell electrons of an atom
MM	molar mass
MPP	2-mercapto-5-n-propylpyrimidine
MV ²⁺	methyl viologen
MΩ/sq	megaohms per square
NA	numerical aperture
N _a	dopant density
NC	nanocrystal
NCF	nanocrystal film
nm	nanometre
n-type	semiconductor with electron majority carrier
PECM	photoelectrochemical measurement
PET	polyethylene terephthalate
pF	picofarad
p-type	semiconductor with hole majority carrier
PV	photovoltaic
PVD	physical vapour deposition
q	electron charge
Q	charge
R	resistance
R	inter-atomic distance between the absorber and the scatterer
RF	radio frequency
R _S	series resistance
R _{SH}	shunt resistance
R-space	Fourier transformed k-space
SAED	selected area diffraction
sccm	standard cubic centimetres
SCE	saturated calomel electrode
SCR	space charge region
SEM	scanning electron microscopy

SR	synchrotron radiation
TEM	transmission electron microscopy
TEY	total electron yield
UV	ultraviolet
V	potential
V_{bi}	built-in charge
VESTA	visualization for electronic and structural analysis
Vis	visible
V_{oc}	open circuit voltage
W_d	depletion width
XANES	X-ray absorption near edge structures
XRD	X-ray diffraction
z	number of electrons

1 Introduction

1.1 The Energy Problem

The “big picture” motivation for this work is primarily due to the problematic increase in the need for energy. In addition to these problems our primary sources of energy, are heavily based around non-renewable sources. Oil has been predicted to run out in the next 50 years, natural gas in the next 70 years and coal in the next 250.¹ With so many of our main sources of energy becoming scarce, combined with the increased globalization of many countries and markets, the demand for energy will soon exceed the abilities of our current resources.² In order to stop the destruction of the environment as well as have a long term viable source of energy, research must be done into a more inexpensive, clean, and efficient method for harnessing renewable energy, such as solar power. While many other renewable sources of energy exist, they are not all equivalent in terms of scale of energy. Wind energy has the potential to be able to supply the energy demands, however considerable leaps in innovation need to be taken in order for it to be optimized to its full potential.³ Additionally, other sources of energy are first or second order by-products of solar energy, but are unable to meet the demand of energy as single sources. At present, solar energy is one of the only renewable resources that can successfully meet the energy demands of our current global consumption, combined with the ability to increase its current potential for energy conversion, it has a truly bright future.

1.2 The Sunlight Solution

Sunlight is a widely abundant, free source of energy that is always present and is not subject to the variability of the economy. If all the sunlight that hit the earth in one hour

was collected at 100% efficiency, the world's supply of energy for one year would be harnessed; in 20 days it would match the energy currently in the oil, natural gas and coal reserves combined.⁴ The particles that are emitted by sunlight can be described simply as photons. The energy of a photon can vary significantly and is dependent on its wavelength. Solar radiation and its wave-like characteristics are defined by the energy of a photon (E) given by **Equation 1.1**

$$E = \frac{hc}{\lambda} \quad \mathbf{1.1}$$

where h is Planck's constant (6.626×10^{-34} Js), c is the velocity of light (2.998×10^8 m/s) and λ is the photon's wavelength.

The energy from the sun can be harnessed by using photovoltaic devices (PV) or solar cells. PVs make use of semiconductors and the photovoltaic effect to create an electrical current through the absorption of photons. As only a particular range of energies can be absorbed by a semiconductor it is important to look at the solar spectrum. The distribution of solar intensities at different wavelengths are altered by the atmospheric absorption, especially when compared to those emitted by the sun. **Figure 1.1** illustrates a normalized spectral distribution of different points along a photon's route to the earth. The black line illustrates the black body radiation that would be indicative of the energy of a photon at the surface of the sun. The blue line shows the spectrum as a photon enters earth's atmosphere denoted as Air Mass 0 (AM0). The red line indicates the solar spectrum that reaches the earth's surface at an angle of 48.2° and is denoted by AM1.5.

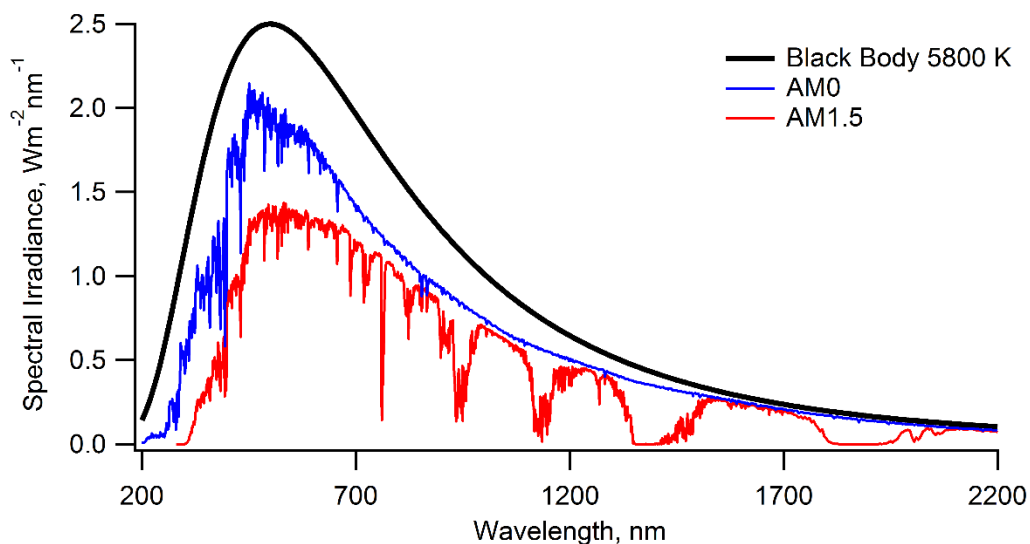


Figure 1.1 The spectral irradiance of a photon at different positions along its path to the earth.

The black line shows the black body irradiation at the sun's surface. The blue line is the spectrum when a photon enters the earth's atmosphere at AM0. The red line is the spectrum of a photon's irradiance as it hits the earth at a solar zenith angle of 48.2° angle, AM1.5. AM1.5 is useful to represent the overall yearly average for regions within the mid-latitudes of the Earth with a culminating average angle of 48.2° .

The problem thus far in most PV research has been the ability of semiconductors to convert this abundant source of energy into usable electricity efficiently.

1.3 Semiconductors

A material is identified as a semiconductor when its electrical conductivity magnitude is between that of a conductor and an insulator. An approximation of its electronic structure is represented by continuous energy bands separated by a gap. The electronic ground state of a semiconductor has electrons filled into the lower energy band known as

the valence band. The higher energy band above the gap is known as the conduction band. The minimum energy required in order to excite an electron from the top of the valence band to the bottom of the conduction band is known as the band gap (E_g).

1.3.1 Types of Semiconductors

The main differences semiconductors rely on the distribution of electrons and the lack of electrons, known as holes, within the energy bands. Electrons and holes can move freely from atom to atom within a semiconductor material. In a band diagram model, the Fermi level energy (E_F) is used to represent the hypothetical energy level of an electron at which the probability of it being occupied is 50%. The type of semiconductor can be illustrated by the location of its E_F (**Figure 1.2**). An intrinsic semiconductor has an equal number of electrons and holes in both bands as a result of thermal excitation and its E_F is located directly in the middle of the band gap. Extrinsic semiconductors can be p-type semiconductors that are an electron deficient material and the majority charge carriers are positive holes. Its E_F is located close to the valence band as a result of the lack of electrons at higher energies. An n-type semiconductor is the opposite of a p-type, with electrons as the majority carriers and an E_F closer to the conduction band as a result of more electrons present at those energy levels.

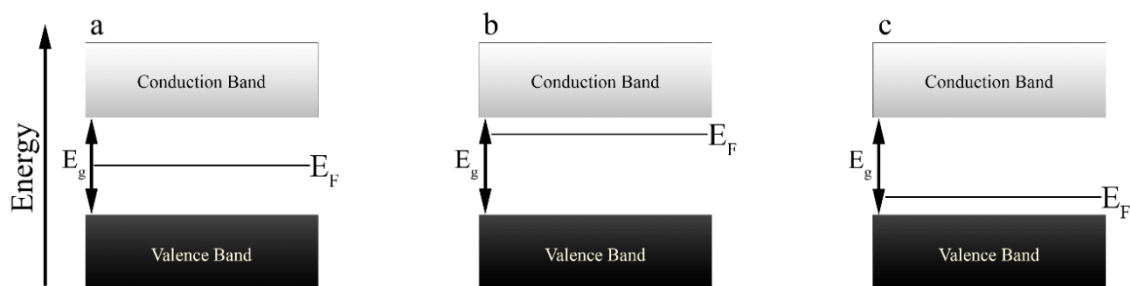


Figure 1.2 Band diagrams for a) an intrinsic semiconductor b) a p-type semiconductor c) an n-type semiconductor p-n Junction

When a p-type and an n-type semiconductor come into contact with each other, a p-n junction is formed. When in contact with each other, the diffusion of the majority charge carriers occurs across the barrier. The movement of the charge exposes the immobilized atom sites; positive ion cores in the n-type semiconductor and negative ion cores in the p-type. As a result, an electric field forms between the positive and negative ion cores resulting in what is known as a space charge region (SCR) (**Figure 1.3**). When light is absorbed by a p-type semiconductor, an electron-hole pair forms. If the pair can separate, the electron moves into the n-type semiconductor and participates in current production.

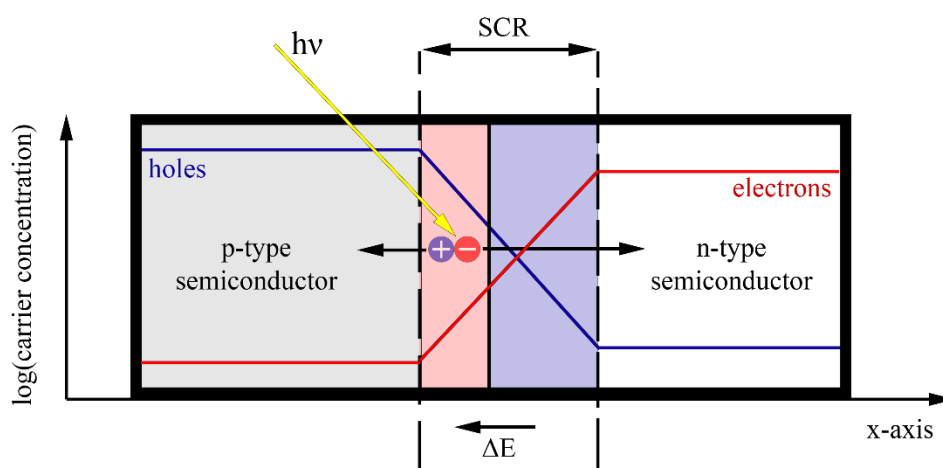


Figure 1.3 Schematic band diagram of a p-n junction

1.4 Photovoltaics Technologies

At present, the abundance of PV research has only been limited to the discovery of new materials. Silicon solar cells were the first practical PVs, invented in 1954 by Bell Labs.⁵ Since then, solar cell development in the area of silicon solar cells have reached upwards of 25 % efficiency.⁵⁻⁶ While these types of solar cells have had much success, an initially high cost of purifying and processing silicon pushed research in search of alternatives.

This has prompted the emergence of several different streams of PV device types:

multijunction cells, thin film technologies, further crystalline Si development, and new emerging PVs. The processing for Si development has mainly focused on reducing the purification process for Si and has been met with success and many variations.⁷⁻⁸

Multijunction solar cells, seek to harvest and combine different semiconductor junctions in order to optimize maximal efficiency.⁹⁻¹⁴ Most recently, the discovery of perovskites for use in solar cells has revamped the emerging PV technologies.¹⁵⁻¹⁷ The reason to focus on thin film photovoltaics lies in the concentration of efforts to make more compact solar cells, while not compromising on lifetime of the devices. For this reason, an in-depth perspective of thin film photovoltaics are necessary in order to develop future solar cell applications.

1.5 Thin Film Photovoltaics

Thin film PVs are one of the fastest growing technologies in the PV market. The major selling point of this type of material is to overcome the indirect band gaps and active material thickness limitation of crystalline silicon – a benchmark in PV materials. These direct band gap materials have high light absorption coefficients and are less material-intensive to capture the same amount of light. These thin film PVs typically have

archetypical layers that operate with specific purposes. This layout can be seen in **Figure 1.4**.

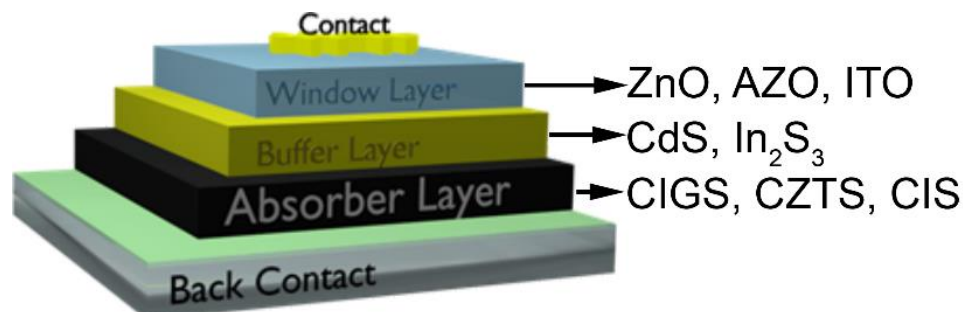


Figure 1.4 Schematic representation of common thin film PV construction

1.5.1 Absorbing Layer

p-type semiconductors are often the singular choice when it comes to absorbing layers in thin film PVs. Thin film solar cells employ an absorbing layer as a method of converting a photon into an electron. At present, copper indium gallium selenide/sulfide ($\text{Cu}(\text{In}_x, \text{Ga}_{1-x})\text{S}/\text{Se}$, CIGS) has record laboratory efficiencies of up to 22.6%.¹⁸⁻¹⁹ Unfortunately, gallium and selenium have been shown to be difficult to handle and to refine and many synthesis rely on energy intensive techniques. Although this material shows high efficiency, it is not an ideal candidate for a sustainable energy future due to this high environmental impact associated with the production of the solar cells.

1.5.2 $\text{Cu}_2\text{ZnSnS}_4$ (CZTS)

Bulk $\text{Cu}_2\text{ZnSnS}_4$ (CZTS) has tuneable a direct band gap of 1.45-1.51 eV matching quite well with the solar spectral range and a large absorption coefficient of 10^4 cm^{-1} .²⁰⁻²¹ As a result, the quaternary kesterite absorbing layer (**Figure 1.5**) is well documented and characterized.²²⁻²⁴ While CZTS thin film solar cells are expected to have a theoretical efficiency of 30% based on photon balance calculations,²⁵ laboratory-size

$\text{Cu}_2\text{ZnSn}(\text{S},\text{Se})_4$ solar cells have reached efficiencies of 12.6 %.²⁶ Low-cost thin film deposition methods for the light-absorbing layers have been developed, such as electrodeposition²⁷ and spray deposition.²⁸ Synthesis of CZTS nanoparticles also means that collar cell could be applied as a simple coating on any number of manufactured goods, but almost all reports required rebuilding crystallinity and stoichiometry via annealing at high temperature and in sulfur or selenium atmosphere.²⁹⁻³¹ Unfortunately, annealing process can often leave unwanted residues that lower the photovoltaic performance.³²

The push for these sulfur-containing, or chalcogenide thin film PVs is to maintain a delicate balance between increasing solar cell efficiency, while reducing and optimizing the cost associated with production.

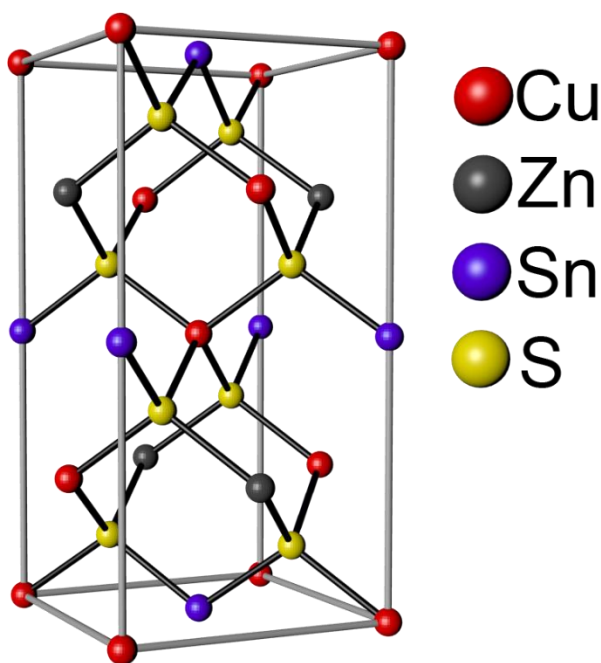


Figure 1.5 Kesterite crystal structure unit cell of CZTS

1.5.3 CuInS₂ (CIS)

The ternary compound, copper indium disulfide (CuInS₂, CIS) seeks to overcome the problems associated with the use of gallium and selenium in a similar fashion as CZTS. Much academic and industrial interest has been paid to CIS thin films due to its particular optoelectronic properties.^{4, 33-34} This is more apparent in the field of PVs in which the ternary semiconductor CIS is often sought for its near optimum band gap (1.54 eV) and high theoretical efficiency (28.5 %).³⁵⁻³⁶ The chalcopyrite crystal structure (**Figure 1.6**) of CIS has been shown to have influence into the effectiveness of CIS as an absorber layer as well.³⁶⁻³⁸ The multitude of methods for obtaining and depositing CIS has also been intensely studied: radio frequency sputtering, thermal evaporation and chemical vapour deposition are just a few of the methods that can be utilized for effective absorbing layers.³⁹⁻⁴³ However, the scalability of many of these techniques is quite limited. Much research has been done to increase the efficiency of these thin film solar cells while decreasing the cost of synthesis and production.⁴⁴ CIS shows great potential to replace CIGS solar cells with laboratory efficiency up to 11.6 %.⁴⁵⁻⁴⁶ Drawbacks of this solution are similar to CIGS in which there are high costs associated with the material production and the environmental impact of the synthesis.⁴² The removal of these steps causes the cost of production and environmental impact to decrease. The synthesis of a low-impact CIS absorbing layer would aid in the current status of inexpensive thin film PV production. The characterizations of the effectiveness of the absorbing layer before production of a full solar cell are crucial to lowering the costs of production and insuring the synthesis is correct.

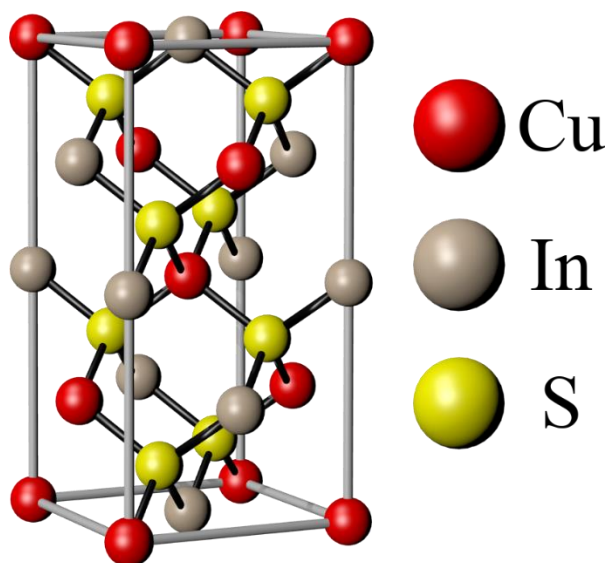


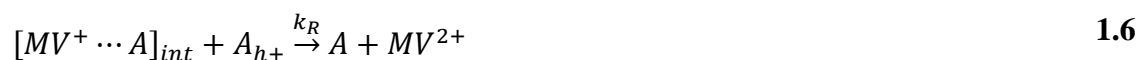
Figure 1.6 Chalcopyrite crystal structure unit cell for CuInS_2

1.5.4 Photoelectrochemistry of Solar Energy Materials

One of the cruxes of the developments in solar cell research is the specificity at which each layer operates and interacts with the ones around it. With this in mind, when dealing with novel approaches to solar energy materials, there is no single methodology that can be applied to every material. A systematic approach has to be undertaken in order to identify key features and optimize each layer.

Photoelectrochemical measurements (PECMs) utilize a solution-phase oxidant to mimic the effects of contact with a semiconductor.⁴³ Utilizing the absorbing layer as a working electrode and an electrochemical cell with reference and counter electrodes, the reduction of the solution produces a measurable current under applied bias when the working electrode is illuminated. The standard reduction potential of a solution-phase oxidant, such as methyl viologen (MV^{2+}) must lie in between the conduction band and valence bands of the absorber layer in order to facilitate the movement of photogenerated electrons.⁴⁷⁻⁴⁸ When light illuminates an absorber layer (A), the photon conversion to

electrons generate a series of photoreactions as it interacts with the MV^{2+} (**Equations 1.2-1.6**).



When an absorber layer is introduced to photons, a photogenerated electron-hole pair is generated (**Equation 1.2**).⁴⁹⁻⁵¹ The photogenerated electron-hole pair can immediately decay into its original state, producing no current (**Equation 1.3**). The p-type absorbing layer then observes a measureable minority carrier flux towards the solution interface, described as the Gärtner flux (g_1).⁵²⁻⁵³ If the electron is able to flow to the interface, it can transfer to MV^{2+} where an intermediate can occur (**Equation 1.4**). This is usually indicated through a sharp increase in current when measured at an applied potential.⁵⁴⁻⁵⁵ The intermediate species could recombine with a hole present in the absorber to its ground state and form the original reagents (**Equation 1.5**). This is represented by a decay in the photocurrent generated by the electrochemical system. A competing process is the successful reduction of the MV^{2+} species (**Equation 1.6**).

Intensity modulated photocurrent spectroscopy seeks to quantify the rates of these photoreactions. The application of a sinusoidal modulation on the light intensity over a range of frequencies can be seen in the complex function of the AC component of the

measured photocurrent.^{49, 56} Given a simple equivalent circuit, such as a resistor and capacitor in series, the expression of the AC component of the photocurrent (j_1) can be simplified into **Equation 1.7**

$$j_1 = g_1 \frac{k_{PS} + i\omega}{k_R + k_{PS} + i\omega} \left(\frac{1}{1 + RCi\omega} \right) \quad \mathbf{1.7}$$

where g_1 is the Gärtner flux, k_{PS} is the rate of product separation, k_R is the rate of recombination, ω is the frequency, R is the resistance, and C is the interfacial capacitance.

The modelled, response with respect to the real and imaginary components of the photocurrent are seen in **Figure 1.7** in which different relative rates of recombination and product separation occur, giving rise to observable patterns.^{49, 51}

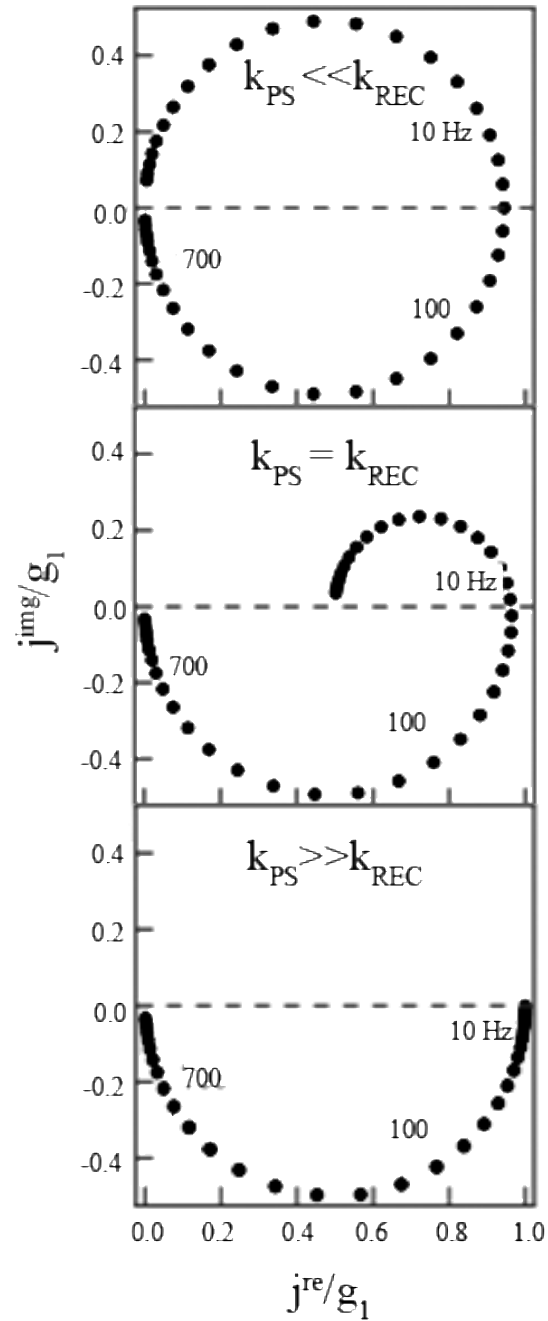


Figure 1.7 IMPS transients for characteristic rates of product separation and recombination

Employing these methods as tools allow for a probing of the film and its interface before the production of a full solar cell device. This effort has the benefit of economic use of

time and resources, to ensure effective absorbing layers for eventual use within photovoltaic devices.

1.5.5 Synchrotron-Based Spectroscopies

Synchrotron radiation is the nomenclature given to the resultant radiation emitted when electrons are accelerated at a speed close to light and circulated in a curved path. A synchrotron facility can produce high energy photons using a combination of linear accelerator and booster ring. An accelerator confines electrons using electromagnetic fields into a near-circular orbits.⁵⁷ When these electrons are accelerated at speed close to light, the circular movement allows for a centripetal force to act on these particles, causing a generation of electromagnetic radiation. This radiation is typically within the X-ray to vacuum ultraviolet regions of energies.⁵⁷⁻⁵⁸ A synchrotron beamline is a specialized type of synchrotron instrument in which photons can be turned into a highly tuneable source of radiation by the specialized sets (bending magnets or insertion devices) in the storage ring of a synchrotron facility.⁵⁹ With this instrumentation, precise control over the energy level and polarization of photons can be culminated and sent to collide with an object of interest.

An X-ray is electromagnetic radiation that have relatively short wavelengths ($\sim 10^{-3}$ -10 nm) that lay between ultraviolet and gamma ray radiation. The designation of “hard” and “soft” X-rays are based on these ranges respectively. When X-rays collide with a sample, they interact with the electrons bound in the sample’s atoms and are either scattered or absorbed. The absorption of X-rays by a sample causes an ejection of core-level electron.⁵⁷⁻⁵⁹ These absorption energies are specific for individual atoms (E_o) and are designated edges for specific electrons within the atoms (**Figure 1.8**).

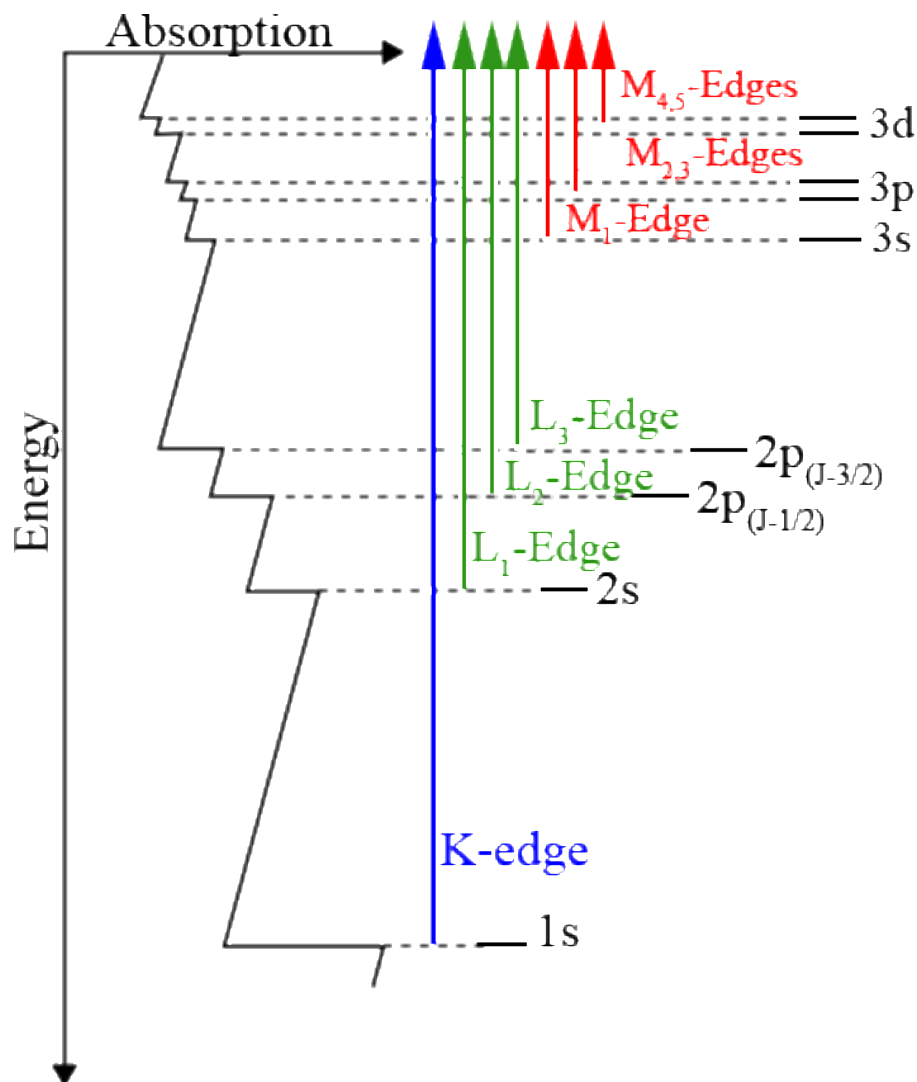


Figure 1.8 Illustrative X-ray absorption spectrum of a transition metal atom

With a sweep of X-ray energy approaching and passing the E_0 of an atom, there are two characteristic regions of the absorption that define different local and extended environments of the atom itself (**Figure 1.9**). An absorption edge is the energy at which there is a sharp rise (discontinuity) in the (linear) absorption coefficient of X-rays by an element, which occurs when the energy of the photon corresponds to the energy of a shell of the atom (K, L₁, L₂, L₃, etc. corresponding to the creation of electron holes in the 1s, 2s, 2p_{1/2}, 2p_{3/2} etc. atomic subshells).⁵⁹

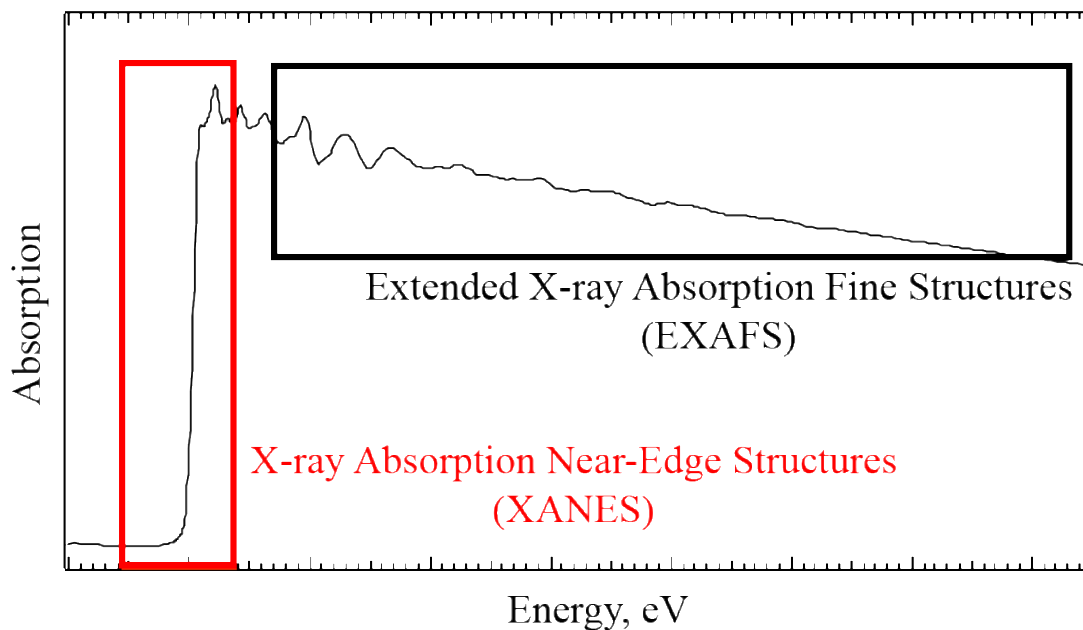


Figure 1.9 Exemplar metal X-ray absorption edge showing defined regions of analysis

X-ray absorption near-edge structures (XANES, black) is roughly defined as the region ~ 10 eV below the E_0 to ~ 30 eV above E_0 . When approaching the absorption edge and the photon energy is low enough, the ejected core electrons (photoelectrons) caused by electronic transitions can populate either unoccupied bound states or low-lying continuum states, this is known as the pre-edge.⁶⁰⁻⁶¹ These pre-edge characteristics are altered by changes in the local geometry around the absorbing atom and illustrate a dependence on oxidation state and bonding characteristics.⁶² Similarly the E_0 intensity and energy shift is a function of the absorbing atom's oxidation state. The XANES region contains information on the atomic position of neighbours, and alters based on interatomic distances and bond angles.⁶³⁻⁶⁴ This allows for a qualitative “fingerprint” on the coordination chemistry, molecular orbitals, band structure, and multiple scattering geometry of atoms of interest, allowing for atomic precision on desired structures.

Extended X-ray absorption fine structures (EXAFS) analysis involves the investigation of long range oscillations in the post-edge region (~ 30 eV to $1000 \sim$ eV above E_0).⁵⁷ At these energies the effect of elastic scattering of the photoelectron by neighbouring atoms is apparent.⁶⁵ These oscillations correspond to the constructive and destructive interference between the photoelectron wave and the backscattered wave.⁶⁶ Deconvolution of these waves through EXAFS analysis can contribute qualitative information on specific neighbouring atoms and can again allow for atom-specific probes for a sample.

1.6 Scope of Thesis

The focus of this research has been to customize and optimize CZTS and CIS chalcogenide thin film PVs layer-by-layer. This was accomplished by beginning with the synthesis of the absorbing layers, followed by the optimization of each subsequent layer in the solar cell as well as modifying the interfaces between them. The physical, chemical, and optical properties of CIS and CZTS were explored and identified utilizing a wide range of techniques and methods. This work has allowed for insight into the properties of the chalcogenide thin films in order to facilitate an effective absorbing layer and incorporate it into a PV device while maintaining low costs.

Chapter 2 deals with the synthesis of CZTS nanocrystals (NCs) via a facile and low-cost one-pot method. Using photoelectrochemical measurements (PECMs) as a basis for effective light absorbing layers, photovoltaic behaviour of NC films was assessed. The optimization of the CZTS through PECMs is a simple and powerful strategy. Non-stoichiometric copper rich and zinc poor starting molar ratios provided the best overall products although they are not concerted throughout the reaction. Other analytical and physical techniques were further used to identify NC composition, topography and

crystallinity and oxidation states of the elements. Analogous experiments were performed to characterize CIS thin films in a similar fashion.³⁴ This work generated the basis for much of the following research and functioned as a base on which the following work was carried out.

Through the continuation of electrochemical probing, the interface of CIS nanocrystal films (NCF) were explored in Chapter 3. Intensity modulated photocurrent spectroscopy (IMPS) was performed at the nanocrystal film/solution interface. IMPS quantified the kinetic constants of the photoreaction. The rate ratio of the product separation to recombination increased as a function of applied potential, while the RC time constant decreased. Interfacial reaction kinetics of a solution-phase oxidant and the CIS film was revealed by means of PECMs and IMPS. The interaction of the light absorbing CIS NCFs at a hole-rich interface allow for an understanding of what might happen at an analogous n-type junction. CZTS/solution interfaces were also probed utilizing the IMPS technique, giving insight into how CIS and CZTS would be able to act at an interface as well as which conditions were conducive to photocurrent generation.⁶⁷⁻⁶⁸

Chapter 4 delved into CZTS NCs based on their initial metal stoichiometry and photoresponse behavior. CZTS films were divided into groups of high-photoresponse (hp-CZTS) and low-photoresponse samples (lp-CZTS). An X-ray absorption near-edge structure (XANES) study was then performed to unravel the origin of the difference in their photovoltaic properties. The results demonstrated that, the local structures of the elements and their interaction with capping ligands are different and strongly affect the photovoltaic behavior, although both CZTS groups through one-pot synthesis were free of secondary phases. It was determined that the coordination of Zn and the capping

ligand-metal interaction are the two major factors for the production of higher photocurrent. The correlations were used as a guide to produce viable CZTS films crucial for the development of solar energy conversion.

The CZTS/CdS heterojunction was examined using photoelectrochemical and synchrotron radiation (SR) spectroscopies in Chapter 5. The study provided physical insights into the interface that was formed by electrophoretic deposition (EPD) of CZTS NCs and chemical bath deposition (CBD) of CdS for the two respective films. Results showed that CBD induced a change in the local and long range environment of the Zn in the CZTS lattice that was detrimental to the photoresponse. XANES and extended X-ray absorption fine structures (EXAFS) of the junction showed that this change was at an atomic level and was associated with the coordination of oxygen to zinc, which was confirmed through FEFF fitting. It was discovered that this change can be reversed with the use of low temperature annealing in both photoresponse and in the Zn. Investigating CZTS through synchrotron radiation (SR) techniques provides detailed structural information of minor changes from the zinc perspective.

Both Chapter 6 and Chapter 7 dealt with the conclusion of the construction of solar cell devices. The construction of the full device and the measurement of efficiency for CZTS solar cell constructed via a NC route and through galvanostatic electroplating of metal precursors. The EPD of CZTS NCs and formation of the solar cell followed closely with the information obtained from previous chapters on optimized solar cell layers. For the electroplated samples, galvanostatic electrodeposition precursors from environmentally friendly electrolytes and sulfurization were implemented. Optimized sequential electrodepositions of Cu, Sn, and Zn films were carried out on molybdenum-coated glass,

while the sulfurization of Mo/Cu/Sn/Zn precursors was performed. An analogous series of tests were performed to confirm if the findings from previous chapters could be applied to these new CZTS films. The produced CZTS films were characterized in detail by PECMs, scanning electron microscopy (SEM) with energy dispersive X-ray spectroscopy (EDX), Raman spectroscopy, X-ray diffraction (XRD), and UV-Vis spectroscopy. In both cases the results of XRD and Raman depicted that all CZTS films possessed kesterite structure. A direct band gap of about 1.47 and 1.45 eV for the produced for the EPD and electroplated CZTS films respectively. All the measurements demonstrated that the CZTS films fabricated by EPD and galvanostatic electroplating meet the requirements for a light-absorbing layer and is a potential candidate in CZTS solar cells. The J-V measurement demonstrates that the conversion efficiencies of the CZTS solar cells are 1.28 and 2.21 % for EPD and electroplating respectively.

These chapters have formed a plethora of knowledge in areas of NC CIS and CZTS solar cells and serve as a stepping stone for those to continue to optimize and change the interfaces and reactions of the solar cell device. The CZTS route has not yet reached its full potential, but with increasing amounts of work and investigative studies into its properties, a penultimate solar cell is close at hand. Focusing on a cost-effective and environmentally-friendly approach not only enriches the sole drive for solar energy, but is forward thinking that will allow for a sustainable future in energy production.

1.7 References

- (1) Greene, D. L.; Hopson, J. L.; Li, J.; *Energ. Policy*, (2006), 34, 515-531.
- (2) Perez, R.; Zweibel, K.; Hoff, T. E.; *Energ. Policy*, (2011), 39, 7290-7297.
- (3) Inganas, O.; Sundstrom, V.; *Ambio*, (2016), 45, S15-23.

- (4) Batabyal, S. K.; Tian, L.; Venkatram, N.; Ji, W.; Vittal, J. J.; *J. Phys. Chem. C*, (2009), 113, 15037-15042.
- (5) Green, M. A.; *Prog. Photovoltaics*, (2009), 17, 183-189.
- (6) Masuko, K.; Shigematsu, M.; Hashiguchi, T.; Fujishima, D.; Kai, M.; Yoshimura, N.; Yamaguchi, T.; Ichihashi, Y.; Mishima, T.; Matsubara, N.; TYamanishi, T.; Takahama, T.; Taguchi, M.; Maruyama, E.; Okamoto, S.; *IEEE J. Photovolt.*, (2014), 4, 1433-1435.
- (7) Branham, M. S.; Hsu, W. C.; Yerci, S.; Loomis, J.; Boriskina, S. V.; Hoard, B. R.; Han, S. E.; Chen, G.; *Adv. Mater.*, (2015), 27, 2182-2188.
- (8) Tucher, N.; Eisenlohr, J.; Hauser, H.; Benick, J.; Graf, M.; Müller, C.; Hermle, M.; Goldschmidt, J. C.; Bläsi, B.; *Energy Procedia*, (2015), 77, 253-262.
- (9) Cotal, H.; Fetzer, C.; Boisvert, J.; Kinsey, G.; King, R.; Hebert, P.; Yoon, H.; Karam, N.; *Energy Environ. Sci.*, (2009), 2, 174-192.
- (10) Kinsey, G. S.; Hebert, P.; Barbour, K. E.; Krut, D. D.; Cotal, H. L.; Sherif, R. A.; *Prog. Photovoltaics*, (2008), 16, 503-508.
- (11) King, R. R.; Bhusari, D.; Larrabee, D.; Liu, X. Q.; Rehder, E.; Edmondson, K.; Cotal, H.; Jones, R. K.; Ermer, J. H.; Fetzer, C. M.; Law, D. C.; Karam, N. H.; *Prog. Photovoltaics*, (2012), 20, 801-815.
- (12) Faine, P.; Kurtz, S. R.; Riordan, C.; Olson, J. M.; *Solar Cells*, (1991), 31, 259-278.
- (13) Mann, S. A.; Garnett, E. C.; *ACS Photonics*, (2015), 2, 816-821.
- (14) King, R. R.; Law, D. C.; Edmondson, K. M.; Fetzer, C. M.; Kinsey, G. S.; Yoon, H.; Sherif, R. A.; Karam, N. H.; *Appl. Phys. Lett.*, (2007), 90, 183516 1-3.
- (15) Bailie, C. D.; Christoforo, M. G.; Mailoa, J. P.; Bowring, A. R.; Unger, E. L.; Nguyen, W. H.; Burschka, J.; Pellet, N.; Lee, J. Z.; Grätzel, M.; Noufi, R.; Buonassisi, T.; Sallee, A.; McGehee, M. D.; *Energy Environ. Sci.*, (2015), 8, 956-963.

- (16) Smith, I. C.; Hoke, E. T.; Solis-Ibarra, D.; McGehee, M. D.; Karunadasa, H. I.; *Angew. Chem.*, (2014), 53, 11232-11235.
- (17) Stranks, S. D.; Nayak, P. K.; Zhang, W.; Stergiopoulos, T.; Snaith, H. J.; *Angew. Chem.*, (2015), 54, 3240-3248.
- (18) Xu, J.; Luan, C.-Y.; Tang, Y.-B.; Chen, X.; Zapfen, J. A.; Zhang, W.-J.; Kwong, H.-L.; Meng, X.-M.; Lee, S.-T.; Lee, C.-S.; *ACS Nano*, (2010), 4, 6064-6070.
- (19) Jackson, P.; Wuerz, R.; Hariskos, D.; Lotter, E.; Witte, W.; Powalla, M.; *Phys. Status Solidi RRL*, (2016), DOI: 10.1002/pssr.201600199.
- (20) Mitzi, D. B.; Gunawan, O.; Todorov, T. K.; Wang, K.; Guha, S.; *Sol. Energ. Mat. Sol. Cells*, (2011), 95, 1421-1436.
- (21) Katagiri, H.; Jimbo, K.; Maw, W. S.; Oishi, K.; Yamazaki, M.; Araki, H.; Takeuchi, A.; *Thin Solid Films*, (2009), 517, 2455-2460.
- (22) Walsh, A.; Chen, S.; Wei, S.; Gong, X. G.; *Adv. Energy Mater.*, (2012), 2, 400-409.
- (23) Just, J.; Lützenkirchen-Hecht, D.; Frahm, R.; Schorr, S.; Unold, T.; *Appl. Phys. Lett.*, (2011), 99, 262105 1-3.
- (24) Chen, S.; Gong, X. G.; Walsh, A.; Wei, S.; *Appl. Phys. Lett.*, (2010), 96, 021902 1-4.
- (25) Amano, F.; Tian, M.; Wu, G.; Ohtani, B.; Chen, A.; *ACS Appl. Mater. Interfaces*, (2011), 3, 4047-4052.
- (26) Wang, W.; Winkler, M. T.; Gunawan, O.; Gokmen, T.; Todorov, T. K.; Zhu, Y.; Mitzi, D. B.; *Adv. Energy Mater.*, (2014), 4, 1301465 1-5.
- (27) Scragg, J. J.; Dale, P. J.; Peter, L. M.; *Electrochem. Commun.*, (2008), 10, 639-642.
- (28) Madarasz, J.; Bombicz, P.; Okuya, M.; Kaneko, S.; *Solid State Ionics*, (2001), 141-142, 439-446.

- (29) Steinhagen, C.; Panthani, M. G.; Akhavan, V.; Goodfellow, B.; Koo, B.; Korgel, B. A.; *J. Am. Chem. Soc.*, (2009), *131*, 12554-12555.
- (30) Guo, Q.; Hillhouse, H. W.; Agrawal, R.; *J. Am. Chem. Soc.*, (2009), *131*, 11672-11673.
- (31) Guo, Q.; Ford, G. M.; Hillhouse, H. W.; Agrawal, R.; *Nano Lett.*, (2009), *9*, 3060-3065.
- (32) Panthani, M. G.; Akhavan, V.; Goodfellow, B.; Schmidtke, J. P.; Dunn, L.; Dodabalapur, A.; Barbara, P. F.; Korgel, B. A.; *J. Am. Chem. Soc.*, (2008), *130*, 16770-16777.
- (33) Pons, T.; Pic, E.; Lequeux, N.; Cassette, E.; Bezdetnaya, L.; Guillemain, F.; Marchal, F.; Dubertret, B.; *ACS Nano*, (2010), *4*, 2531-2538.
- (34) Tapley, A.; Vaccarello, D.; Hedges, J.; Jia, F.; Love, D. A.; Ding, Z.; *Phys. Chem. Chem. Phys.*, (2013), *15*, 1431-1436.
- (35) Siebentritt, S.; *Thin Solid Films*, (2002), *403-404*, 1-8.
- (36) Shay, J. L.; Wernick, J. H. *Ternary Chalcopyrite Semiconductors: Growth, Electronic Properties and Applications*; Pergamon Press: New York, 1975.
- (37) Lauermann, I.; Kropp, T.; Vottier, D.; Ennaoui, A.; Eberhardt, W.; Aziz, E. F.; *Chemphyschem*, (2009), *10*, 532-5.
- (38) Schorr, S.; Mainz, R.; Mönig, H.; Lauermann, I.; Bär, M.; *Prog. Photovoltaics Res. Appl.*, (2012), *20*, 557-567.
- (39) Genevee, P.; Donsanti, F.; Renou, G.; Lincot, D.; *J. Phys. Chem. C*, (2011), *115*, 17197-17205.
- (40) Peter, L. M.; *J. Phys. Chem. Lett.*, (2011), *2*, 1861-1867.

- (41) Wang, Y.-H. A.; Zhang, X.; Bao, N.; Lin, B.; Gupta, A.; *J. Am. Chem. Soc.*, **(2011)**, *133*, 11072-11075.
- (42) Kemell, M.; Ritala, M.; Leskelä, M.; *CRC Cr. Rev. Sol. State*, **(2005)**, *30*, 1-31.
- (43) Ye, H.; Akhavan, V. A.; Goodfellow, B. W.; Panthani, M. G.; Korgel, B. A.; Bard, A. J.; *J. Phys. Chem. C*, **(2011)**, *115*, 234-240.
- (44) Shi, X.; Xi, L.; Fan, J.; Zhang, W.; Chen, L.; *Chem. Mater.*, **(2010)**, *22*, 6029-6031.
- (45) Cherian, A. S.; Jinesh, K. B.; Kashiwaba, Y.; Abe, T.; Balamurugan, A. K.; Dash, S.; Tyagi, A. K.; Kartha, C. S.; Vijayakumar, K. P.; *Sol. Energy*, **(2012)**, *86*, 1872-1879.
- (46) Braunger, D.; Hariskos, D.; Walter, T.; Schock, H. W.; *Sol. Energ. Mat. Sol. Cells*, **(1996)**, *40*, 97-102.
- (47) Bennett, T.; Niroomand, H.; Pamu, R.; Ivanov, I.; Mukherjee, D.; Khomami, B.; *Phys. Chem. Chem. Phys.*, **(2016)**, *18*, 8512-21.
- (48) Jiang, T.; Xie, T.; Yang, W.; Chen, L.; Fan, H.; Wang, D.; *J. Phys. Chem. C*, **(2013)**, *117*, 4619-4624.
- (49) Peter, L. M.; *Chem. Rev.*, **(1990)**, *90*, 753-769.
- (50) Schaming, D.; Hojeij, M.; Younan, N.; Nagatani, H.; Lee, H. J.; Girault, H. H.; *Phys. Chem. Chem. Phys.*, **(2011)**, *13*, 17704-17711.
- (51) Fermin, D. J.; Duong, H. D.; Ding, Z. F.; Brevet, P. F.; Girault, H. H.; *Phys. Chem. Chem. Phys.*, **(1999)**, *1*, 1461-1467.
- (52) Li, J.; Peter, L. M.; *J. Electroanal. Chem.*, **(1985)**, *193*, 27-47.
- (53) Ahmed, A. Y.; Oekermann, T.; Lindner, P.; Bahnemann, D.; *Phys. Chem. Chem. Phys.*, **(2012)**, *14*, 2774-2783.
- (54) Gärtner, W.; *Phys. Rev.*, **(1959)**, *116*, 84-87.

- (55) Peat, R.; Peter, L. M.; *J. Electroanal. Chem.*, **(1987)**, 228, 351-364.
- (56) DiCarmine, P. M.; Semenikhin, O. A.; *Electrochim. Acta*, **(2008)**, 53, 3744-3754.
- (57) Teo, B. K. *EXAFS: Basic Principles and Data Analysis*; Springer: Berlin, 1986.
- (58) Willmott, P. *An Introduction to Synchrotron Radiation: Techniques and Applications*; John Wiley & Sons: West Sussex, 2011.
- (59) Newville, M.; *Rev. Mineral. Geochem.*, **(2014)**, 78, 33-74.
- (60) Li, R.; Krcha, M. D.; Janik, M. J.; Roy, A. D.; Dooley, K. M.; *Energy Fuels*, **(2012)**, 26, 6765-6776.
- (61) Rajendran, J.; Gialanella, S.; Aswath, P. B.; *Mat. Sci. Eng. C*, **(2013)**, 33, 3968-3979.
- (62) Lamberti, C.; Bordiga, S.; Bonino, F.; Prestipino, C.; Berlier, G.; Capello, L.; D'Acapito, F.; Xamena, F. X. L. i.; Zecchina, A.; *Phys. Chem. Chem. Phys.*, **(2003)**, 5, 4502-4509.
- (63) Chiou, J. W.; Kumar, K. P. K.; Jan, J. C.; Tsai, H. M.; Bao, C. W.; Pong, W. F.; Chien, F. Z.; Tsai, M.-H.; Hong, I.-H.; Klauser, R.; Lee, J. F.; Wu, J. J.; Liu, S. C.; *Appl. Phys. Lett.*, **(2004)**, 85, 3220-3222.
- (64) Fleet, M. E.; *Can. Mineral.*, **(2005)**, 43, 1811-1838.
- (65) Hartman, K.; Newman, B. K.; Johnson, J. L.; Du, H.; Fernandes, P. A.; Chawla, V.; Bolin, T.; Clemens, B. M.; Cunha, A. F.; Teeter, G.; Scarpulla, M. A.; Buonassisi, T.; *IEEE Phot. Spec. Conf.*, **(2011)**.
- (66) Ravel, B.; Newville, M.; *J. Synchrotron Radiat.*, **(2005)**, 12, 537-41.
- (67) Perini, L.; Vaccarello, D.; Martin, S.; Jeffs, K.; Ding, Z.; *J. Electrochem. Soc.*, **(2015)**, 163, H3110-H3115.

(68) Khoshmashrab, S.; Turnbull, M. J.; Vaccarello, D.; Nie, Y.; Martin, S.; Love, D. A.; Lau, P. K.; Sun, X.; Ding, Z.; *Electrochim. Acta*, (2015), 162, 176-184.

2 Optimization of $\text{Cu}_2\text{ZnSnS}_4$ Nanocrystal Recipe by means of Photoelectrochemical Measurements

Synthesis of $\text{Cu}_2\text{ZnSnS}_4$ (CZTS) nanocrystals (NCs) via a one-pot method was facile and low-cost to realize. Using photoelectrochemical measurements (PECMs) as a basis for effective light absorbing layers, photovoltaic behaviour of NC films was assessed. The optimization of the CZTS through PECMs is a simple and powerful strategy. Non-stoichiometric copper rich and zinc poor starting molar ratios provided the best overall products although they are not concerted throughout the reaction. Other analytical techniques were further used to identify NC composition, topography and crystallinity. The oxidation states of the elements in CZTS were found to be 1+, 2+, 4+ and 2- for copper, zinc, tin, and sulfur respectively.

2.1 Introduction

Bulk $\text{Cu}_2\text{ZnSnS}_4$ (CZTS) has a direct band gap of 1.45-1.51 eV matching well with the solar spectrum. CZTS consists of 4 earth-abundant elements, which will reduce fabrication cost easily relative to its counterpart, CuInGaSe_2 even prepared with cost-effective electrodeposition.¹ While CZTS thin film solar cells are expected to have theoretical efficiency of 30% based on photon balance calculations,² laboratory size $\text{Cu}_2\text{ZnSn}(\text{S},\text{Se})_4$ ones have reached an efficiency of 9.7%-10.1%.³⁻⁴ Low-cost thin film deposition methods for the light-absorbing layers have been developed, such as electrodeposition, and spray deposition.⁵⁻⁶ Synthesis of CZTS nanoparticles has the advantage for fabrication and coatings, but almost all reports required rebuilding crystallinity and stoichiometry via annealing at high temperature and in S or Se atmosphere.⁷⁻¹³ The capping ligands were "burned out" in the annealing process leaving

unwanted residues that lower the photovoltaic performance as in the case of CuInS₂, CuInSe₂ and CuInGaSe₂.¹⁴ CZTS nanowires/nanotubes and sphalerite-type (Cu₂Sn)_{x/3}Zn_{1-x}S (0 ≤ x ≤ 0.75) NCs were also fabricated via sol-gel method.¹⁵⁻¹⁶

Herein, a one-pot synthetic method is reported for CZTS nanocrystals (NCs) at low temperatures and without annealing. Photoelectrochemical measurements (PECMs) of the reduction of methyl viologen dichloride (MV²⁺) in aqueous solution were used as a basis for the photoeffectiveness of the NC films.¹⁷ Morphology, crystallinity, oxidation states and stoichiometry of the CZTS NCs were investigated using various analytical methods.

2.2 Experimental

2.2.1 Nanocrystal Preparation

The NC preparation began with mixing copper, zinc and tin salts. Acetylacetonates (acac), chlorides and sulfates were used as counter ions for the metal salts and various combinations of these reagents and with different molar ratios were tested. The precursors were heated at 160 °C in benzyl alcohol (BA) for two minutes to allow for the salts to be fully dissolved. Thiourea was added as the sulfur source and 2-mercapto-5-n-propylpyrimidine (MPP) was added as the capping ligand. The solution was stirred at 180 °C for ten minutes and then cooled to room temperature. The reacted solution was centrifuged and the supernatant was discarded. The precipitate was dispersed in acetone and centrifuged to clean any remaining BA and/or MPP. The resulted NCs were dispersed in acetone at 20 g/L and drop-casted onto a well-defined surface area on an indium-doped tin oxide coated polyethylene terephthalate substrate (ITO-PET).

2.2.2 Photoelectrochemical Set-up

The PEC set-up consisted of a 150 W Newport lamp with an AM 1.5D filter, and a CH Instruments potentiostat. The NC film on the ITO-PET plate was the working electrode submerged in a 0.1 M MV^{2+} electrolyte solution. A platinum and standard calomel electrode (SCE) were used as counter and reference electrodes. Current was measured versus applied potential sweeping from 0 to -0.400 V while chopped light was directed onto a 10.0 mm² area of NC film at a frequency of 0.167 Hz.

2.2.3 Characterization

Scanning electron microscopy (SEM) was performed on a Hitachi S-4500 field emission microscope with an energy dispersive X-ray spectroscopy (EDX) system. Transmission electron microscopy (TEM) was done on a Philips CM 10. Powder X-ray diffraction (XRD) was examined on an Inel CPS Powder Diffractometer with Cu X-ray radiation source. X-ray photoelectron spectroscopy (XPS) was investigated on a Kratos AXIS Nova Spectrometer with an Al K α X-ray source.

2.3 Results and Discussion

2.3.1 PECMs and Sample Selection

This is the first occurrence of CZTS NCs via a one-pot synthesis without post-processing. Over 200 combinations were tried based on the different starting materials and permutations of concentrations. Concentrations ranging from 1-5 molar equivalents were tested at intervals of 0.5 for each material. An area that provided higher photoresponse was tested at ratios in between the intervals for all metal salt combinations to aid in the identification of a molar ratio that was best suited for the synthesis. It was found that

different counterions have varied effects on the photoelectroconversion of the materials. $\text{Cu}(\text{acac})_2$, ZnCl_2 and SnCl_2 were the best sources that generated NCs with the largest photocurrent density. The NC film showed poor photoconversion if SnSO_4 was used. MPP functions as effective capping ligand for CZTS NCs similar to the case of Cu clusters,¹⁸ without compromising their photovoltaic role, which might be better than other ligands such as oleylamine.^{7-8, 11} With these factors in mind, two samples were chosen based on their photo-response. D70 was chosen because of it had the largest photo-response and utilized the metal salts that worked best with the synthesis: $\text{Cu}(\text{acac})_2$, ZnCl_2 and SnCl_2 . A50 was among the lowest photo-response samples and used the metal salts: CuCl_2 , ZnCl_2 and SnCl_2 . Both samples yielded results that were characteristic of working and non-working groups of CZTS NCs.

Figure 2.1 shows linear sweep voltammograms (LSVs) of two CZTS NC thin films drop-casted from two contrasted samples among the 200, D70 and A50, on ITO-PET upon alternative light-on, -off switching. The NC films were used as photoelectrodes in a three-electrode photoelectrochemical cell. The MV^{2+} , which served as a redox mediator, did produce some background current which can be seen by the non-zero values of the dark current. The films had an alternating pattern of photocurrent evolution and devolution following light on-off switching during the potential sweep from 0 to -0.400 V at a scan rate of 5 mV/s. Electrons promoted to the conduction band of the CZTS film upon light illumination were transferred to MV^{2+} that was reduced to MV^{1+} . This electron transfer caused a cathodic current between the ITO-PET and Pt counter electrodes, which was used as a criterion for the photovoltaic effectiveness of the NC films. It can be seen that D70 had a much larger difference in photocurrent density (up to 0.15 mA/cm^2) in

dark and light illumination than A50 did. This PECM was used as the key criterion to test the photovoltaic effectiveness of NC films throughout the recipe optimization. In **Figure 2.1**, the dark current is shown as the dashed curves. The introduction of the light can be seen in the sharp increase in current density. All photocurrent transients display desirable steady state, showing low charge recombination, which are very competitive among light absorbing thin films prepared.^{10, 17}

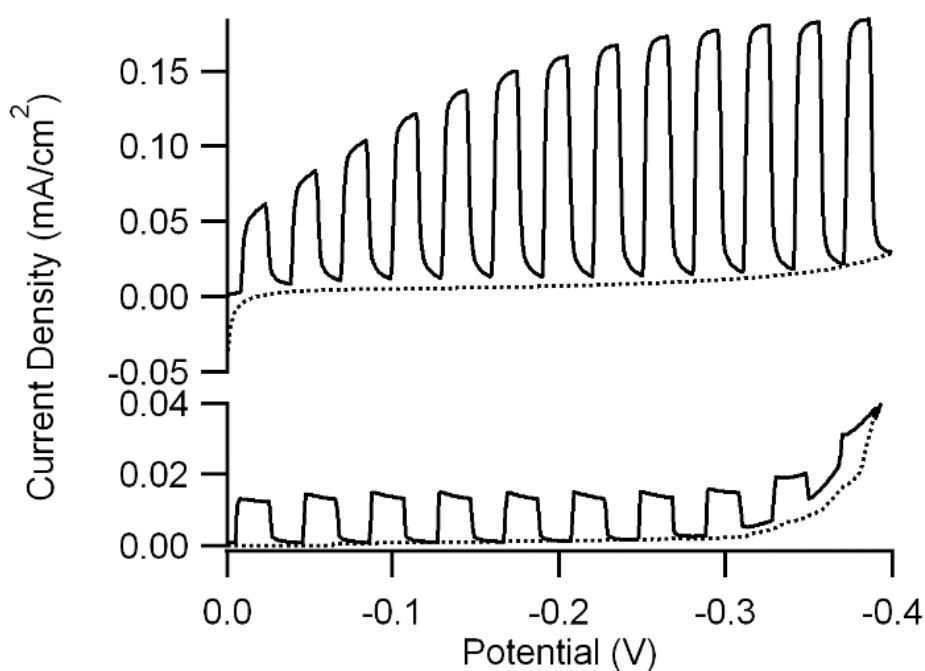


Figure 2.1 Current density-potential curves of D70 and A50 during PECMs (top and bottom). The dashed curves are the LSVs in the dark for the two samples.

2.3.2 SEM and TEM

Figure 2.2a) demonstrates an SEM image of D70 which had an average crystal size of $51.6 \text{ nm} \pm 4.7 \text{ nm}$, whereas A50 had an average size of $663.6 \text{ nm} \pm 84.1 \text{ nm}$ (**Figure 2.2b**). Sample D70 had little surface detail or irregularities i.e. smooth and uniform surfaces. In contrast, the non-working material A50 has a granular appearance and many

irregularities. The smooth surface may have allowed for a greater flow of electrons through the sample due to many points of contact rather than the granular edge contacts. The insets of **Figure 2.2a** and **b** show TEM of D70 and A50. The NC sizes of D70 averaged $43.6 \text{ nm} \pm 1.2 \text{ nm}$ in diameter, a little smaller than that determined from SEM. An individual NC size of A50 estimated from TEM ranges from approximate 100 nm to 270 nm. Both TEM images reveal that the two samples do not appear to be single NCs, rather a cluster. This is especially apparent in D70. It is most difficult to see these substructures in sample A50 as it is nearly opaque. Its structures are also not uniformly shaped. The larger A50 sample seems to take a relatively uniform circular structure whereas D70 may be made of irregular clusters.

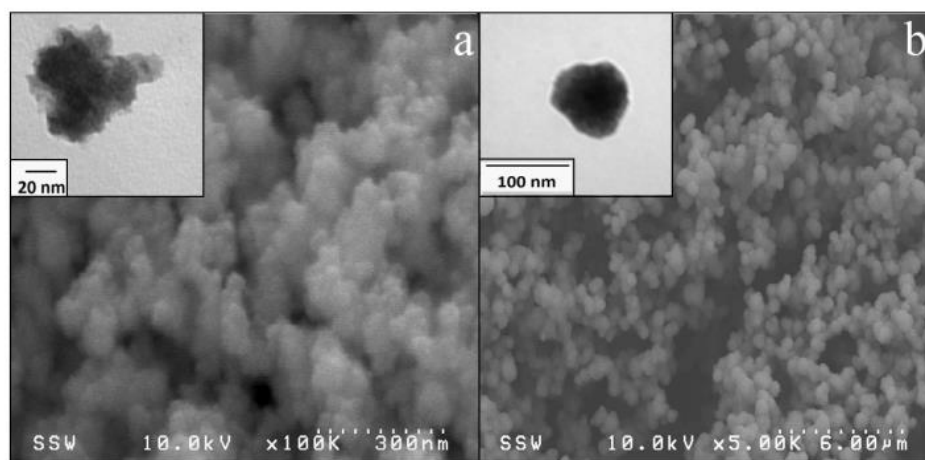


Figure 2.2 SEM with TEM inset of sample a) D70 and sample b) A50

2.3.3 X-ray Diffraction (XRD)

The XRD patterns in **Figure 2.3** obtained for both D70 and A50 indicates a similar structure. The 2θ peak values at 28.0° , 47.3° and 56.1° for both samples correspond to (112), (200) and (312) planes of the established CZTS kesterite structure (JCPDS 27-0575),^{7, 13, 19} which is a vertically expanded zinc blend structure with sulfur occupying

half the tetrahedral holes and alternating CuSn/S/CuZn/S layers.²⁰ The NCs have similar characteristics to the nanowires/nanotubes¹⁵ but are very different with sphalerite-type NCs.¹⁶ The crystals have a tetragonal unit cell, with cell parameters of $a=b \neq c$ and internal angles all at 90° . It was found that $a = b = 4.51 \text{ \AA}$ and $c = 11.81 \text{ \AA}$ for both D70 and A50. These parameters are different from the reported results of $a = 5.40 \text{ \AA}$ and $c = 10.40 \text{ \AA}$.¹³ This difference may arise from variations in synthesis as well as the presence of the capping ligand MPP that may cause an elongation along the c direction, but closer packing in a and b directions. Also, for both samples, the absence of secondary structures was noted. This implies that the synthetic method employed allowed for the formation of a pure material.

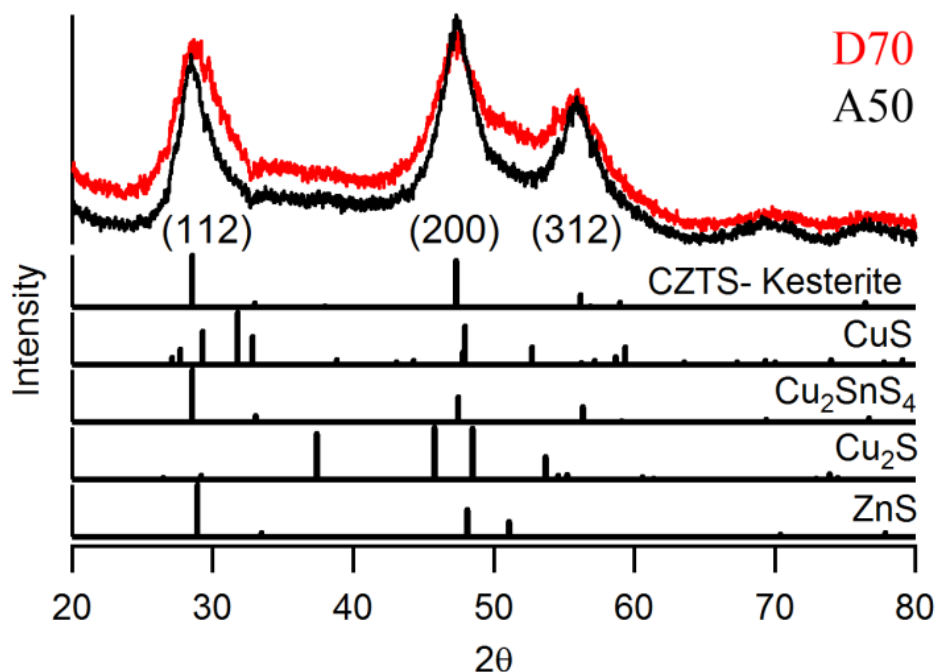


Figure 2.3 XRD patterns of D70 and A50 compared to JCPDS cards of CZTS, CuS, Cu₂SnS₄, Cu₂S and ZnS

The size of the NCs was determined from the Scherrer equation (**Equation 2.1**) to be 2 nm for both D70 and A50.²¹ Compared to the values obtained in both TEM and SEM, this is significantly smaller suggesting that the structures observed in those images are clusters of much smaller NCs. The size of NCs may have been the same between all samples tested, but the way the NC self-assembled differed between D70 and A50. The assembly of the NCs in A50 may inhibit photoconversion. While CZTS nanorod assembly in solution has been reported,²² our NCs have tendency to pack, leading to high photovoltaic effectiveness.¹²

$$D = \frac{K\lambda}{\beta_{1/2}\cos\theta} \quad \mathbf{2.1}$$

Where, K is the dimensionless crystallite shape factor with a value close to unity (0.94), λ is the wavelength of Cu K α X-ray, $\beta_{1/2}$ is the full width at half maximum of the selected peak, θ is the diffraction angle of the selected peak.

2.3.4 X-ray Photoelectron Spectroscopy (XPS)

Figure 2.4a shows the Cu 2p_{3/2} binding energies for D70 and A50. Cu(II) was able to be eliminated due to the absence of a peak at 934eV.²³ Since the binding energies for Cu(0) and Cu(I) are similar (932.63 eV and 932.18 eV), the modified Auger parameter was used to distinguish the copper oxidation state.²⁴⁻²⁵ The modified Auger parameter sums the kinetic energy of the Auger electron and the binding energy of the copper electron to give unique values of 1851.24 eV and 1849.17 eV for Cu(0) and Cu(I). In this way, it was determined that Cu(I) is present in both samples. **Figure 2.4b** illustrates the Zn 2p_{3/2} binding energies for D70 and A50 which identify its presence as Zn(II) based on literature values.²⁵⁻²⁶ **Figure 2.4c** shows the Sn 3d_{5/2} binding energy for D70 and A50.

Sn(IV) was determined as the oxidation state most likely present in the CZTS for both samples, given literature values for $3d_{5/2}$ binding energies.^{25, 27} **Figure 2.4d** depicts the $2p_{3/2}$ peaks for the sulfur in D70 and A50 as the form of S^{2-} .²⁸ An overall net zero charge on the CZTS via this synthetic method was concluded based on the oxidation states of all four elements.

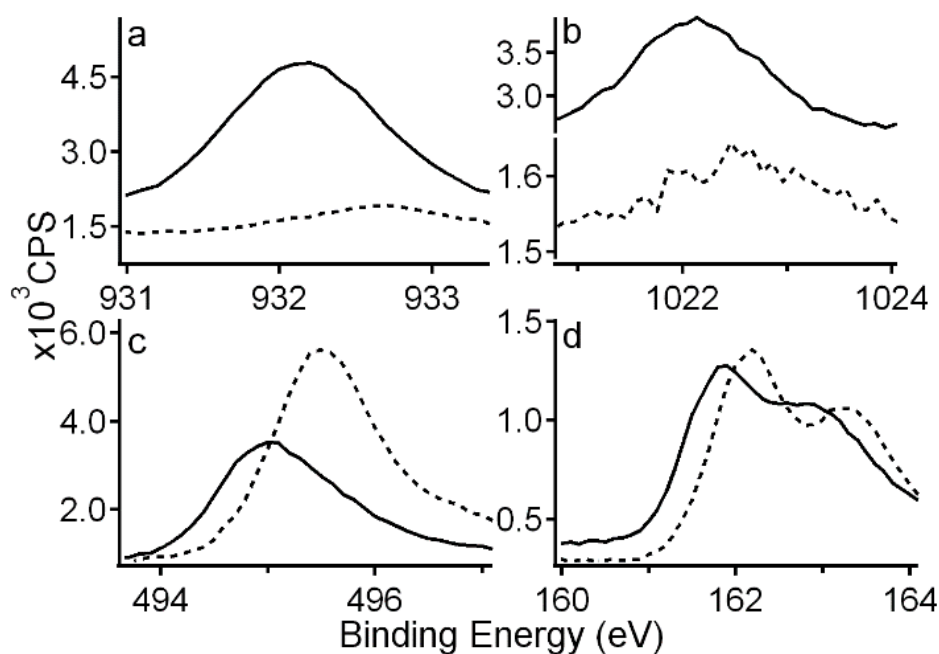


Figure 2.4 XPS spectra for D70 (solid lines) and A50 (broken lines). a) $2p_{3/2}$ Cu peaks, b) $2p_{3/2}$ Zn peaks, c) $3d_{5/2}$ Sn peaks and d) $2p_{3/2}$ S peaks.

The synthesis of D70 and A50 used initial ratios of 1.44:1.00:4.28:4.21 and 1.00:1.17:1.39:3.93 for copper, zinc, tin and sulfur, respectively. While EDX reveals the bulk compositions and XPS is more surface-sensitive, both were used. EDX gave molar ratios of 3.17:0.51:1.00:5.28 for D70 and 2.09:0.21:1.00:3.85 for A50. XPS determined molar ratios of 1.95:0.82:1.00:6.78 and 0.23:0.02:1.00:4.46 for D70 and A50, respectively. It can be seen that both samples had non-stoichiometric ratios. As well, the

Cu/(Zn+Sn) ratios for D70 were 0.27 for the starting ratios and >1 for the analytical methods. This differs from what is typically seen as a good ratio in the synthesis of CZTS.²⁹⁻³⁰ D70 was Cu-rich and Zn-poor in bulk, while the surface was slightly less so. Conversely A50 had more zinc initially, but was deficient in zinc on both the surface and in the bulk. This may shed light into the reasons behind the differences in its photovoltaic ability: the participation of the zinc in the photoresponse is limited by its concentration in the CZTS. This also shows that there may be both a limit to the amount of zinc that can be used initially as well as a dependency on how much zinc is necessary to provide a photoresponse.

2.4 Conclusions

In summary, CZTS NCs have been synthesized, for the first time, using a simple one-pot method without post annealing. PECMs were used as criteria for determining photovoltaic effectiveness. It was found that a starting ratio of approximately 1.5:1:4.3:4.2 for copper, zinc, tin and sulfur respectively, yielded the highest photoactivity. The oxidation states of the four elements were determined to be 1+, 2+, 4+ and 2- by XPS. The CZTS was in the kesterite structure with cell parameters of $a = b = 4.51 \text{ \AA}$ and $c = 11.81 \text{ \AA}$. The calculated NC size was determined to be 2 nm. NC sizes and configurations showed that self-assembly was a factor in the synthesis as their sizes were more than 20 times bigger. The synthetic method also yielded a pure product that was free of secondary phases.

2.5 References

(1) Harati, M.; Jia, J.; Giffard, K.; Pellarin, K.; Hewson, C.; Love, D. A.; Lau, W. M.; Ding, Z.; *Phys. Chem. Chem. Phys.*, (2010), 12, 15282-15290.

i. This chapter contains the work presented in Vaccarello, D. *et al. RSC Adv.* 2013, 3, 3512-3515

- (2) Shockley, W.; Queisser, H. J.; *J. Appl. Phys.*, (1961), 32, 510-519.
- (3) Todorov, T. K.; Reuter, K. B.; Mitzi, D. B.; *Adv. Mater.*, (2010), 22, E156-E159.
- (4) Barkhouse, D. A. R.; Gunawan, O.; Gokmen, T.; Todorov, T. K.; Mitzi, D. B.; *Prog. Photovoltaics*, (2012), 20, 6-11.
- (5) Scragg, J. J.; Dale, P. J.; Peter, L. M.; *Electrochem. Commun.*, (2008), 10, 639-642.
- (6) Madarasz, J.; Bombicz, P.; Okuya, M.; Kaneko, S.; *Solid State Ionics*, (2001), 141-142, 439-446.
- (7) Steinhagen, C.; Panthani, M. G.; Akhavan, V.; Goodfellow, B.; Koo, B.; Korgel, B. A.; *J. Am. Chem. Soc.*, (2009), 131, 12554-12555.
- (8) Guo, Q.; Hillhouse, H. W.; Agrawal, R.; *J. Am. Chem. Soc.*, (2009), 131, 11672-11673.
- (9) Yang, H.; Jauregui, L. A.; Zhang, G.; Chen, Y. P.; Wu, Y.; *Nano Lett.*, (2012), 12, 540-545.
- (10) Kameyama, T.; Osaki, T.; Shibayama, T.; Kudo, A.; Kuwabata, S.; Torimoto, T.; *J. Mater. Chem.*, (2010), 20, 5319-5324.
- (11) Khare, A.; Wills, A. W.; Ammerman, L. M.; Norris, D. J.; Aydil, E. S.; *Chem. Commun.*, (2011), 47, 11721-11723.
- (12) Redinger, A.; Berg, D. M.; Dale, P. J.; Siebentritt, S.; *J. Am. Chem. Soc.*, (2011), 133, 3320-3323.
- (13) Shavel, A.; Cadavid, D.; Ibanez, M.; Carrete, A.; Cabot, A.; *J. Am. Chem. Soc.*, (2012), 134, 1438-1441.
- (14) Panthani, M. G.; Akhavan, V.; Goodfellow, B.; Schmidtke, J. P.; Dunn, L.; Dodabalapur, A.; Barbara, P. F.; Korgel, B. A.; *J. Am. Chem. Soc.*, (2008), 130, 16770-16777.

- (15) Su, Z.; Yan, C.; Tang, D.; Sun, K.; Han, Z.; Liu, F.; Lai, Y.; Li, J.; Liu, Y.; *CrystEngComm*, (2012), 14, 782-785.
- (16) Dai, P.; Shen, X.; Lin, Z.; Feng, Z.; Xu, H.; Zhan, J.; *Chem. Commun.*, (2010), 46, 5749-5751.
- (17) Ye, H.; Akhavan, V. A.; Goodfellow, B. W.; Panthani, M. G.; Korgel, B. A.; Bard, A. J.; *J. Phys. Chem. C*, (2011), 115, 234-240.
- (18) Wei, W.; Lu, Y.; Chen, W.; Chen, S.; *J. Am. Chem. Soc.*, (2011), 133, 2060-2063.
- (19) Kumar, P.; Gusain, M.; Nagarajan, R.; *Inorg. Chem.*, (2011), 50, 3065-3070.
- (20) Kumar, P.; Nagarajan, R.; *Inorg. Chem.*, (2011), 50, 9204-9206.
- (21) Wu, J. M.; Chen, Y.-R.; *J. Phys. Chem. C*, (2011), 115, 2235-2243.
- (22) Singh, A.; Geaney, H.; Laffir, F.; Ryan, K. M.; *J. Am. Chem. Soc.*, (2012), 134, 2910-2913.
- (23) Fan, J.; Dai, Y.; Li, Y.; Zheng, N.; Guo, J. H.; Yan, X.; Stucky, G. D.; *J. Am. Chem. Soc.*, (2009), 131, 15568-15669.
- (24) Tsang, S.-W.; Fu, H.; Ouyang, J.; Zhang, Y.; Yu, K.; Lu, J.; Tao, Y.; *Appl. Phys. Lett.*, (2010), 96, 243104 1-3.
- (25) Liu, Q.; Zhao, Z.; Lin, Y.; Guo, P.; Li, S.; Pan, D.; Ji, X.; *Chem. Commun.*, (2011), 47, 964-966.
- (26) Yu, S. H.; Shu, L.; Yang, J.; Han, Z. H.; Qian, Y. T.; Zhang, Y. H.; *J. Mater. Res.*, (1999), 14, 4157-4162.
- (27) Shen, G.; Chen, D.; Tang, K.; Liu, X.; Huang, L.; Qian, Y.; *J. Solid State Chem.*, (2003), 173, 232-235.
- (28) Webber, D. H.; Brutchey, R. L.; *J. Am. Chem. Soc.*, (2011), 134, 1085-1092.

(29) Todorov, T. K.; Gunawan, O.; Chey, S. J.; de Monsabert, T. G.; Prabhakar, A.; Mitzi, D. B.; *Thin Solid Films*, (2011), 519, 7378-7381.

(30) Guo, Q.; Ford, G. M.; Yang, W.-C.; Walker, B. C.; Stach, E. A.; Hillhouse, H. W.; Agrawal, R.; *J. Am. Chem. Soc.*, (2010), 132, 17384-17386.

3 Dynamic Aspects of CuInS₂ Light Absorbing Nanocrystals Thin Films

Photoelectrochemical measurements (PECMs) of CuInS₂ (CIS) nanocrystal films (NCFs) on indium-doped tin oxide coated polyethylene terephthalate were carried out in an electrolyte solution. Intensity modulated photocurrent spectroscopy (IMPS) was performed at the NCF/solution interface. IMPS quantified the kinetic constants of the photoreaction. The rate ratio of the product separation to recombination increased as a function of applied potential, while the RC time constant decreased. Interfacial reaction kinetics of MV²⁺ and the CIS film was revealed by means of PECMs and IMPS. The interaction of the light absorbing CIS NCFs at a hole-rich interface allow for an understanding of what might happen at an analogous n-type junction.

3.1 Introduction

The CuIn_{1-x}Ga_xSe_yS_{2-y} (CIGS) absorber systems have been developed for thin-film photovoltaic (PV) devices, which may be limited in the long-term by the depletion of Te, Ga, and In resources along with the complexity of more than 4-body alloys. Copper indium disulfide (CuInS₂, CIS) and other alternative ternary copper sulfides based on Cu–Bi–S or Cu–Sb–S type materials are very attractive in the field of PV in which the ternary semiconductors have a desired band gap (1.54 eV) and high theoretical efficiency (28.5%).¹⁻⁴ While there are many different methods for the preparation of CIS, such as RF sputtering,⁵ thermal evaporation,⁶ and chemical vapour deposition,⁷ the scalability is quite limited. Much research has been done to increase the efficiency of these thin film solar cells while decreasing the cost of synthesis and production.⁸⁻¹¹ The characterization of the effectiveness of the absorbing layer before production of a full solar cell is crucial

to not only lowering the costs but also insuring the photovoltaic efficiency.

Photoelectrochemical measurements (PECMs) are simple to evaluate the light-absorbing layers without making a solar device.¹²⁻¹⁴ However, rates of recombination and product separation in addition to that of the electron transfer are important aspects in the understanding of all photochemical reactions.¹⁵

Herein we report a study of intensity modulated photocurrent spectroscopy (IMPS) of CIS prepared via a one-pot sulfurization of metal salts in correlation to PECMs. Both were conducted at an interface between the nanocrystal films (NCFs) deposited on indium tin oxide polyethylene terephthalate (ITO-PET) and a methyl viologen dichloride (MV^{2+}) solution. The photocurrent transients are interpreted to be dependent on the recombination process and minority carriers flowing to the surface, based on IMPS analysis. Photoresponse was found to rely on MV^{2+} concentrations as well. Information on the properties of a suitable n-type contact can be predicted from the interactions of the NCF and solution. Higher photovoltaic efficiency may be achieved if a corresponding n-type contact forms a junction with the NCF.

3.2 Experimental

3.2.1 Nanocrystal Synthesis and PECMs

The CIS nanocrystals with a stoichiometry of 1.00:0.52:1.32 for Cu:In:S were prepared based on an established one-pot method.¹² Once the nanocrystals were prepared, the thin films were produced by dropcasting 6 μ L of CIS dispersed in acetone at 20 g/L onto a cleaned ITO-PET surface of 10.1 mm². PECMs were performed using a three electrode system in a MV^{2+} electrolyte solution with 0.1 M KCl as a supporting electrolyte. A

saturated calomel reference, a platinum wire counter and a CIS/ITO-PET working electrode were immersed into the solution and chopped light from a 150 W Newport lamp with an AM 1.5D filter was irradiated onto the working electrode at 1/3 Hz. The working electrode was irradiated perpendicular to their orientation in the solutions, and the reference and counter electrodes were not in the light path. The concentrations of MV^{2+} were varied from 0.100, 0.050, 0.025 and 0.010 M. A linear voltage sweep was applied between 0.000 and -0.400 V at a scan rate of 5 mV/s, and the resulting photocurrent was measured. SEM was performed using a Hitachi S-4500 field emission microscope with a Quartz XOne EDX system at Surface Science Western.

3.2.2 IMPS

IMPS was conducted in a welled container with the CIS/ITO-PET on the bottom. The NCFs were face up and exposed to a solution of MV^{2+} whereas the bottom was exposed to an IVIUM ModuLight as a light source. A 20.0 mW/cm² white light source was used with a modulation amplitude of 2.4 mW/cm² and frequency between 100000 Hz and 1 Hz and measured with an IVIUM CompactStat. While similar methodologies have been used before on full solar cells, the NCF/solution interface has been explored in this case.¹⁶⁻¹⁷

3.3 Results and Discussion

3.3.1 Physical Identification of Films

The material produced through this synthesis has been previously characterized; its p-type characteristic, purity and structure have been identified.¹² Previous characterization of the prepared CIS through XRD, XPS and EDX have identified a chalcopyrite crystal

structure, oxidation states of Cu(I) and In(III) as well as a stoichiometry of 1.00:0.52:1.32 for Cu:In:S.¹² When dropcast, the nanocrystals formed ~50 nm clusters. These clusters produced a film on the ITO-PET which can be seen in **Figure 3.1**. While some areas tend to have slightly less aggregation of the clusters, the film is densely packed and around 1 μm thick.

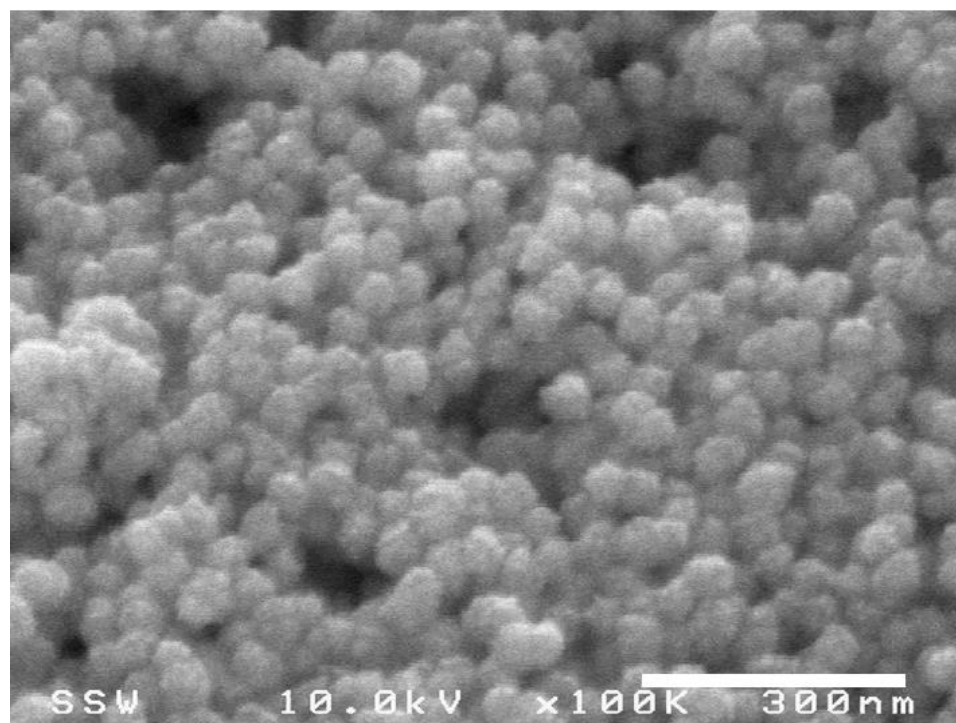


Figure 3.1 SEM image of a CIS sample dropcast on ITO-PET

3.3.2 PECMs and Photoreactions

The PECMs were utilized to characterize CIS films in a solution with $\text{MV}^{2+}/\text{MV}^{1+}$ redox couple as an electron acceptor. The current-potential behaviours of the system under illumination provide information of the reaction kinetics with respect to the photoresponse of CuInS_2 , i.e. information on the incident photon conversion as well as

valence and conduction band energies.¹⁵ **Figure 3.2** shows the typical PECMs of a CIS film at various MV^{2+} concentrations.

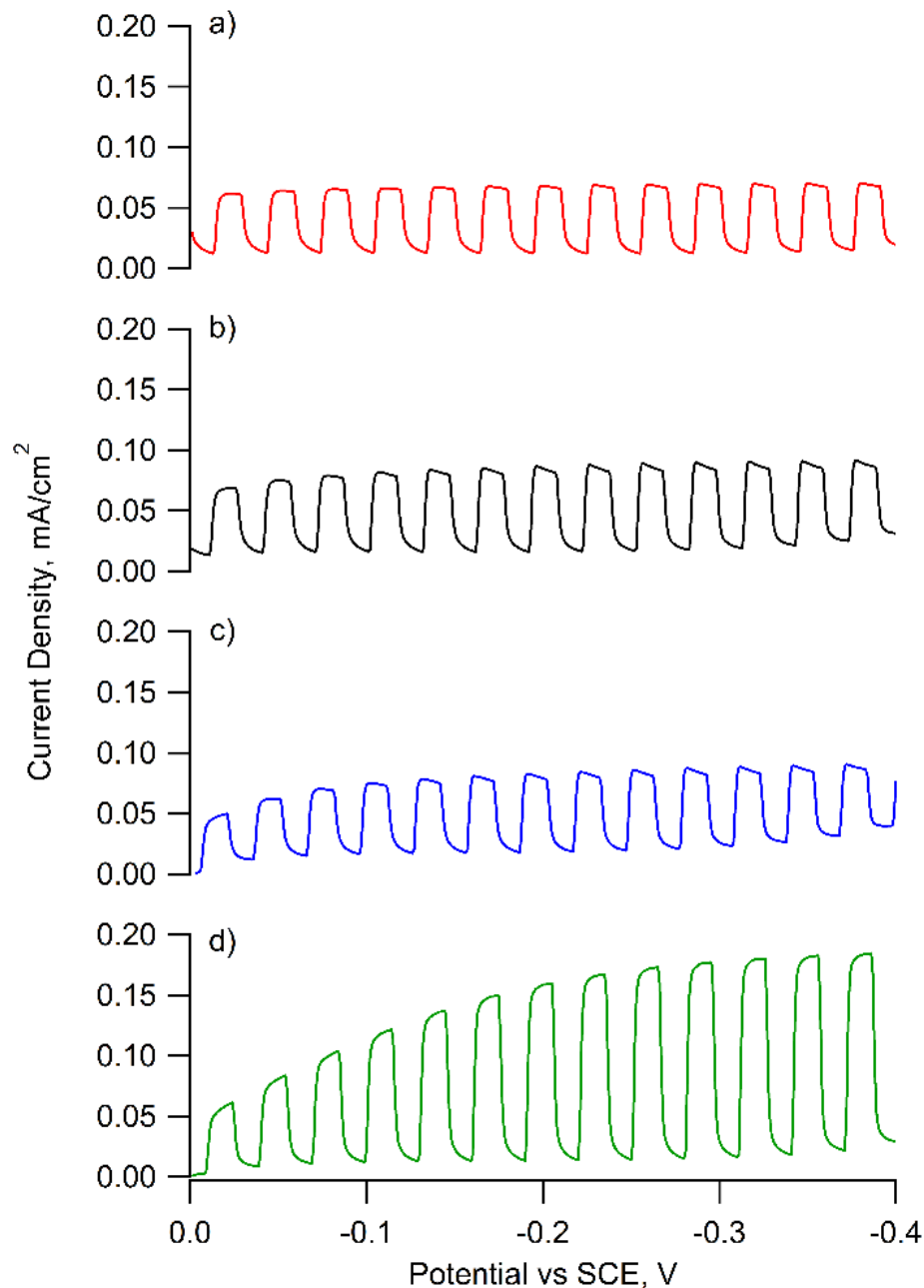
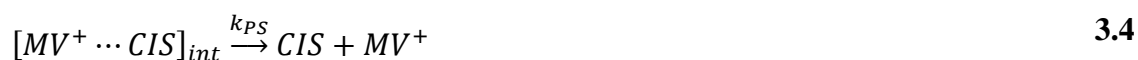


Figure 3.2 Linear sweep voltammograms of CuInS₂ under alternative illumination, in solutions of a) 0.010 M, b) 0.025 M, c) 0.050 M and d) 0.100 M MV^{2+} containing 0.1 M KCl. A scan rate of 5 mV/s was used with 1/3 Hz chopped light

When the CIS NCFs were illuminated by photons, a photogenerated electron was promoted into the conduction band; a corresponding hole was also produced from the removal of the electron (**Equation 3.1**).¹⁸⁻²⁰ The production of electrons by the p-type CIS, the minority carrier, resulted in a flow of these carriers towards the NCF/solution interface, described as the Gärtner flux (g_1).²¹⁻²² Once at the interface, the electrons formed an intermediate with MV^{2+} (**Equation 3.3**). This contributed to the initial increase of photocurrent when the light was turned on²³⁻²⁴. The intermediate species could also recombine with a hole present in the CIS to its ground state and form the original reagents (**Equation 3.4**) or the photogenerated electron can be transferred to the MV^{2+} (**Equation 3.5**). Assume that these processes have rate constants of k_R and k_{PS} , respectively. The recombination would decrease the current at a measurable rate $k_R[MV^{+}\cdots CIS^+]$. Product separation assumed the distance between the electron and hole too large for any reverse reaction to occur at a rate of $k_{ps}[MV^{+}\cdots CIS^+]$. The photogenerated electron and hole pair can conversely decay to form its ground state without current production (**Equation 3.2**). Other reactions may occur at the interface due to surface defects and contribute to recombination.



The first three transients in **Figure 3.2** follow the same general trend. In the photocurrent transients with 0.010 M MV^{2+} (**Figure 3.2a**), at more positive potentials there was almost no decrease after the initial excitation. This would indicate that the product separation reaction for the CIS is dominant over the recombination reaction. At more negative potentials, the photocurrent decreases after the initial photoexcitation. This would be due to the negative affect of recombination at the interface. After the light was turned off, the current density drops to a non-zero value without the conventional negative overshoot. It can be proposed that this is the result of the minority carrier diffusion to the interface. The current produced by this diffusion is not obvious under illumination since it is small compared to the initial photo-injection. In the dark, recombination is dominated by bulk states for sulfide-based photovoltaics.⁴ The diffusion of the photogenerated electron-hole pair to the surface in combination with the absence of a defined bulk may be the cause for the lack of overshoot as well as the gradual decrease in current. Moreover, the photocurrent consists of current produced by carrier generation inside the depletion layer as well as those generated in the bulk. The carriers that were able to pass through the space charge region also vary as a function of bias and can deviate from the norm in the negative bias.²³ As stated, the transients for the 0.025 and 0.050 M MV^{2+} (**Figure 3.2 b** and **c**) concentrations also share the same characteristics, however they are more pronounced. The trends discussed above still remain. The 0.100 M MV^{2+} transient does differ greatly (**Figure 3.2d**). The initial photoexcitation is punctuated by apparent diffusion current occurring under illumination, illustrating a slow increase after the initial sharp rise in photocurrent. This observation indicates the whole photoprocess is controlled by the diffusion.¹⁹ At lower negative potentials the working electrode

becomes a site where the positively charged MV^{2+} in solution begins to form a Schottky-junction. The increase in photocurrent with more negative potentials is due to the presence of excess MV^{2+} at the surface. The slow transfer can be seen in the gradual increase after initial photoexcitation to support this. A large driving force is required between the working and counter electrodes in order to overcome this. Even after reaching a plateau in the photocurrent maximum, the diffusion-driven photoresponse is still present, identifying the inability to overcome this diffusion.²⁵ The Schottky-junction formed between the CIS thin film and the MV^{2+} solution needs a higher negative overpotential in order to perform optimally.¹⁴ The CIS interface with the MV^{2+} is non-ideal, and a larger proportion of the potential change occurs across the Helmholtz layer.²⁶

3.3.3 IMPS Fitting and Correlation to PECMs

IMPS of inorganic thin films can identify charge transfer to and from the surface states present in the film as well as surface recombination.²⁷ IMPS was then performed on these thin films with the concentrations of MV^{2+} in order to quantify and compare the relative rates of recombination and product separation occurring at the NCF/solution interface across different applied potentials. In order to resolve the time constant, IMPS offers insight into the photoelectrochemical charge distribution across the NCF/solution interface. Although the NCF/solution interface would present a more complex circuit, the illuminated interface however can change the electronic structure.²⁸⁻²⁹ With this in mind, the virtual equivalent circuit can be represented through the interfacial capacitance and the uncompensated resistance based on its shape.²⁰ After the introduction of light, g_1 creates excess charge at the interface. It is at this point that the k_R and k_{PS} are responsible for the dissemination of charge under potentiostatic conditions. When the interface is

presented with periodic photon flux changes at different angular frequencies, the movement of photogenerated electron carriers is recorded through the photocurrent. The AC component of the photocurrent (j_1) is treated as a complex function of the angular frequency (ω).¹⁸ j_1 can be modeled with a virtual electronic circuit which has an equivalent frequency response.³⁰ The model used to map the AC component of the photocurrent was a resistor (R) and a capacitor (C) in series (**Figure 3.3**). In this model, j_1 can be described as a function of angular frequency, g_1 , k_{PS} , k_R as well as the resistance and the interfacial capacitance (**Equation 3.6**).¹⁹⁻²⁰



Figure 3.3 Virtual equivalent electronic circuit of a resistor and capacitor in series used for theoretical calculations

$$j_1 = g_1 \frac{k_{PS} + i\omega}{k_R + k_{PS} + i\omega} \left(\frac{1}{1 + RCi\omega} \right) \quad 3.6$$

The real, in-phase signal can be separated from the imaginary, out-of-phase, signal can be described as functions of ω as well (**Equations 3.7 and 3.8**). When this imaginary component is plotted as a function of the real, the ability to quantitatively represent the relative rates occurring at the surface occurs. This complex relationship shows the dependence of the photocurrent flux on the relative rates of product separation and recombination as well as how the shape of the IMPS peaks mathematically corresponds to the equation. At low frequencies, the response of the photocurrent is determined by the k_R and k_{PS} . When dominated by k_R , the shape of the IMPS response takes on a

circular shape. When k_{PS} is sufficiently larger, a semi-circular response is recorded. When both rates are relatively similar a shell-shaped response is observed. At higher frequencies the RC time constant plays a larger role in the shape of the response.²⁰

$$j_{photo}^e = g_1 \frac{k_{PS}(k_{PS} + k_R) + \omega^2(k_R RC + I)}{\left((k_{PS} + k_R)^2 + \omega^2\right) (1 + (RC\omega)^2)} \quad 3.7$$

$$j_{photo}^{img} = g_1 \frac{\omega(k_R - RC(k_{PS}k_R - k_{PS}^2 - \omega^2))}{\left((k_{PS} + k_R)^2 + \omega^2\right) (1 + (RC\omega)^2)} \quad 3.8$$

Figure 3.4 shows a set of the IMPS data for the NCF on ITO-PET immersed in the a) 0.010 M, b) 0.025 M, c) 0.050 M and d) 0.100 M MV^{2+} electrolyte solutions. The data was curve-fitted according to **Equations 3.7-8**, and the values for the rate constants were determined (Error! Reference source not found.).

Table 3.1 Average IMPS measurement ratios and their standard deviations for constants of photocurrent across all concentrations of MV^{2+}

Applied Potential (V)	k_{PS} (s^{-1})	k_R (s^{-1})	RC ($10^{-3}s$)	g_1 (10^{-3})
0.000	12.1±0.4	2.6±0.4	1.2±0.1	1.9±0.5
-0.100	12.8±0.2	6.5±0.2	1.1±0.1	2.0±0.5
-0.200	13.7±0.4	13.5±0.4	8.7±0.3	2.2±0.8
-0.300	14.3±0.1	25.7±0.1	16.3±0.1	2.4±0.7
-0.400	11.2±0.1	79.3±0.1	48.4±2.2	3.0±1.2

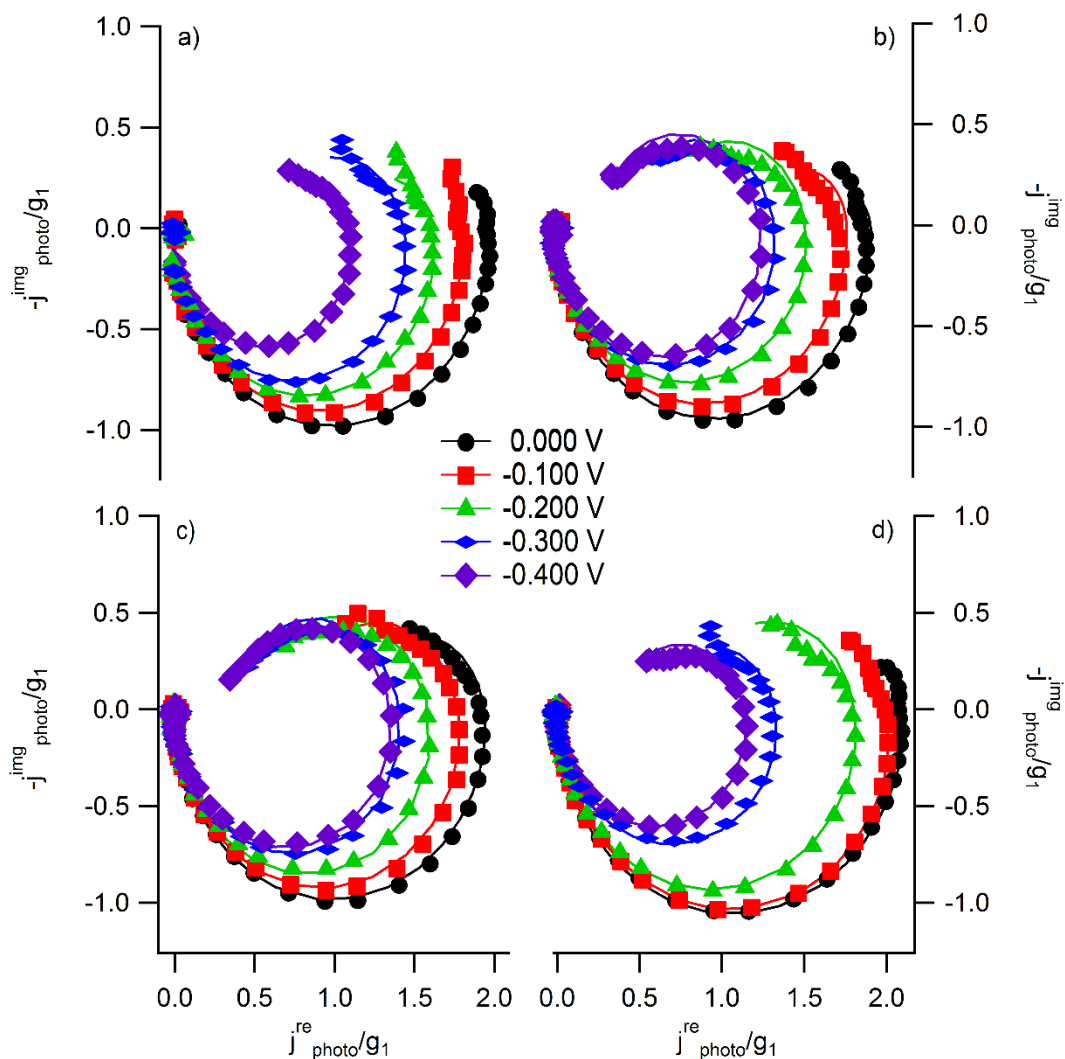


Figure 3.4 Complex representation of the IMPS data for the CuInS₂ nanocrystal film in (a) 0.010 M MV²⁺, (b) 0.025 M MV²⁺, (c) 0.050 M MV²⁺, and (d) 0.100 M MV²⁺ solutions at various applied potentials. The solid lines are the fitted results according to the theoretical calculations

The transients for the NCF/solution interface resemble calculated curves for simple RC circuits, confirming their use in the model for the photocurrent.²⁰ For the IMPS curves, at less negative potentials the rate of product separation is larger than the rate of recombination. This is represented in the semi-circular path of the data points. At more negative potentials, the k_R becomes larger and a spiral shape begins to form. This was

seen in the IMPS curves across all concentrations of MV^{2+} . This trend corresponded well with the PECM transients for 0.010, 0.025 and 0.050 M MV^{2+} and correlated well to the transients of the PECMs with exception for the 0.100 M IMPS transients. The PECM for 0.100 M MV^{2+} does not show the same pattern as the other concentrations. This is contrary to the IMPS transients at the same concentration, which follows a similar pattern as the lower concentrations of MV^{2+} . Error! Reference source not found. shows the average values of k_{PS} and k_R as well as the RC time constant over the applied potentials. The IMPS curve fitting data verifies higher k_{PS} rates relative to k_R from 0.000 V to -0.200 V on average. This can be seen in the PECM transients as only a small decrease in the photocurrent after the initial photo-injection. After -0.200 V the greater decrease in photocurrent after the initial photo flux occurs as a result of the k_R increasing relative to the k_{PS} . This pattern of decreasing in k_{PS}/k_R ratio is consistent across all concentrations of MV^{2+} . In the curve fitted data for the 0.100 M MV^{2+} IMPS measurement (**Figure 3.4**), there was an overall larger k_R relative to k_{PS} over the applied potentials. This is observed as the spiral shaped response at low negative potentials, but is not seen in the PECM transients however. PECMs reflect the possibility of enhanced photocurrent at this concentration of MV^{2+} , given that it may alter the lifetime of the photogenerated electron-hole pair or possibly change the impurity concentration at the interface.^{19, 23} This possible change in minority carrier lifetime as well as an unknown minority carrier diffusion length do not allow for the dependence of photocurrent on the band bending as described by the Gärtner equation to be resolved.^{23, 31} However, the Gärtner equation does not allow for accurate representation of the photocurrent in many experimental studies of semi-conductor electrodes, particularly around the flat band potential; this can

be seen as a decrease in photocurrent in this region.³²⁻³⁴ IMPS transients imply that the measurements and curve fitting can be a very useful tool in identifying the reaction kinetics at the interface, while PECMs can be dependent on the redox couple concentration in the solution.

The RC time constant increased with increased applied voltage, which can be seen in the transients as the upwards shift of the photocurrent across the applied voltage. This is contrary to CIS being reported as having a very small dependence of voltage for time constants and adds to the notion of other underlying factors contributing to the reaction kinetics.¹⁷ This change in the RC time constant could be also due to an increase in interfacial capacitance from compositional change at the surface.³⁵

As it can be seen in the lower concentrations' transients, the qualitative assessment of the photoprocesses can be quite accurate and correlate to the IMPS data. In bulk situations like the 0.100 M case however, the PECMs fail to correctly illustrate the processes occurring at the interface. The possibility of a diffusion of the excited state towards the interface may explain the enhancement of the photocurrent under illumination at 0.100 M MV^{2+} . It may also explain the non-negative and non-zero values for the photocurrent when illumination is interrupted. From this it can be seen that PECMs are very complementary to IMPS for low electrolyte concentrations (**Figure 3.5**). It should also be noted that IMPS is a powerful technique that can be used when PECMs are unable to describe the photoprocesses.

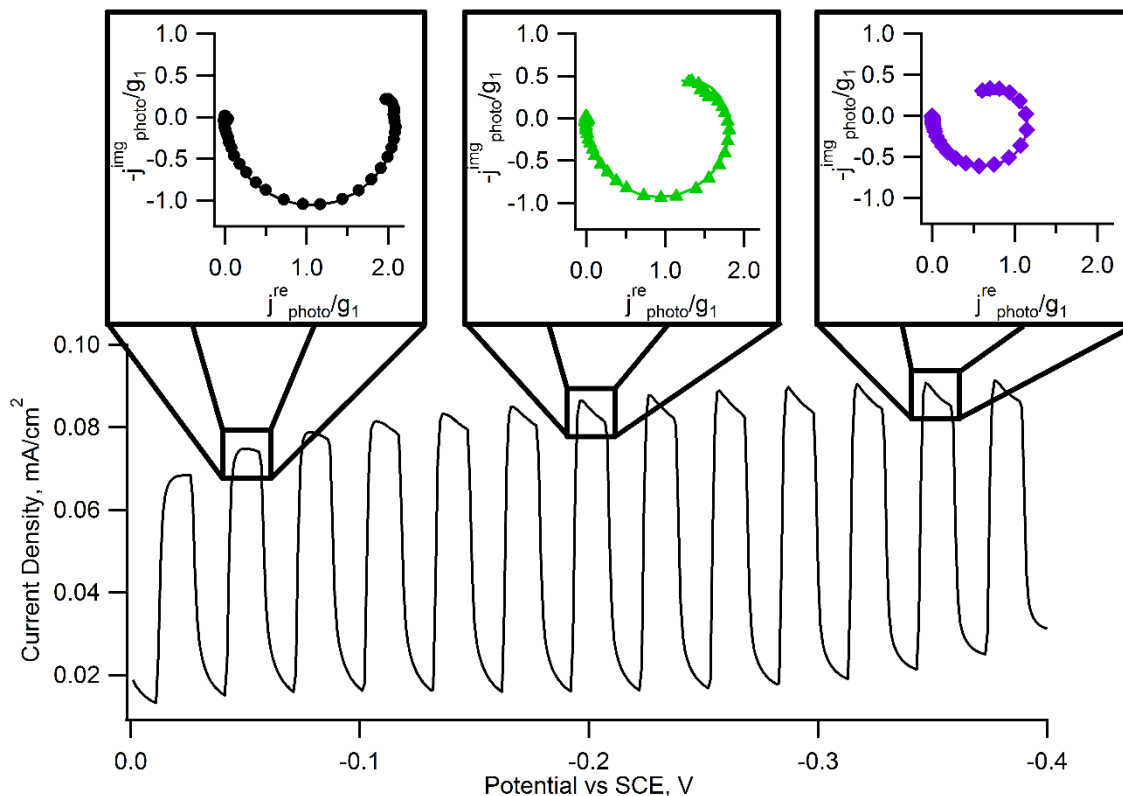


Figure 3.5 Graphical representation of the correlational relationship between PECM transients and the IMPS data collected at different applied potentials

3.4 Conclusions

CIS NCFs were photochemically characterized using both PECMs and IMPS, revealing interfacial reaction kinetics of MV^{2+} and the CIS film. Competition between product separation and charge recombination was observed in the IMPS. The ratio of the k_{PS} to k_R was found to decrease when the potential moved to more negative, while the RC time constant increases in the same course. These can be confirmed in the PECMs with a decrease in photocurrent after photo-injection as the potential was more negative.

Upward shifts in both photocurrent and dark current followed. An enhancement effect has been demonstrated in the PECMs and concentration dependence in photocurrent response has been established. Both methods in conjunction were able to provide

dynamic insight into the interfacial reactions of CuInS₂ and MV²⁺, as well as an idea of the properties an n-type contact would need in order to minimize loss due to recombination. Our understanding will be very useful for other types of devices such as photoelectrochemical hydrogen generation and Li batteries using CuInS₂ nanostructures.³⁶⁻³⁷

3.5 References

- (1) Shay, J. L.; Wernick, J. H. *Ternary Chalcopyrite Semiconductors: Growth, Electronic Properties and Applications*; Pergamon Press: New York, 1975.
- (2) Dufton, J. T. R.; Walsh, A.; Panchmatia, P. M.; Peter, L. M.; Colombara, D.; Islam, M. S.; *Phys. Chem. Chem. Phys.*, (2012), 14, 7229.
- (3) Colombara, D.; Peter, L. M.; Hutchings, K.; Rogers, K. D.; Schäfer, S.; Dufton, J. T. R.; Islam, M. S.; *Thin Solid Films*, (2012), 520, 5165-5171.
- (4) Siebentritt, S.; *Thin Solid Films*, (2002), 403-404, 1-8.
- (5) Genevee, P.; Donsanti, F.; Renou, G.; Lincot, D.; *J. Phys. Chem. C*, (2011), 115, 17197-17205.
- (6) Peter, L. M.; *J. Phys. Chem. Lett.*, (2011), 2, 1861-1867.
- (7) Wang, Y.-H. A.; Zhang, X.; Bao, N.; Lin, B.; Gupta, A.; *J. Am. Chem. Soc.*, (2011), 133, 11072-11075.
- (8) Shi, X.; Xi, L.; Fan, J.; Zhang, W.; Chen, L.; *Chem. Mater.*, (2010), 22, 6029-6031.
- (9) Fischer, C.; Muffler, H.-J.; Bär, M.; Kropp, T.; Schönmann, A.; Fiechter, S.; Barbar, G.; Lux-Steiner, M. C.; *J. Phys. Chem. B*, (2003), 107, 7516-7521.

- (10) Panthani, M. G.; Akhavan, V.; Goodfellow, B.; Schmidtke, J. P.; Dunn, L.; Dodabalapur, A.; Barbara, P. F.; Korgel, B. A.; *J. Am. Chem. Soc.*, **(2008)**, *130*, 16770-16777.
- (11) Sheng, X.; Wang, L.; Chang, L.; Luo, Y.; Zhang, H.; Wang, J.; Yang, D.; *Chem. Commun.*, **(2012)**, *48*, 4746-4748.
- (12) Tapley, A.; Vaccarello, D.; Hedges, J.; Jia, F.; Love, D. A.; Ding, Z.; *Phys. Chem. Chem. Phys.*, **(2013)**, *15*, 1431-1436.
- (13) Vaccarello, D.; Tapley, A.; Ding, Z.; *RSC Adv.*, **(2013)**, *3*, 3512-3515.
- (14) Ye, H.; Akhavan, V. A.; Goodfellow, B. W.; Panthani, M. G.; Korgel, B. A.; Bard, A. J.; *J. Phys. Chem. C*, **(2011)**, *115*, 234-240.
- (15) Liou, Y.-J.; Hsiao, P.-T.; Chen, L.-C.; Chu, Y.-Y.; Teng, H.; *J. Phys. Chem. C*, **(2011)**, *115*, 25580-25589.
- (16) Byers, J. C.; Ballantyne, S.; Rodionov, K.; Mann, A.; Semenikhin, O. A.; *ACS Appl. Mater. Interfaces*, **(2011)**, *3*, 392-401.
- (17) Grasso, C.; Nanu, M.; Goossens, A.; Burgelman, M.; *Thin Solid Films*, **(2005)**, *480-481*, 87-91.
- (18) Peter, L. M.; *Chem. Rev.*, **(1990)**, *90*, 753-769.
- (19) Schaming, D.; Hojeij, M.; Younan, N.; Nagatani, H.; Lee, H. J.; Girault, H. H.; *Phys. Chem. Chem. Phys.*, **(2011)**, *13*, 17704-17711.
- (20) Fermin, D. J.; Duong, H. D.; Ding, Z. F.; Brevet, P. F.; Girault, H. H.; *Phys. Chem. Chem. Phys.*, **(1999)**, *1*, 1461-1467.
- (21) Li, J.; Peter, L. M.; *J. Electroanal. Chem.*, **(1985)**, *193*, 27-47.
- (22) Ahmed, A. Y.; Oekermann, T.; Lindner, P.; Bahnemann, D.; *Phys. Chem. Chem. Phys.*, **(2012)**, *14*, 2774-2783.

- (23) Gärtner, W.; *Phys. Rev.*, **(1959)**, *116*, 84-87.
- (24) Peat, R.; Peter, L. M.; *J. Electroanal. Chem.*, **(1987)**, *228*, 351-364.
- (25) Loutfy, R. O.; McIntyre, L. F.; *Can. J. Chem.*, **(1982)**, *61*, 72-77.
- (26) Peter, L. M.; *J. Solid State Electrochem.*, **(2012)**, *17*, 315-326.
- (27) DiCarmine, P. M.; Semenikhin, O. A.; *Electrochim. Acta*, **(2008)**, *53*, 3744-3754.
- (28) Cummings, C. Y.; Marken, F.; Peter, L. M.; Tahir, A. A.; Wijayantha, K. G.; *Chem. Commun.*, **(2012)**, *48*, 2027-9.
- (29) Heidari-pour, A.; Jafarian, M.; Gobal, F.; Mahjani, M. G.; Miandari, S.; *J. Appl. Phys.*, **(2014)**, *116*, 034906 1-7.
- (30) Savenije, T.; Goossens, A.; *Phys. Rev. B*, **(2001)**, *64*, 115323-115332.
- (31) Batchelor, R. A.; Hamnett, A. *Surface States on Semiconductors*; Springer: New York, N.Y., 1992.
- (32) Peter, L. M.; Li, J.; Peat, R.; *Electrochim. Acta*, **(1990)**, *35*, 1657-1664.
- (33) Peter, L. M.; Ponomarev, E. A.; Fermin, D. J.; *J. Electroanal. Chem.*, **(1997)**, *427*, 79-96.
- (34) Brahim, R.; Trari, M.; Bouguelia, A.; Bessekhoud, Y.; *J. Solid State Electrochem.*, **(2009)**, *14*, 1333-1338.
- (35) Peat, R.; Riley, A.; Williams, D. E.; Peter, L. M.; *J. Electrochem. Soc.*, **(1989)**, *136*, 3352.
- (36) Ma, G.; Minegishi, T.; Yokoyama, D.; Kubota, J.; Domen, K.; *Chem. Phys. Lett.*, **(2011)**, *501*, 619-622.
- (37) Zhou, W.-H.; Zhou, Y.-L.; Feng, J.; Zhang, J.-W.; Wu, S.-X.; Guo, X.-C.; Cao, X.; *Chem. Phys. Lett.*, **(2012)**, *546*, 115-119.

4 Photoelectrochemical and Physical Insight into $\text{Cu}_2\text{ZnSnS}_4$ Nanocrystals Using Synchrotron Spectroscopy

$\text{Cu}_2\text{ZnSnS}_4$ (CZTS) nanocrystals were synthesized via a one-pot method and photoelectrochemical measurements (PECMs) of the CZTS films were quantitatively compared. Based on their initial metal stoichiometry and photoresponse behavior, CZTS films were divided into groups of high-photoresponse (hp-CZTS) and low-photoresponse samples (lp-CZTS). An X-ray absorption near-edge structure (XANES) study was then performed to unravel the origin of the difference in their photovoltaic properties. The results demonstrated that, the local structures of the elements and their interaction with capping ligands are different and strongly affect the photovoltaic behavior, although both CZTS groups through one-pot synthesis were free of secondary phases. It was determined that the coordination of Zn and the capping ligand-metal interaction are the two major factors for the production of higher photocurrent. The correlations will guide us to produce viable CZTS films crucial for the development of solar energy conversion.

4.1 Introduction

The need for a sustainable and renewable energy source is becoming more apparent as current fossil reserves deplete. The sun provides a source of energy that is abundant as well as persistent. The development of efficient solar energy materials is driven by this need, allowing for many options on harvesting sunlight.¹⁻² Single junction photovoltaics are still far away from their theoretical efficiency limits, while multi-junction devices have gone beyond 43 %.² The additional limiting factor in many cases is the economic

i. This chapter contains the work presented in Vaccarello, D. *et al. J. Phys. Chem. C.* **2015**, 119 (21), 11922-8

practicality of the synthesis as well as the ability to scale up the process for terawatt applications.

$\text{Cu}_2\text{ZnSnS}_4$ (CZTS) is a quaternary kesterite material with a desirable direct energy band gap between 1.45-1.51 eV, allowing it to be a viable option for absorbing layers in photovoltaic devices.³ Combined with a high optical absorption coefficient of 10^4 cm^{-1} , a readily available supply of source elements and being a non-toxic absorber, CZTS solar cells have been able to reach efficiencies as high as 10 %.⁴⁻⁷ There are other different ways of producing CZTS films,⁷⁻¹⁵ leading to variations in both their quality and viability for use in photovoltaic devices.

The kesterite crystal lattice (**Figure 4.1**) has a space group of $I\bar{4}$. Copper occupies the 2c and 2a lattice positions, zinc and tin atoms occupy the 2b and 2d lattice positions respectively and sulfur occupies the 8g lattice position.¹⁶ With this in mind, the ability for secondary structures to evolve is prevalent and is often a cause for problems in the effectiveness of CZTS as a light-absorbing layer in photovoltaic devices.^{3, 17-18} While the detection of secondary structures using X-ray diffraction is well established, the diffraction patterns do not fully confirm the kesterite structure as free of secondary phases. The diffraction patterns tended to be broad and could not definitively differentiate between kesterite and possible secondary phases such as ZnS and CuS.¹⁹⁻²⁰ The chemical potential for CZTS to be synthesized without the presence of secondary phases has been shown to be small and resulted in a range of reported band gap energies for kesterite CZTS.^{3, 21} For the reasons described above, the use of X-ray absorption near-edge spectroscopy (XANES) allows for the analysis of specific atoms in specific states.

i. This chapter contains the work presented in Vaccarello, D. *et al. J. Phys. Chem. C.* **2015**, 119 (21), 11922-8

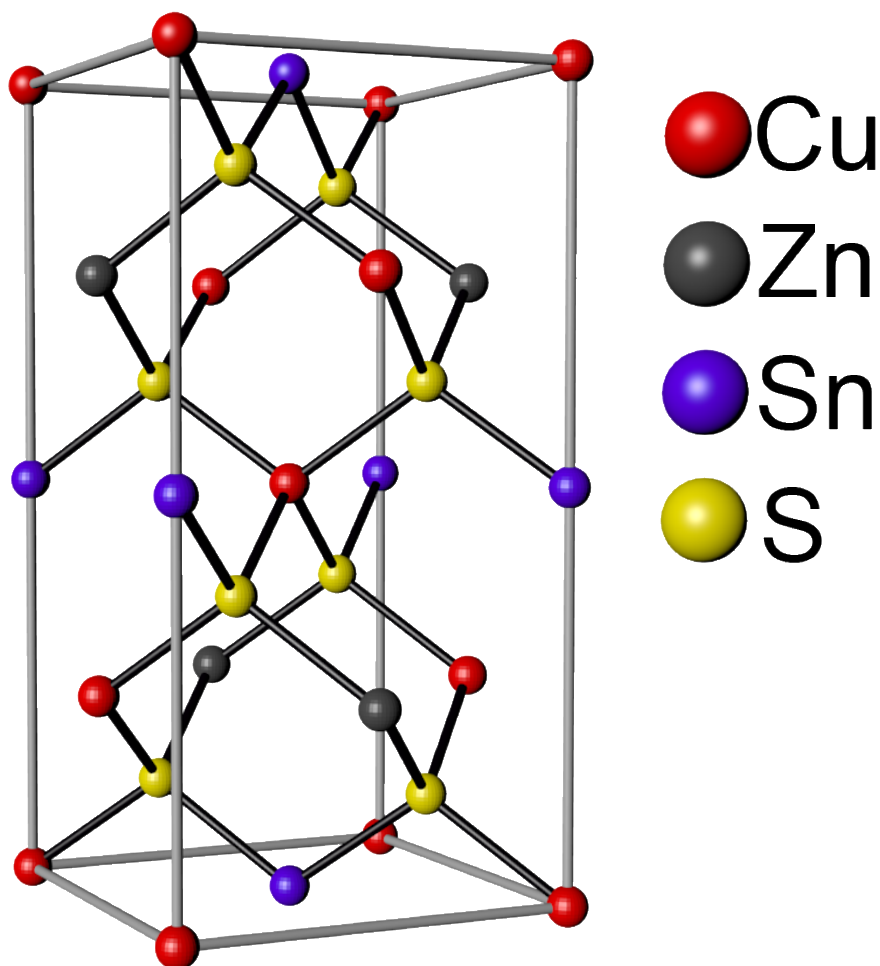


Figure 4.1 Kesterite CZTS lattice with an $I\bar{4}$ space group

XANES is an element, excitation channel and chemically sensitive technique that tracks the local structure and bonding of any given atom in a chemical environment by measuring the absorption coefficient across an absorption edge of a core level of the element of interest (similar to UV-visible spectroscopy except that the initial state is an atomic orbital, not a molecular orbital). The elemental and chemical sensitivities come about because each and every element has its own characteristic absorption edge (binding energy of core electrons) and the transition is dipole, i.e. that we can probe the unoccupied electronic state of p character by exciting the 1s electron at the K-edge, etc. and the unoccupied electronic states are established by the molecular potential set up by

the surrounding atoms. Since core levels are tighter bound, XANES requires the use of tunable X-rays from the synchrotron.

There has been well-documented use of comparison with the S K-edge in order to determine the presence of secondary phases.²²⁻²³ The probing of other edges could give insight into variations in performance of the CZTS as an absorbing layer as well as possibly corroborate S K-edge findings.

Probing local environments of the atoms in CZTS is important for more than just elucidation of secondary structures; for the one-pot solvothermal synthesis method we have developed, it is also essential in identifying the factors that determine the CZTS layer's photoresponse.¹³ Possible factors affecting the photoresponse in such a complex quaternary material may include the composition, the coordination of atoms or crystal-phase homogeneity. A variation in our synthetic method from classical CZTS preparation is the use of the capping ligand, 2-mercapto-5-n-propylpyrimidine (MPP, **Figure 4.2**). The MPP can act as both a terminating ligand in the formation of the nanocrystal clusters and a possible source of sulfur source to be used within the CZTS itself. It also acts as a surfactant that aids in the increased solubility of metal salts in the synthetic process. The interaction of the thiol and the pyrimidine ring in MPP with the CZTS has yet to be explored and can affect the photoresponse and electronic properties of the nanocrystals the ligand caps. These can be very helpful in choosing the right starting ratios for the one-pot synthesis. Herein, the compositions and purity of the CZTS produced by our synthesis were tested, as well as the effect of the capping ligand on nanocrystal stability and photoresponse. It is essential to obtain insight into this structure-property relationship that guides the construction of full solar devices.

i. This chapter contains the work presented in Vaccarello, D. *et al. J. Phys. Chem. C.* **2015**, 119 (21), 11922-8

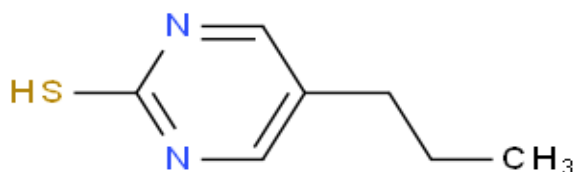


Figure 4.2 2-mercapto-5-n-propylpyrimidine capping ligand structure

4.2 Experimental

4.2.1 Nanocrystal Preparation

CZTS NCs were prepared via a one-pot synthesis.⁸ Briefly, metal precursor salts of copper, zinc and tin were used in varying combinations: copper(II) acetylacetonate (Aldrich Chemistry 97%), copper (II) sulfate (Fluka 99%), copper (I) chloride (Aldrich Chemistry 99%), zinc(II) chloride, zinc(II) oxide (Aldrich Chemistry 99%), (Aldrich Chemistry 99.99%), tin(II) chloride, (Aldrich Chemistry 99%), tin(II) sulfate (Aldrich Chemistry $\geq 95\%$) in varying molar ratios. Thiourea (Fluka 99.0%) was the source of sulfur and was kept constant at 1.2×10^{-4} M. 2-mercapto-5-propylpyrimidine (MPP) was used as both a surfactant and a capping ligand for the CZTS nanocrystals (NCs). The CZTS NCs were purified through centrifugation and washing with acetone. The dried NCs were weighed and dispersed in acetone with a concentration of 20 g/L. Two 6 μ L drops of the dispersed NCs were dropcast onto a 10.02 mm² area on an indium-doped tin oxide coated polyethylene terephthalate (ITO-PET, Aldrich Chemistry) with a drying time of 5 minutes between each addition.

4.2.2 Photoelectrochemical Set-up

Photoelectrochemical measurements (PECMs) were used in order to analyze the performance of the light-absorbing layers relative to one another.⁸ The photocurrent was

i. This chapter contains the work presented in Vaccarello, D. *et al. J. Phys. Chem. C.* **2015**, 119 (21), 11922-8

used as a basis for comparison in order to determine the optimal starting combinations. Utilizing an electrolyte solution of 0.1 M methyl viologen (MV^{2+}) dichloride (Aldrich, 98%) containing 0.1 M KCl as a solution-phase oxidant substituting for an n-type contact and junction.²⁴ The PECMs were conducted using a 150 W Newport lamp with an AM 1.5D filter, a ThorLabs SC10 shutter was used to produce a square wave light stimulus to the system, and a CHI 832a potentiostat (CH Instruments, Austin TX). A resistive polyimide tape was used as a mask to ensure a constant area for the working electrode. The electrode was submerged in the MV^{2+} electrolyte solution. A standard calomel electrode (SCE) and a platinum coil were used as reference and counter electrodes, respectively. Current was measured versus applied potential in a linear sweep from 0.000 V to -0.400 V while the chopped light was directed onto the NC film area at a frequency of 0.333 Hz.^{8, 25} From this method, the determination of high photoresponse CZTS (hp-CZTS) and low photoresponse CZTS (lp-CZTS) was possible. Both hp- and lp-CZTS were analyzed using various techniques.

4.2.3 Synchrotron Beamlines

Synchrotron spectroscopic measurements were conducted at the Canadian Light Source. Experiments were performed at two beamlines: the high resolution spherical grating monochromator (SGM, 11ID-1) and the soft X-ray microcharacterization (SXRMB, 06B1-1) beamlines. SGM provides a soft X-ray energy from 250 eV to 2000 eV with a resolution ($E/\Delta E$) of >5000 ²⁶, which is for the Zn L_3 - and N K-edge XANES measurements. The S K-edge XANES spectra were measured at the SXRMB beamline, which has an energy range of 1.7-10 keV and resolution of ~ 3000 .²⁷ The samples were dispersed on a double-sided carbon taped and mounted 45° toward the incident X-ray

beam. XANES spectra at SGM beamline were obtained in total electron yield (TEY) mode which is surface sensitive, and X-ray fluorescence yield (FY) mode, which is relatively bulk sensitive. The TEY measures specimen current resulted from photoelectrons, Auger electrons and secondary electrons, while FY collects total X-ray fluorescence using a channel plate detector. XANES at SXRMB beamline were obtained using the TEY mode. All spectra were normalized to incident photon flux (I_0).

4.2.4 Physical Characterization

The sample stoichiometry was investigated using energy dispersive X-ray spectroscopy (EDX); morphology and size were examined using scanning electron microscopy (SEM). Both SEM and EDX were performed using a Hitachi S-4500 field emission electron microscope with a Quartz XOne EDX system at Surface Science Western.

4.3 Results and Discussion

4.3.1 Physical and Stoichiometric Evaluation of PECM Response in CZTS Thin Films

The CZTS NC films were evaluated using the photoresponse in the transients of PECMs, **Figure 4.3a**. One of the advantages of PECMs is to ensure that a high photoresponse was present in the film before moving further to create a full photovoltaic device. The stoichiometry was of initial concern due to CZTS NC production using highly varied starting reagent ratios. It had been determined that a wide range of these ratios could produce the CZTS NC end product with a diverse range in the photoresponse.⁸ Insight into the composition-performance correlation for the CZTS NCs is desirable in the determination of an effective light-absorbing layer. **Figure 4.3a** shows exemplar PECM photoresponse transients of hp- and lp-CZTS NC films in a linear potential sweep under

chopped illumination. Hp-CZTS is characterized by the large difference between the dark current and photocurrent. By plotting the photocurrent density as a function of initial concentrations of metal salts, areas of hp- and lp-CZTS can be determined from the current density in the ternary contour plot (**Figure 4.3b**). Over 500 different combinations were tested and several regions can be seen to produce hp-CZTS. This is an important part in refining the synthesis and adapting it to best suit the development of this absorbing layer.

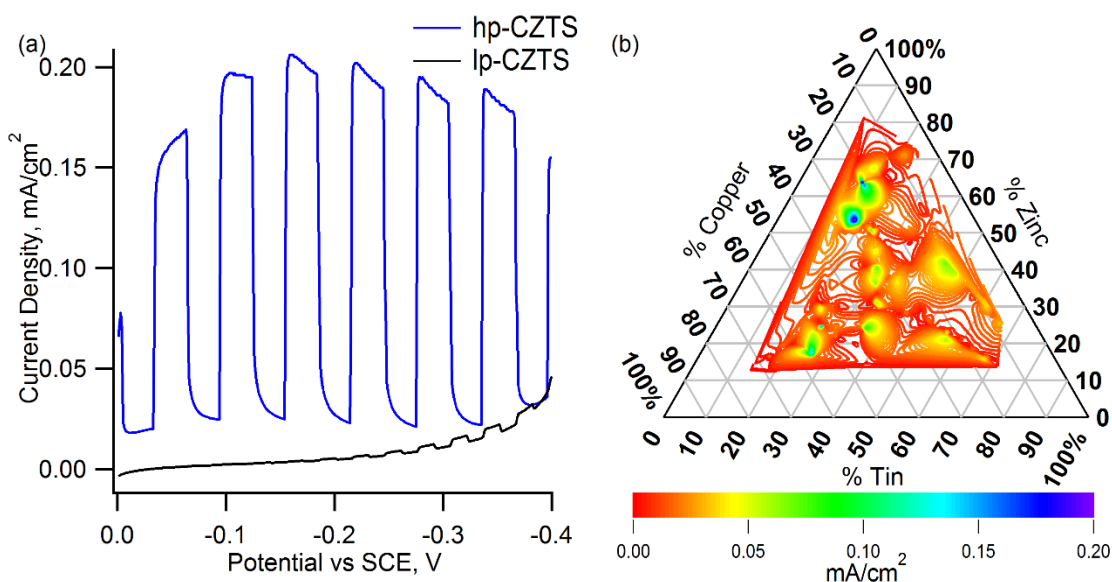


Figure 4.3 a) Exemplar PECM photoresponse transients of hp- and lp-CZTS NC films in a linear potential sweep under chopped illumination; and b) ternary contour plot representing the percentages of copper, tin and zinc with respect to the photocurrent of the resultant nanocrystals. The contour is a polynomial interpolation of the data points

From this graph it can be seen that the photocurrent of the NCs produced in the synthesis is a function of the initial ratios of metal salts used. Sulfur was omitted because it was

always in excess in the syntheses. There have been a few studies on the relationships between metal ratios and stoichiometries that produce secondary phases.^{4, 25, 28-29} Comparative ratios for copper, tin and zinc that are indicative of higher quality CZTS that are utilized in solar cells achieving high efficiencies differ greatly.²⁸ Typically the Cu/(Zn+Sn) is expected to be between 0.9-0.96 and the Zn/Sn around 1.1.²⁸ Comparatively, the most prominent areas of hp-CZTS from the synthesis were found in the higher initial ratios of zinc between 55-70%. The EDX results showed that the stoichiometry and initial ratios were not concerted throughout the reaction. For the hp-CZTS, initial Cu/Sn+Zn and Zn/Sn ratios were 0.4 and 3.1, which differed greatly from their EDX values of 1.3 and 0.5. Similarly for lp-CZTS, the ratios changed from initial values of 0.7 and 1.6 to the final ones of 2.2 and 0.2. The most notable of the changes in initial and final ratios were the differences in the presence of zinc. While both hp- and lp-CZTS had more zinc initially, lp-CZTS showed very little zinc in the final product. The SEM images of both hp- (**Figure 4.4a**) and lp-CZTS (**Figure 4.4b**) illustrate the physical differences between the films as well as the NC sizes that are common to each throughout the samples studied. Hp-CZTS NCs show an average size of 60 nm while lp-CZTS ones displayed a smaller size of 30 nm. As well, the two samples do not appear to be single NCs, but clusters,⁸ with the lp-CZTS ones exhibiting less crystallinity. It is plausible that Zn-deficient CZTS NCs have a similar detriments on the photovoltaic effect as a large excess of Zn.³⁰

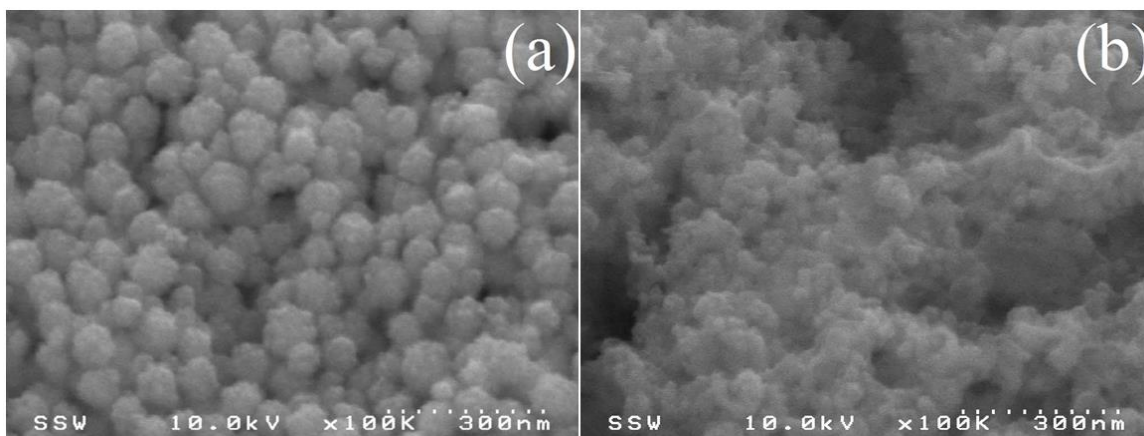


Figure 4.4 SEM images of (a) hp-CZTS and (b) lp-CZTS

The initial ratios of Cu:Zn:Sn for the best performance hp-CZTS occurs at 0.3:0.5:0.2. When compared with other ternary phase diagrams, these ratios typically describe areas in which secondary phases would likely occur.^{10, 21, 23, 31} The evolution of secondary phases is detrimental to CZTS in terms of stability, structure and photoactivity. Powder X-ray diffraction (XRD) was initially utilized to compare the diffraction patterns of the CZTS samples and known secondary phases in order to determine their presence.⁸ However the broad diffraction patterns could not definitively differentiate between kesterite and possible secondary phases such as ZnS and CuS. The use of transmission electron microscopy (TEM) and selected area electron diffraction (SAED) in combination with XRD has been found useful in differentiating closely related CuInS₂ phases.³² Unfortunately SAED and TEM comparisons of CZTS, were unable to discern kesterite from stannite or ZnS produced from this synthesis.¹⁹

4.3.2 Zn L₃-Edge

Figure 4.5 compares the XANES of hp-CZTS and lp-CZTS at the Zn L₃-edge. The spectrum of hexagonal wurtzite ZnS crystal powder was plotted as a reference. The local

structures of Zn in the two CZTS materials display great divergence. Zn L₃-edge probes the electronic transition of Zn 2p_{3/2} electrons to the unoccupied electronic states containing s and d characters. Zn metal has an electronic configuration of 4s²3d¹⁰, and due to the full d band, the spectra usually show broad resonances beyond the absorption edge (Fermi level).³³⁻³⁵

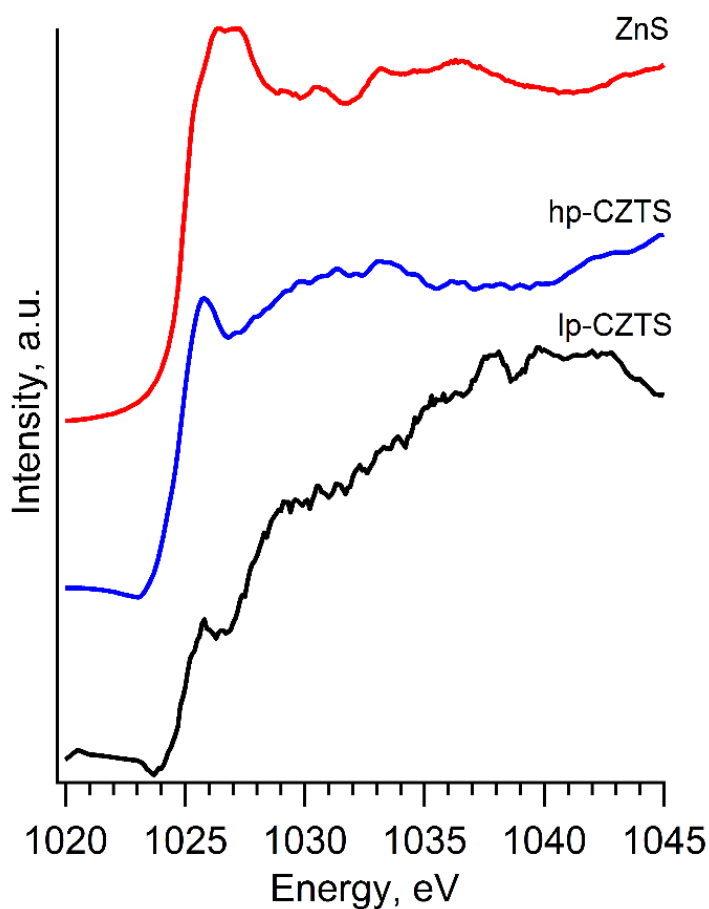


Figure 4.5 Zn L₃-edge XANES (FY) of lp-CZTS and hp-CZTS in comparison with ZnS

In ZnS, the shoulder feature right above the edge jump corresponds to the transition from the core to 4s orbital in the valence band, and the main resonance is from the transition to 4s-3d derived electronic states. The feature is broadened by S 3p and Zn 4s, 4p and 3d

hybridization (wurtzite band structure). In hp-CZTS nanocrystals, on the other hand, the spectrum only shows a weak narrow peak above edge, beyond which is more or less featureless. It suggests that the interaction between Zn and S in hp-CZTS is significantly different from the one in ZnS, in that the unoccupied densities of states are more localized in hp-CZTS. The hybridization between Zn 4s, 4p, 3d and S 3p is much weaker in the CZTS. In other words, the local chemical environment of Zn in hp-CZTS is different from the one in a ZnS lattice, a desirable result, since avoiding the production of ZnS in hp-CZTS would be beneficial to the overall stability of the CZTS as an efficient absorbing layer.^{3, 21} The observed feature in XANES provides clear evidence that there is no detectable ZnS secondary phase in hp-CZTS. The lp-CZTS displays a similar feature as hp-CZTS, but with a low signal-to-noise ratio. It is due to the intrinsic low Zn concentration, consistent with the EDX results. In addition, the spectral feature of lp-CZTS is broadened compared to hp-CZTS. This also indicates that Zn in lp-CZTS is in a highly disordered environment.

The EDX results show that in lp-CZTS, the Cu concentration is high, so the system tends to produce more Cu-on-Zn antisite type (Cu_{Zn} -type) defect and less Cu vacancy (V_{Cu} -type) defect. According to Han *et al.*,³⁶ the major hole carrier is V_{Cu} , so reducing the chance of V_{Cu} formation might lead to a decrease in photoresponse. The above observation would corroborate a mode in which electron-hole pairs may accumulate and recombine or the lack of a separation pathway for the photogenerated pair.^{21, 36}

4.3.3 N K-edge

The N K-edge XANES was measured in order to determine the presence and effect of the capping ligand, MPP on the different photoresponse of the two CZTS samples being

tested (**Figure 4.6**). In order to probe the ligand-nanocrystal interaction with thickness dependency, the spectra in TEY (surface sensitive) and FY (bulk sensitive) modes were measured simultaneously. All spectra display a sharp peak at 400.5 eV, which corresponds to the N 1s to π^* LUMO transition of N in a pyridinic type environment.³⁷

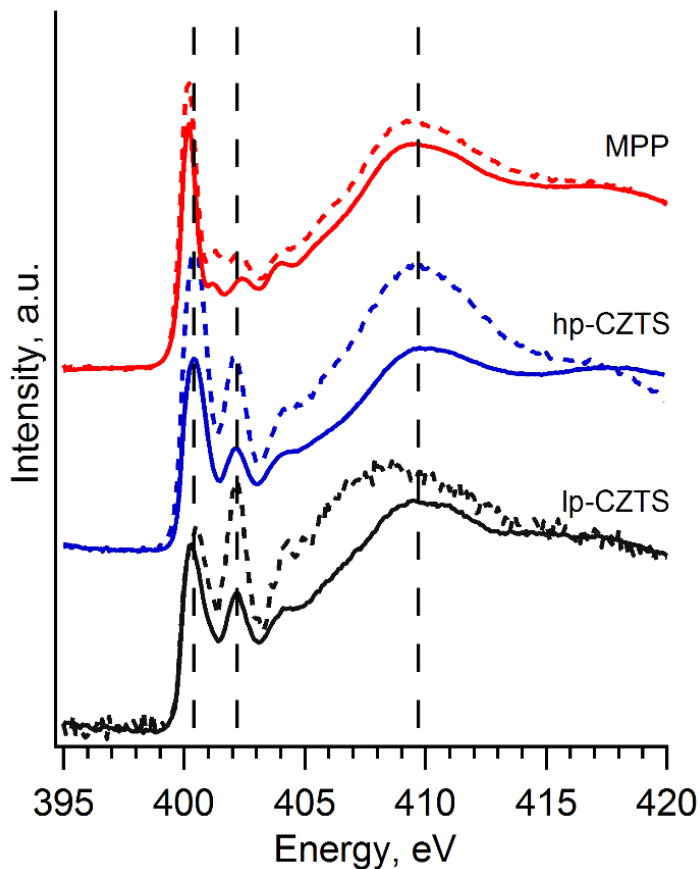


Figure 4.6 N K-edge XANES of lp-CZTS, hp-CZTS and MPP. Solid lines: TEY; dashed lines: FY. The spectra are offset vertically for clarity

The broad peak centered at 410 eV identifies the σ^* resonance associated with the N-C interatomic distance in the aromatic ring. The TEY spectra (solid lines) of lp-CZTS exhibit features that resemble the spectral profile of MPP. The first difference in MPP and MPP capped hp-CZTS can be identified as the energy shift of the π^* feature in FY:

the 400.5 eV peak shifts to higher energy in hp-CZTS. This can be explained as partial donation (coordination) of aromatic electrons from the nitrogen of MPP upon contact with the CZTS core via the interface. Although MPP is linked to the CZTS through the thiol group, electron redistribution that occurs in the pyrimidine due to the ligand-NC interaction could alter the electron density around N. The feature is seen in both TEY and FY indicating that the capping is uniform, and all MPP molecules are participating in the capping process. For lp-CZTS, however, the position of the π^* peak in TEY and FY exhibit some degree of discrepancy: the energy shift is only seen in FY. This observation suggests the MPP capping at the NC surface is less effective, and there is a layer of unbonded MPP on the NC surface. Another apparent difference is the emergence of the 402 eV peak in MPP-capped CZTS. This peak directly correlates to the change of N bonding environment upon new bond formation. The possible explanation is that the environment of the N is transformed from a pyridine-type to a graphitic type.³⁷ The pyridine component in MPP might participate in formation of dimers during the capping process.³⁸ It can also be seen that the peak intensity is higher in FY than in TEY, indicating that this feature is originated from the ligand-particle interface. In particular, the peak intensity in FY of lp-CZTS is much higher, which might be due to the close distance between the MPP molecules at the NC surface, leading to a stronger ligand-ligand interaction. In addition, the σ^* peak in FY of lp-CZTS exhibit a significant shift to low energy, but such feature is not seen in the spectra of hp-CZTS. It has been well established that the energy separation between the position of the resonance and the threshold is inversely proportional to the R^2 where R is the inter-atomic distance between the absorber and the scatterer: the closer the resonance to the threshold, the longer the

bond. Thus the energy down-shift of the σ^* indicates a longer N-C bond in lp-CZTS, which is formed by the N bond to the neighboring pyridine. The observed difference in N local environment suggests that lp-CZTS has a stronger MPP-MPP interaction than the MPP-CZTS interaction. There have been other studies on the effects of capping ligands and their effect on solar cells,³⁹⁻⁴¹ and shorter capping ligands have shown to be advantageous.⁴²⁻⁴⁴ Here the XANES demonstrate that tuning the interaction between the capping ligand and CZTS NC also plays an important role in the performance of CZTS. Uniform ligand coverage with less ligand-ligand interaction proves to be an important factor for producing large photocurrent. At the same time, a strong capping molecule interaction further reduces the surface traps for better electron-hole separation.⁴⁵⁻⁴⁶ The probing of the N K-edge of the capping ligand MPP showed that lp-CZTS had a less effective MPP capping, which has an adverse effect to the production of photocurrent by enhancing electron-hole pair stability to the point where separation of the pair was not as frequent.

4.3.4 S K-edge

The presence of secondary phases in CZTS is usually of great concern when dealing with syntheses that have no-intensive separation step. Many secondary phases that can evolve in a CZTS deal with a metal sulfides. It is often challenging to elucidate CuS, Cu₂S, SnS, ZnS or SnS₂ phases from CZTS using XRD.¹⁸ However, identification of S species using S K-edge XANES is relatively well established.⁴⁷ **Figure 4.7** shows XANES characteristics of the local structure of the CZTS from the S perspective. In comparison with other standard sulfide compounds, the S K-edge XANES of both hp- and lp-CZTS share no similarity with other binary compounds. It should be noted that the sharp peaks

above 2480 eV in CuS and Cu₂S are due to the presence of oxidized S species (i.e. sulfate). The first peak in hp- and lp-CZTS is attributed to the transition of S 1s to unoccupied 3p σ^* of a sulfide nature (bottom of the conduction band containing S character). In addition, hp- and lp-CZTS exhibit noticeable difference from the secondary phase reference spectra at 2472.8 eV, marked as the second of the dashed grid lines. Previously, Just *et al.* have reported through the use of linear combination to find the correlation between the peak ratio and the concentration of ZnS in CZTS, that a peak at that energy is caused by the presence of the secondary ZnS phase.²² The peak heights at 2472.8 eV of the samples containing ZnS secondary phase reported by Just *et al.* were much higher than that at 2470.5 eV. For the hp-and lp-CZTS produced in this study however, the opposite was true.

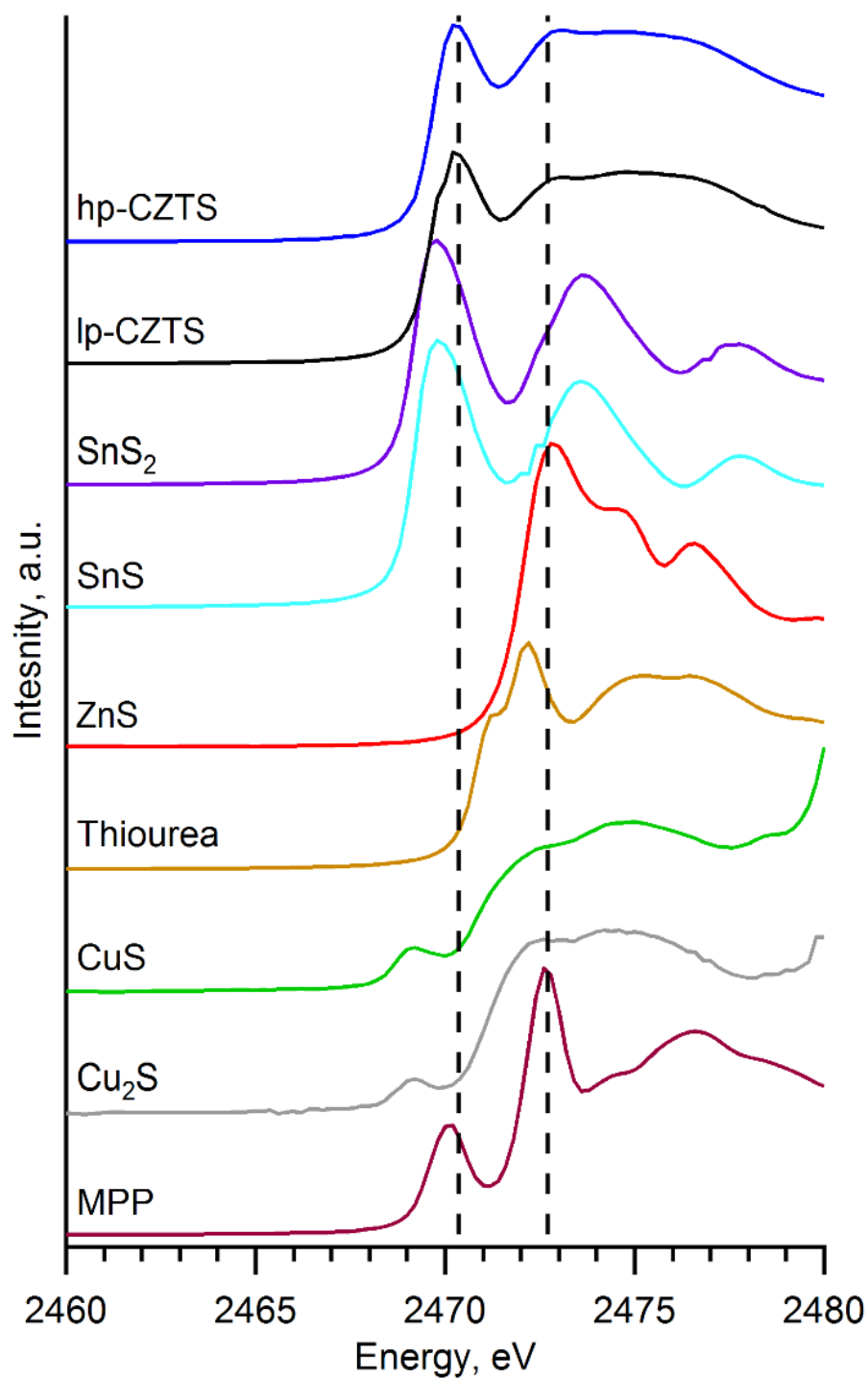


Figure 4.7 S K-edge XANES of lp-CZTS and hp-CZTS in comparison with a series of sulfide references and the capping ligand MPP. The spectra are normalized to unity edge jump and offset vertically for clarity

From the analysis of the curve fit (**Figure 4.8**), it is reasonable to see that some addition in the peak height between peak 1 of hp-CZTS and MPP. The shoulder of the lp-CZTS may still be due to interaction between lp-CZTS and unreacted MPP on the surface. However it is very hard to resolve using this method due to very close edge bands (**Table 4.1**). The second peak at ~ 2472.5 eV can show a combination of the hp- and MPP samples since the peak height and width are larger in lp-CZTS. The above observation illustrates that our one-pot NC preparation has great advantage over the PVD co-evaporation method.²² A weak shoulder in lp-CZTS could be attributed to the unreacted free MPP on the surface. Moreover, the similarities in the spectra between MPP and the CZTS samples could denote the incorporation of the capping ligand into the CZTS NCs in the lattice. Since the CZTS is copper rich, the S is likely to connect with the Cu, leading to a certain degree of hybridization. It was reported that the shape of the Cu L-edge spectra is mostly due to a particular crystal field splitting.⁴⁸ A CuS or Cu₂S crystal is very different from something that has bonds other than Cu-S. This is possibly why at the previously reported Cu L-edge, CZTS does not look like CuS or Cu₂S. But at S K-edge reported here, there are some similarities from the reflection of the hybridization between the Cu and S.

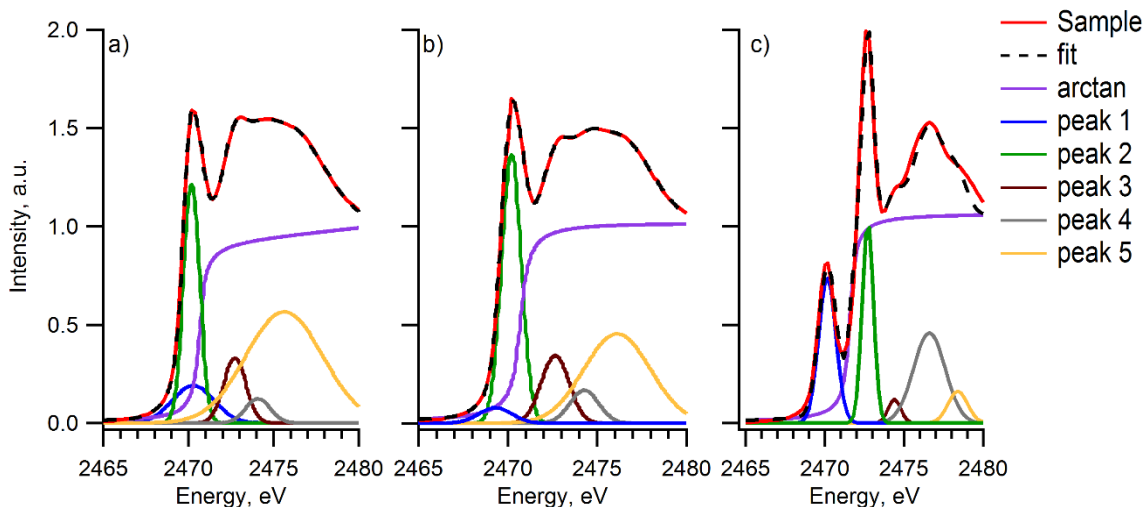


Figure 4.8 Curve fitting results of a) hp-CZTS, b) lp-CZTS and c) MPP overlaid on top of XANES data of S K-edge. The first two peaks are relevant of which the parameters are listed in Table 4.1

Table 4.1 Curve fitting analysis of peak positions, widths and areas for the first two peaks at the edge jump.

Sample	Peak Number	Peak Position	Peak width	Peak Area
		(eV)	(eV)	(a.u.)
lp-CZTS	1	2469.9	2.93	0.365
	2	2470.2	1.28	0.177
hp-CZTS	1	2470.3	2.89	0.586
	2	2470.2	1.12	0.144
MPP	1	2470.2	2.85	1.010
	2	2472.7	1.80	0.910

4.4 Conclusions

The effect of stoichiometry on photoelectrochemical and physical properties was probed using XANES and PECM analyses. The dependence of the composition was determined through the ternary contour plot. The crystals were confirmed to be secondary phase-free

by XANES. Although secondary phases are considered to be detrimental to the photoelectrochemical properties of CZTS materials, our result demonstrated that there are other factors which could cause the difference in photoperformance. Element specific XANES analysis proves that the coordination environment of Zn and the CZTS interaction with the MPP capping ligands are the two major factors. A Cu-rich environment leads to smaller crystal size, and a locally disordered Zn environment. The effects of the capping ligand MPP were elucidated by probing the N K-edge of the films. The examination of PECMs in conjunction with the analysis of XANES data allows for a critical interpretation of the compositional and atomic properties that comprise a good film for high photocurrent CZTS. The application of this knowledge may also aid in the determination of a high efficiency photovoltaic cell.

4.5 References

- (1) Walsh, A.; Chen, S.; Wei, S.; Gong, X. G.; *Adv. Energy Mater.*, **(2012)**, 2, 400-409.
- (2) Green, M. A.; Emery, K.; Hishikawa, Y.; Warta, W.; Dunlop, E. D.; *Prog. Photovoltaics Res. Appl.*, **(2013)**, 21, 1-11.
- (3) Ahn, S.; Jung, S.; Gwak, J.; Cho, A.; Shin, K.; Yoon, K.; Park, D.; Cheong, H.; Yun, J. H.; *Appl. Phys. Lett.*, **(2010)**, 97, 021905 1-3.
- (4) Todorov, T. K.; Reuter, K. B.; Mitzi, D. B.; *Adv. Mater.*, **(2010)**, 22, E156-E159.
- (5) Washio, T.; Shinji, T.; Tajima, S.; Fukano, T.; Motohiro, T.; Jimbo, K.; Katagiri, H.; *J. Mater. Chem.*, **(2012)**, 22, 4021-4024.
- (6) Redinger, A.; Berg, D. M.; Dale, P. J.; Siebentritt, S.; *J. Am. Chem. Soc.*, **(2011)**, 133, 3320-3323.

- (7) Hsu, W.-C.; Zhou, H.; Luo, S.; Song, T.-B.; Hsieh, Y.-T.; Duan, H.-S.; Ye, S.; Yang, W.; Hsu, C.-J.; Jiang, C.; Bob, B.; Yang, Y.; *ACS Nano*, (2014), 8, 9164-9172.
- (8) Vaccarello, D.; Tapley, A.; Ding, Z.; *RSC Adv.*, (2013), 3, 3512-3515.
- (9) Steinhagen, C.; Panthani, M. G.; Akhavan, V.; Goodfellow, B.; Koo, B.; Korgel, B. A.; *J. Am. Chem. Soc.*, (2009), 131, 12554-12555.
- (10) Shavel, A.; Cadavid, D.; Ibanez, M.; Carrete, A.; Cabot, A.; *J. Am. Chem. Soc.*, (2012), 134, 1438-1441.
- (11) Chung, C.-H.; Bob, B.; Lei, B.; Li, S.-H.; Hou, W. W.; Yang, Y.; *Sol. Energ. Mat. Sol. Cells*, (2013), 113, 148-152.
- (12) Yang, W.; Duan, H.-S.; Bob, B.; Zhou, H.; Lei, B.; Chung, C. H.; Li, S. H.; Hou, W. W.; Yang, Y.; *Adv. Mater.*, (2012), 24, 6323-6329.
- (13) Zhou, H.; Song, T. B.; Hsu, W. C.; Luo, S.; Ye, S.; Duan, H. S.; Hsu, C. J.; Yang, W.; Yang, Y.; *J. Am. Chem. Soc.*, (2013), 135, 15998-16001.
- (14) Zhou, H. P.; Duan, H. S.; Yang, W. B.; Chen, Q.; Hsu, C. J.; Hsu, W. C.; Chen, C. C.; Yang, Y.; *Energy Environ. Sci.*, (2014), 7, 998-1005.
- (15) Suehiro, S.; Horita, K.; Kumamoto, K.; Yuasa, M.; Tanaka, T.; Fujita, K.; Shimano, K.; Kida, T.; *J. Phys. Chem. C*, (2014), 118, 804-810.
- (16) Zillner, E.; Paul, A.; Jutimoosik, J.; Chandarak, S.; Monnor, T.; Rujirawat, S.; Yimnirun, R.; Lin, X. Z.; Ennaoui, A.; Dittrich, T.; Lux-Steiner, M.; *Appl. Phys. Lett.*, (2013), 102, 221908-1-221908-4.
- (17) Fontané, X.; Calvo-Barrio, L.; Izquierdo-Roca, V.; Saucedo, E.; Pérez-Rodríguez, A.; Morante, J. R.; Berg, D. M.; Dale, P. J.; Siebentritt, S.; *Appl. Phys. Lett.*, (2011), 98, 181905-1-181905-4.
- (18) Scragg, J. J.; Dale, P. J.; Peter, L. M.; *Thin Solid Films*, (2009), 517, 2481-2484.

- (19) Khoshmashrab, S.; Turnbull, M. J.; Vaccarello, D.; Nie, Y.; Martin, S.; Love, D. A.; Lau, P. K.; Sun, X.; Ding, Z.; *Electrochim. Acta*, (2015), 162, 176-184.
- (20) Kumar, P.; Gusain, M.; Nagarajan, R.; *Inorg. Chem.*, (2011), 50, 3065-3070.
- (21) Chen, S.; Gong, X. G.; Walsh, A.; Wei, S.; *Appl. Phys. Lett.*, (2010), 96, 021902 1-4.
- (22) Just, J.; Lützenkirchen-Hecht, D.; Frahm, R.; Schorr, S.; Unold, T.; *Appl. Phys. Lett.*, (2011), 99, 262105 1-3.
- (23) Olekseyuk, I. D.; Dudchak, I. V.; Piskach, L. V.; *J. Alloy. Compd.*, (2004), 368, 135-143.
- (24) Ye, H.; Akhavan, V. A.; Goodfellow, B. W.; Panthani, M. G.; Korgel, B. A.; Bard, A. J.; *J. Phys. Chem. C*, (2011), 115, 234-240.
- (25) Vaccarello, D.; Liu, L.; Zhou, J.; Sham, T.-K.; Ding, Z.; *J. Phys. Chem. C*, (2015), 119, 11922-11928.
- (26) Regier, T.; Krochak, J.; Sham, T. K.; Hu, Y. F.; Thompson, J.; Blyth, R. I. R.; *Nucl. Instrum. Meth. A*, (2007), 582, 93-95.
- (27) Hu, Y. F.; Coulthard, I.; Chevrier, D.; Wright, G.; Igarashi, R.; Sitnikov, A.; Yates, B. W.; Hallin, E. L.; Sham, T. K.; Reininger, R. In *Preliminary Commissioning and Performance of the Soft X-ray Micro-Characterization Beamline at the Canadian Light Source*, AIP Conf., 2010; pp 343-348.
- (28) Katagiri, H.; Jimbo, K.; Maw, W. S.; Oishi, K.; Yamazaki, M.; Araki, H.; Takeuchi, A.; *Thin Solid Films*, (2009), 517, 2455-2460.
- (29) Schorr, S.; Mainz, R.; Mönig, H.; Lauermann, I.; Bär, M.; *Prog. Photovoltaics Res. Appl.*, (2012), 20, 557-567.
- (30) Hsu, W.-C.; Repins, I.; Beall, C.; DeHart, C.; Teeter, G.; To, B.; Yang, Y.; Noufi, R.; *Sol. Energ. Mat. Sol. Cells*, (2013), 113, 160-164.

i. This chapter contains the work presented in Vaccarello, D. *et al. J. Phys. Chem. C* 2015, 119 (21), 11922-8

- (31) Scragg, J. J., University of Bath, 2011.
- (32) Huang, W.-C.; Tseng, C.-H.; Chang, S.-H.; Tuan, H.-Y.; Chiang, C.-C.; Lyu, L.-M.; Huang, M. H.; *Langmuir*, (2012), 28, 8496-8501.
- (33) Wang, Z.; Wang, J.; Sham, T.-K.; Yang, S.; *J. Phys. Chem. C*, (2012), 116, 10375-10381.
- (34) Murphy, M. W.; Zhou, X. T.; Ko, J. Y. P.; Zhou, J. G.; Heigl, F.; Sham, T. K.; *J. Chem. Phys.*, (2009), 130, 084707 1-8.
- (35) Chiou, J. W.; Kumar, K. P. K.; Jan, J. C.; Tsai, H. M.; Bao, C. W.; Pong, W. F.; Chien, F. Z.; Tsai, M.-H.; Hong, I.-H.; Klauser, R.; Lee, J. F.; Wu, J. J.; Liu, S. C.; *Appl. Phys. Lett.*, (2004), 85, 3220-3222.
- (36) Han, D.; Sun, Y.; Bang, J.; Zhang, Y.; Sun, H.-B.; Li, X.-B.; Zhang, S.; *Phys. Rev. B*, (2013), 87, 155206 1-7.
- (37) Zhang, L.-S.; Liang, X.-Q.; Song, W.-G.; Wu, Z.-Y.; *Phys. Chem. Chem. Phys.*, (2010), 12, 12055-12059.
- (38) Hohenstein, E. G.; Sherrill, C. D.; *J. Phys. Chem. A*, (2009), 113, 878-886.
- (39) Aldakov, D.; Chandezon, F.; De Bettignies, R.; Firon, M.; Reiss, P.; Pron, A.; *Eur. Phys. J-Appl. Phys.*, (2007), 36, 261-265.
- (40) Olson, J. D.; Gray, G. P.; Carter, S. A.; *Sol. Energ. Mat. Sol. Cells*, (2009), 93, 519-523.
- (41) Chen, J.; Song, J. L.; Sun, X. W.; Deng, W. Q.; Jiang, C. Y.; Lei, W.; Huang, J. H.; Liu, R. S.; *Appl. Phys. Lett.*, (2009), 94, 153115 1-4.
- (42) Talapin, D. V.; Murray, C. B.; *Science*, (2005), 310, 86-89.
- (43) Hillhouse, H. W.; Beard, M. C.; *Curr. Opin. Colloid In.*, (2009), 14, 245-259.

- (44) Semonin, O. E.; Luther, J. M.; Choi, S.; Chen, H. Y.; Gao, J.; Nozik, A. J.; Beard, M. C.; *Science*, (2011), 334, 1530-1533.
- (45) Branz, H. M.; Schiff, E. A.; *Phys. Rev. B*, (1993), 48, 8667–8671
- (46) van de Krol, R. *Principles of Photoelectrochemical Cells*; Springer, 2012; p 13-67.
- (47) Fleet, M. E.; *Can. Mineral.*, (2005), 43, 1811-1838.
- (48) Lamberti, C.; Bordiga, S.; Bonino, F.; Prestipino, C.; Berlier, G.; Capello, L.; D'Acapito, F.; Xamena, F. X. L. i.; Zecchina, A.; *Phys. Chem. Chem. Phys.*, (2003), 5, 4502-4509.

5 Probing the CZTS/CdS Heterojunction Utilizing Photoelectrochemistry and X-ray Absorption Spectroscopy

The importance of renewable resources is becoming more influential on research due to the depletion of fossil fuels. Cost-effective ways of harvesting solar energy should also be at the forefront of these investigations. $\text{Cu}_2\text{ZnSnS}_4$ (CZTS) solar cells are well within the frame of these goals and a thorough understanding of how they are made and processed synthetically is crucial. The CZTS/CdS heterojunction was examined using photoelectrochemistry and synchrotron radiation (SR) spectroscopy. These tools provided physical insights into this interface that was formed by electrophoretic deposition of CZTS nanocrystals and chemical bath deposition (CBD) of CdS for the two respective films. It was discovered that CBD induced a change in the local and long range environment of the Zn in the CZTS lattice, which was detrimental to the photoresponse. X-ray absorption near-edge structures (XANES) and extended X-ray absorption fine structures (EXAFS) of the junction showed that this change was at an atomic level and was associated with the coordination of oxygen to zinc, which was confirmed through FEFF fitting. It was found that this change in both photoresponse and in the Zn coordination can be reversed with the use of low temperature annealing. Investigating CZTS through SR techniques provides detailed structural information of minor changes from the zinc perspective.

5.1 Introduction

The desire for solar cells with earth-abundant chemical elements has been the driving force in solar energy research in recent years. While possessing the current highest

laboratory photoconversion efficiencies, $\text{CuIn}_x\text{Ga}_{(1-x)}\text{Se}_2$ and CdTe-based solar cells contain layers which rely on uncommon, expensive, and sometimes toxic elements.¹⁻³ On the contrary, $\text{Cu}_2\text{ZnSnS}_4$ (CZTS) based solar cells offer a reasonable alternative due to the low cost and high abundance of Cu, Zn, Sn, and S. CZTS is a p-type semiconductor with a tunable direct energy band gap between 1.4-1.5 eV and a high absorption coefficient, more than 10^4 cm^{-1} .⁴⁻⁵ At present, the laboratory efficiency of CZTS has reached as high as 12.6%.⁶ This is not only lower than those of CIGS and CdTe-based solar cells,^{2, 7} but also much lower than its theoretical value $\sim 30\%$.⁸⁻⁹ Therefore, a step-wise approach to understand the synthesis, preparation and interactions of CZTS solar cells is necessary in order to unlock its full potential.

There are a variety of techniques for synthesis and deposition of CZTS films, including sputtering,^{4, 10} thermal co-evaporation,¹¹⁻¹² pulsed laser deposition,¹³ electroplating,¹⁴ solution process,¹⁵⁻¹⁷ and solvothermal methods¹⁸⁻¹⁹. A convenient and facile solvothermal method has been developed in our group for CZTS and CuInS_2 (CIS) nanocrystals that utilizes low temperatures as well as low-cost reagents.²⁰⁻²¹ The CZTS nanocrystals produced by this synthesis have been characterized and optimized for maximized photoresponse, effects of stoichiometry,²²⁻²³ and phase purity through examining local structures.²⁴ Several deposition routes have also been explored.²⁵ From these results an effective CZTS layer has been developed at a relatively low environmental impact with scalability in mind.

The next step is to identify the effectiveness of the CZTS/CdS hetero-junction in our layer by layer strategy. The interaction between CZTS and CdS is important since the buffer layer's sole purpose is to facilitate photogenerated electron transfer out from the

absorber layer into an n-type semiconductor.²⁶⁻²⁸ Methodologically, chemical bath deposition (CBD) for CdS films has been reported utilizing a time-controlled chemical reaction for depositing a thin layer through precipitation.²⁹ CBD typically involves the use of aqueous conditions in order to heterogeneously nucleate CdS on substrates.³⁰ One nucleation pathway involves the deposition of Cd(OH)₂ onto the substrate to provide a catalytic surface on which thiourea can decompose.³¹ This coupling with aqueous environment can allow for oxidation or coordination of –OH and –OH₂ to the surface of exposed CZTS. A positive effect on the photocurrent generation through photoelectrochemical measurements (PECMs) by the addition of CdS films has been seen in electrodeposited CIGS, CIS and CZTS films;³²⁻³⁴ however, in the case of nanocrystals prepared and deposited onto a substrate might be significantly different.

Synchrotron radiation (SR) with energy tunable X-rays is a powerful tool in examining the local environments at atomic levels via absorption spectroscopy, which can be utilized for a vast number of applications in many research fields.^{20, 35-37} SR has many options for a wide range of transition metal elements as well.³⁸⁻⁴⁰ For solar energy materials, while SR is typically reserved for the detection of secondary phases and disordered atoms,^{37, 41-44} the use of X-ray absorption near-edge structures (XANES) and extended X-ray absorption fine structures (EXAFS) can probe the local and extended environments of a target atom, respectively. Previously, XANES was used to correlate the differences in electronic structures to local compositions in CZTS and CIS light absorbing layers with varied photocurrents, giving new details into the physical aspect of photoelectrochemistry.^{24, 45} Through probing the CZTS thin films with the addition of new layers, an examination of the effects by these new layers has been realized in this

work. Alternations in the local and extended structures can be used to determine the cause for changes in photoelectrochemical performance as a function of spectral change at an atomic site of interest.

Employing a cooperative use of both SR spectroscopies and electrochemistry, a CZTS-based solar cell should be dynamically characterized at each interface. The targeted CZTS/CdS heterojunction is an interface of particular importance as it is the interaction of this layer that facilitates electron transfer, resulting in high efficiency devices.^{32, 46-47} The balance between high efficiency and low associated cost is often precarious with respect to processing of solar devices. The necessity of high-energy steps might negate the purpose of utilizing CZTS as a light absorbing layer in order to reduce costs. The addition of a layer can change the local environment of the CZTS, leading to enhancement or degradation of the effectiveness of the absorbing layer. These physicochemical aspects are important to uncover. Our strategy of a step-wise optimization for a photovoltaic device is the balance of effectiveness and cost, particularly for the objective of implementation into mass production.

5.2 Experimental

5.2.1 CZTS Film Preparation

CZTS NCs were prepared via a one-pot solvothermal method previously described by our group.²⁰ In brief, Cu(acac)₂ (Sigma-Aldrich, ≥99.9%), ZnCl₂ (Sigma-Aldrich, ≥98%), SnCl₂ (Sigma-Aldrich, 98%) were added to benzyl alcohol (BA, Alfa Aesar, ≥99%) in molar ratios of 1.44:4.02:1.00. The precursors were heated at 180°C for two minutes to allow for the salts to be fully dissolved. Thiourea (Sigma-Aldrich, ≥99%) and 2-

mercapto-5-n-propylpyrimidine (MPP, Alfa Aesar, 98%) were added as the sulfur source and capping ligand respectively at 7.5 mg/mL of BA. The reaction completed after 10 minutes. The resultant NCs were centrifuged and subsequently cleaned with the use of isopropanol (Sigma-Aldrich, $\geq 99.7\%$) before being dispersed into isopropanol at 2 g/L.

CZTS films were cast using electrophoretic deposition (EPD) with parameters previously optimized by our group.²⁵ Briefly, a standard glass beaker ($\emptyset = 4$ cm) contained a dispersion of NCs in isopropanol. A Teflon cover held FTO coated glass slides (Sigma Aldrich with sheet resistance of $13 \Omega/\text{square}$) 1 cm apart and acted as the anodic working and cathodic counter electrode when attached to a power source. The films were deposited using a constant current of $0.24 \text{ mA}/\text{cm}^2$ for 40 seconds on a Keithley 2400 source meter (Tektrnix, Beaverton, OR). This time and current corresponded to $\sim 1 \mu\text{m}$ of CZTS addition onto the FTO anode.

5.2.2 Chemical Bath Deposition of CdS Films

CdS was deposited on the CZTS film via CBD. The bath employed was based on a previous method,³² with a 1.5 mM CdSO_4 (Fischer Scientific, 98%), 1.5 M NH_4OH (Caledon, $\geq 99\%$) and 7.5 mM thiourea (Sigma-Aldrich, $\geq 99\%$) in water. The CdSO_4 and NH_4OH were stirred for approximately 30 minutes at room temperature, then heated up to 65°C and allowed to keep the same temperature for 5 minutes before adding thiourea. The addition of thiourea was followed by lowering the CZTS thin film substrate into the solution where the reaction proceeded for 23 minutes. This deposition time accounted for approximately 50 nm of CdS on the top of the CZTS films.

5.2.3 Post-Process Annealing

Annealing was performed using a Thermoscientific Lindberg Blue M Tube Furnace (Asheville, NC) with a specially designed quartz tube under an inert argon atmosphere (**Figure 5.1**). The tube was purged three times to ensure removal of oxygen by successively evacuating with a vacuum pump to below -200 kPa and refilling with Ar at 70 kPa. The setpoint temperatures were between 200 and 550 °C and were achieved through a ramp-up speed of 25 °C/min. At the set temperature and with the Ar pressure under 70 kPa, the annealing was processed for 50 minutes. After the annealing time was over, the furnace was opened and the tube was raised above the heating bed to cool to room temperature at a natural rate. After the tube achieved room temperature, a final vacuum-purge cycle was performed before opening the tube.

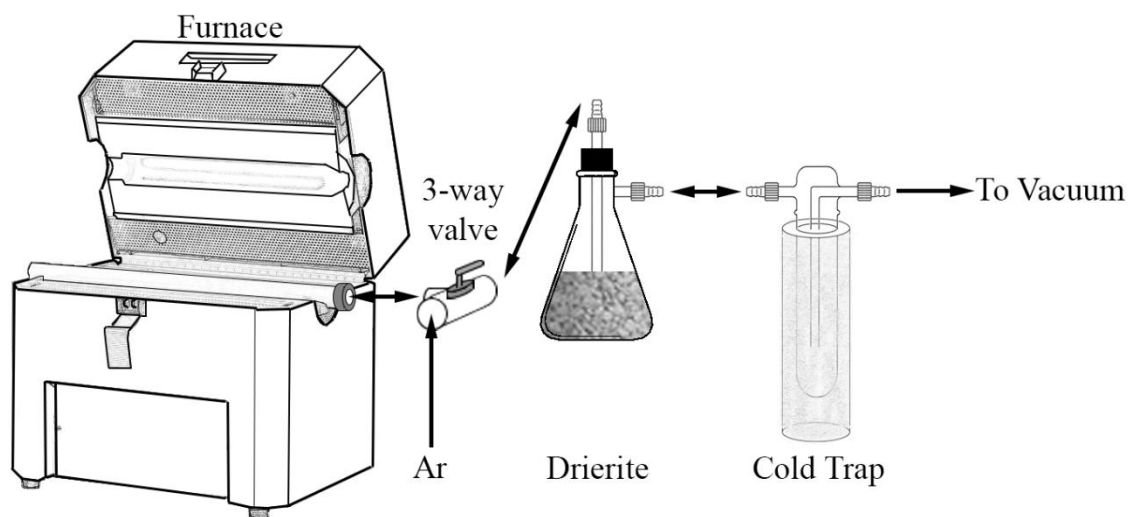


Figure 5.1 Schematic representation of furnace set-up for post processing. A three-way valve connects the quartz tube to an Ar inlet and a Drierite filled vacuum flask. The outlet is connected to a liquid nitrogen-filled cold trap before entering a vacuum

5.2.4 Photoelectrochemical Measurements

Film quality was determined through the comparison of PECMs as reported by Ye et al. and our group.^{20, 32} Briefly, the films were immersed into a solution containing a 0.05 M methyl viologen dichloride ($MVCl_2$, Sigma-Aldrich, 98%) and 0.1 M KCl (99%, Sigma Aldrich). A coiled platinum wire ($d = 0.5\text{cm}$) and a saturated calomel electrode (SCE) were used as the counter and reference electrode, respectively. The light source was a 150 W Newport lamp with an AM 1.5 D filter. An electronic shutter that operated at 0.333 Hz modulated the light. A linear potential sweep was applied from 0.000 to -0.400 V at a scan rate of 0.005 Vs^{-1} using a CHI 832a electrochemical analyzer (CH Instruments, Austin TX).

5.2.5 XANES and EXAFS Analysis

XANES were performed at the Canadian Light Source (CLS) located in Saskatoon, SK. Experiments were carried out on the undulator-based high resolution spherical grating monochromator (SGM, 11ID-1) beamline. SGM provides soft X-ray energy from 250 eV to 2000 eV with a resolution $E/\Delta E > 5000$. This energy range is optimal for the Cu and Zn L-edges. The samples were dispersed on a double-sided carbon tape that was mounted 45° toward the incident X-ray beam. Due to the short escape depth of low kinetic energy electrons, a surface-sensitive total electron yield (TEY) scan was used to measure specimen current resulted from photoelectrons, Auger electrons and secondary electrons. A fluorescent yield (FY) scan collected spectra from a silicon drift detector with $<100\text{ eV}$ energy resolution at the N K-edge (AMPTEK Inc., Bedford, MA) allowing for bulk sensitive detection. All absorption spectra were normalized to incident photon

flux (I_0). The spectrum background was removed and normalized to a flat region of the post edge to unity.^{23, 45}

EXAFS measurements of Cu and Zn K-edges were performed at the PNC/XSD 20-BM beamline of the Advanced Photon Source (APS) at Argonne National Laboratory in Argonne, IL. CZTS films were capped by Kapton tape. A Si (111) monochromator and a 400 μm vertical slit was used over 8.78 to 9.52 keV for the Cu K-edge and 9.46 to 10.4 keV for the Zn K-edge and even k-spacing scans. The samples were placed at a 45° angle with respect to the incident photons and perpendicular to the 13-element Canberra detector that recorded the FY. Detector saturation was set at 50,000 counts per second and all scans were duplicated to sum two million total counts for each element. All spectra were normalized to the incident photon flux, I_0 . Energy calibration was performed using a reference Cu and Zn (EXAFS Materials Inc.) with 7.5 and 10 μm thickness, respectively. They were placed downstream of the sample in two ion chambers filled with 80:20 N_2/Ar mixture. All spectra were collected at room temperature.

The data was treated with a software package of Athena and Artemis. Fluorescence yield was plotted over a corrected energy range defined as $\mu(E)$. The threshold energy, E_0 , for Cu and Zn were set to 8979 eV and 9659 eV for the K-edge, and 932.7 eV and 1021.8 eV for the L-edges, respectively. The normalized energy spectra were examined by normalizing the pre-edge to zero and the post-edge to unity.⁴⁸ The EXAFS data was converted into the photoelectron vector k space, converting from an energy construct into a physical one.⁴⁹⁻⁵⁰ Attenuation of the EXAFS at high k values was compensated through a cubic k -weighting.⁴⁹⁻⁵¹ A Fourier transform was applied using a Hanning window over

a k-range of 3 to 11 Å⁻¹. This produced a measure of relative radial distances, or the R-space plot. The transform from k-space within the window region is generated using a complex Fourier transform and displaying the phase un-corrected R-space radial distribution of the absorbing backscattering atomic pair of interest. A Fourier back transform was applied to the R-space giving the back transformed k-space, to simplify the analysis of CZTS with possible defects. Using the Artemis software package, EXAFS spectra were generated for pure kesterite CZTS from the crystallographic information file (cif) generated using VESTA and crystallographic information (JCPDS 26-0575) at room temperature.⁵² These simulations were used to overlap the peaks and thus quantify the bond distances in our experimental EXAFS. Additional peaks outside of the CZTS oscillations were accounted for by means of component addition to the cif. The CZTS oscillations were calibrated on these samples based on the oscillations obtained from the samples without CdS. By back-calculation, the bond length of this component was determined against known bond lengths and possible contaminants from the chemical procedure. This was carried out using the maximum range associated with the simulated parameters. The complete theoretical spectrum was further compared across the samples to determine the relative closeness of our samples to the theoretically pure kesterite structure.

5.3 Results and Discussion

5.3.1 PECMs

The addition of the CdS buffer layer is commonly utilized as a multi-purpose layer: the facilitation of the electron transfer from CZTS into an n-type semiconductor layer, the chemical buffer layer to protect CZTS from subsequent processing steps and its lattice-

matching properties.^{26, 53} **Figure 5.2** illustrates the PECM response of CZTS (black) and CZTS/CdS (red) films with chopped illumination while applying a linear sweep in potential. The photoresponse of the CZTS interacting with a methyl viologen ion (MV^{2+}) can be described by **Equations 5.1-5.**^{45, 54}



Equation 5.1 describes the generation of an electron-hole pair in the CZTS upon illumination of light. **Equation 5.2** is the decay of the electron-hole pair if they are not able to sufficiently separate. **Equation 5.3** defines the electron transfer that occurs at the CZTS/ MV^{2+} or CZTS/CdS/ MV^{2+} interface, this is denoted in **Figure 5.2** as the sharp increase in current that occurs upon illumination. The electron transfer can reduce the MV^{2+} causing a separation of the products (**Equation 5.4**) or can recombine with a hole from the CZTS or CZTS/CdS and subtract from the photocurrent (**Equation 5.5**). Recombination as a loss in photocurrent can be seen in **Figure 5.2** as the sloped decrease after the initial photoresponse. Increased recombination compared to product separation can also be seen as a negative overshoot when the light turns off. In **Figure 5.2**, the CZTS PECMs show the negative overshoot after illumination is removed. Interestingly, this is in contrast to what obtained by Ye et al after the addition of a buffer layer.³²

Energetically, the CZTS/CdS heterojunction interface has been described similar to a cliff-like configuration.⁵⁵⁻⁵⁶ As a result, carrier loss is attributed to this heterojunction, which could lead to a loss in photocurrent and a sharper decrease in photoresponse due to electron-hole recombination.²⁶ This type of loss can be seen with the addition of the CdS layer with a decrease in photocurrent at less negative potentials. Additionally at more negative potentials, the photocurrent decreases drastically after the initial photon flux compared to the CZTS samples. This can be attributed to high recombination in the material, **Equation 5.5**.^{22, 45} The presence of a current overshoot after the light turns off also confirms the presence of a material with higher recombination in the CZTS/CdS films over the CZTS.^{45, 54}

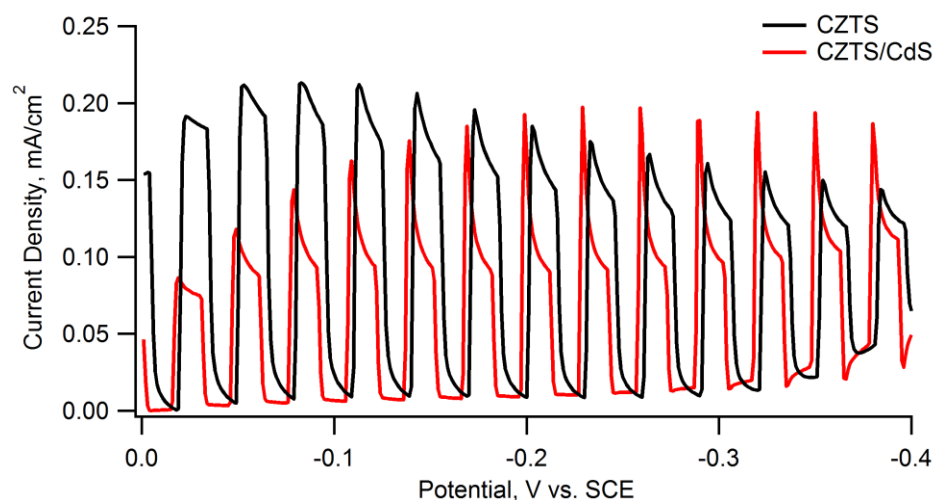


Figure 5.2 PECMs of a CZTS thin film on FTO (black) and CZTS/CdS heterojunction (red). Cathodic reduction of MV^{2+} with higher negative potential reduces with CdS addition and recombination after the photoexcitation can be seen through the sharp decrease in photoresponse

5.3.2 EXAFS Analysis

By means of synchrotron radiation on the Cu and Zn atoms, subtle changes in the CZTS can be revealed by analyzing the local and extended environments of these atoms as a result of subsequent layer deposition.

Figure 5.3 shows EXAFS data for the Zn K-edge of CZTS and CZTS/CdS samples. The XANES region (**Figure 5.3a**) shows different local environments for the Zn after the addition of CdS. The initial absorption edge of the CZTS film was found to be 9659 eV, while the CZTS/CdS sample revealed the same edge energy with a second absorption peak at 9669 eV. Similarly, the EXAFS region (**Figure 5.3a inset**) shows that extended region is also different, the variation in the higher energy oscillations indicate different interactions of the Zn atom beyond the closest atoms.^{37, 57} The corresponding k- and R-spaces as well as the k- space that was obtained from Fourier back transform also show drastically different Zn environments. The k-space is a summation of the signals of different constituent frequencies acting on the atom.^{51, 58} Long range breakdown of the periodicity indicates the long-term order is not maintained within the atom of interest. In the case of the Zn (**Figure 5.3b**), the periodicity is maintained well in the CZTS samples but decomposes in the CZTS/CdS. This lends weight to the changed state of the Zn with the addition of the CdS buffer layer. The radial distance of 2.08 Å to the next nearest neighbor seen in the R-space (**Figure 5.3c**) is also drastically shorter than the traditional Zn-S bond found in CZTS, 2.334 Å.⁵⁹⁻⁶⁰ The k-space is obtained through a Fourier back transform of the R-space data.⁵¹ In **Figure 5.3d** the long range oscillations are not congruent, and would continue to corroborate the findings of a different Zn system.

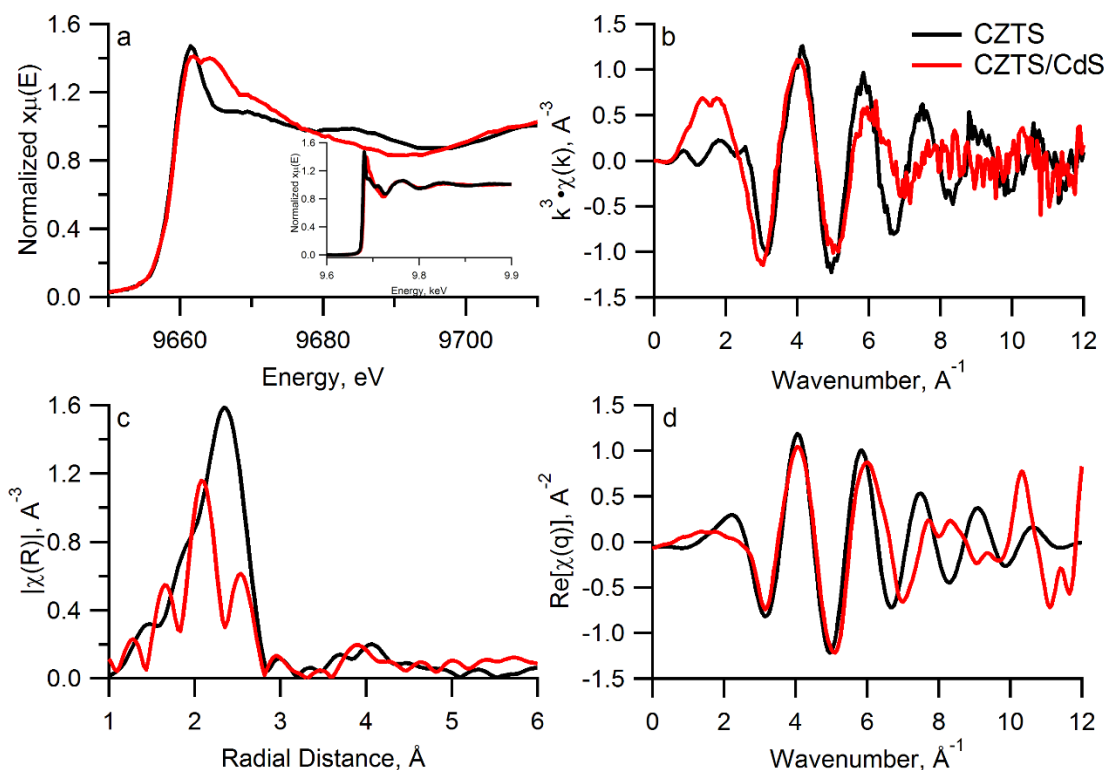


Figure 5.3 Zn K-edge data for CZTS (black) and CZTS/CdS (red) thin films a) near-edge normalized absorption profiles with extended absorption fine structures (inset). b) Absorption energies converted into k^3 -space c) R space profiles of the thin films obtained after Fourier transforming using a Hanning window over k -range of 3 to 11, d) and back transformed k -space

5.3.3 EXAFS Modelling

The CZTS/CdS interface is created through the use of CBD. This process is typically done in aqueous solutions. Typically the addition of CdS deposited through CBD does not have a structural change on the substrate.⁴⁶ However, this is the only process in our method that involves a change from organic solutions and a coordination or electronic change can be seen in the PECMs. With this in mind, there are methods of modeling EXAFS results that are tailored to CZTS systems at low temperatures.⁶¹ FEFF calculations were performed on pure kesterite CZTS calculated from the cif file.⁵² At

room temperature the attenuation of the X-ray scattering, known as the Debye-Waller factor, dampens long range structure due to additional interactions caused by thermal vibrations.^{49-50, 62} By introducing fluidity to the model, the degree of deviation from pure kesterite was calculated as a result of fitting the model to our experimental data. The model however, did not agree with the CZTS/CdS samples (**Figure 5.4**).

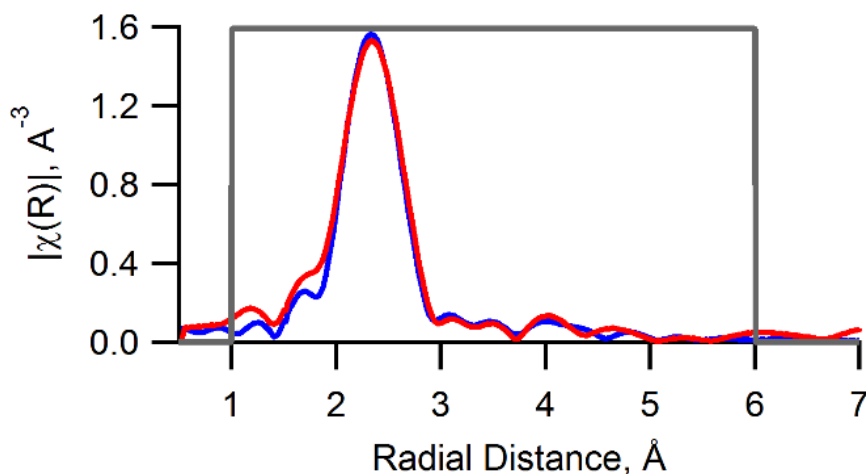


Figure 5.4 Athena fitting for Zn K-edges of CZTS thin films (red). Fitting was performed with a theoretically pure kesterite crystal (blue) over the windowed area (gray)

For this reason, another scattering pathway was integrated on top of the kesterite model to improve the fitting agreement. The radial distance of the scattering pathway was tuned over a range of between 1.8 and 2.4 Å. The CZTS/CdS films corresponded to the altered profile of the CZTS for the Zn K-edge (**Figure 5.5**). In the back transformed k-space (**Figure 5.5a**) the long term oscillations within the Hanning window match well with the model and its fit. The R-space (**Figure 5.5b**) shows that the fitting corresponded well with the measurements in radial distance. The radial distance at the point of maximum

congruence with the model occurred at 2.08 Å. This lowered radial distance of the Zn with another scattering pathway parallels typical findings for Zn-O and Zn-OH₂ lengths 1.95-2.08 Å respectively.⁶³⁻⁶⁵

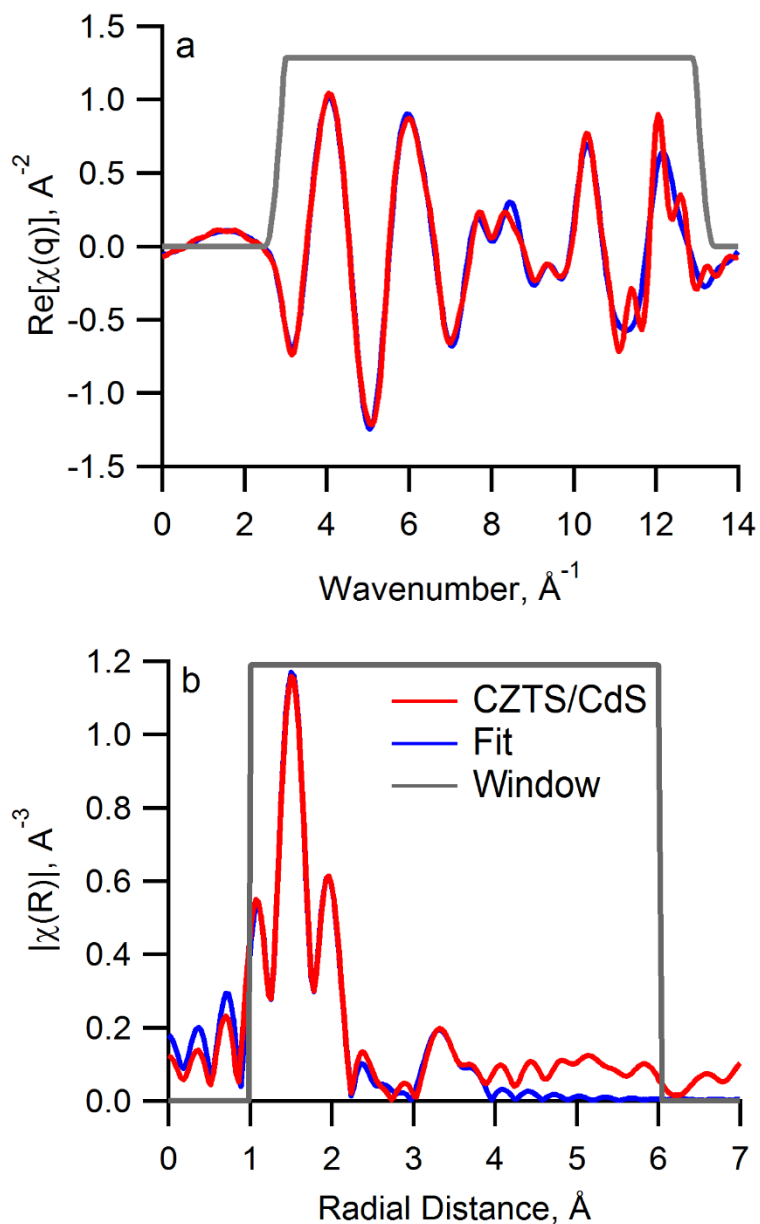


Figure 5.5 Athena fitting for Zn K-edges of CZTS/CdS thin films (red). Fitting was performed with a theoretically pure kesterite crystal in addition to an -OH₂ coordination (blue) over the windowed period (gray). The graphs correspond to the

a) back transformed k-space and b) R-space of the extended fine structures, respectively

The growth mechanisms of CdS through a CBD method can vary but can be highlighted in **Figure 5.6.**^{31, 66-68} The base layer of CdS is typically formed through the removal of –OH and –OH₂ groups through decomposition of a metastable complex (**Figure 5.6: 1-3**).⁶⁶ The process usually involves deposition onto a uniform surface with minimal chances for a dihydroxothiurea-cadmium complex to not undergo a Rideal-Eley mechanistic change. The EPD of CZTS was done with the use of NCs, the adsorption of these NCs, while relatively monodisperse, would still not have a flat microscopic surface on which the CdS can form.²⁰ As a result, the CZTS may become oxidized or coordinate with –OH₂ groups (**Figure 5.6: 4-6**).

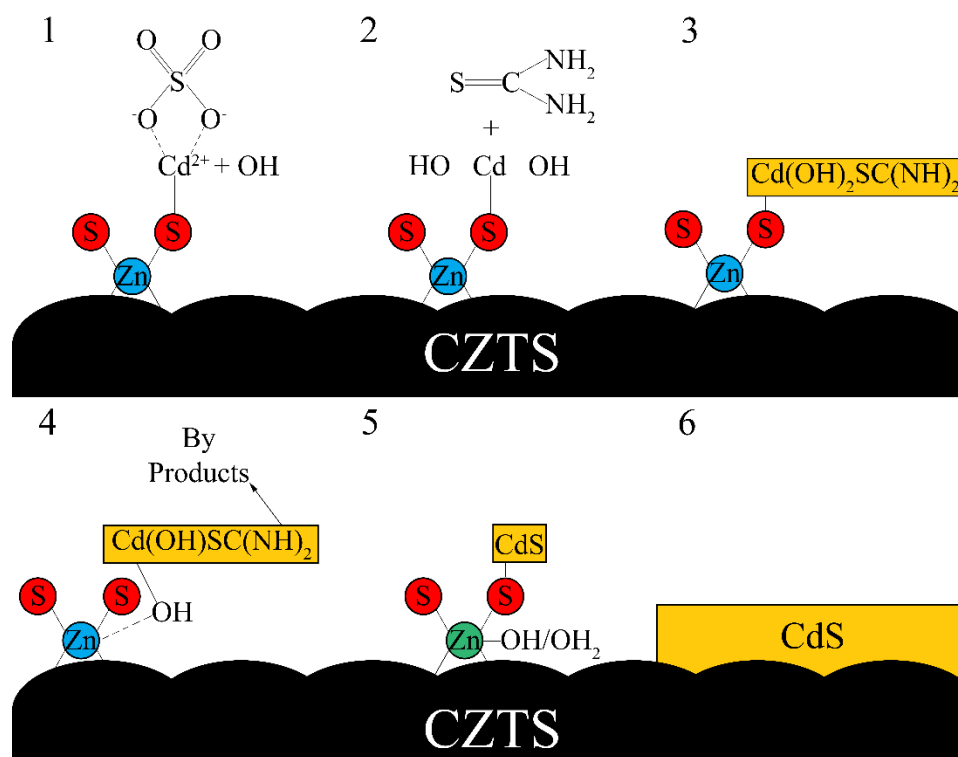


Figure 5.6 Schematic diagram of CBD-CdS Growth mechanism and possible Zn-OH/OH₂ coordination. 1) adsorption of CdSO₄ to CZTS in solution 2) -OH substitution 3) formation of metastable dihydroxothiurea-cadmium complex 4) -OH/OH₂ co-ordination of Zn 5) formation of CdS 6) CdS deposition on top of the CZTS film

5.3.4 Post-Process Annealing and L-edge EXAFS

With the decrease in photocurrent and change in the local and extended environments of the CZTS when a CZTS/CdS heterojunction forms indicates the necessity for a post-processing step. CIS NC films have already shown to exhibit enhanced photocurrent as a result of mild post-processing techniques, and were applied to the CIS films before and after the addition of the CdS.³³ This was carried out in order to confirm that the addition of the CdS was responsible for the deviation in the Zn scattering and not just increased crystallinity in the CZTS due to heating. **Figure 5.7a** illustrates the changes that

occurred in the PECMs of CZTS with the addition of CdS and subsequent annealing. The magnitude and shape of the photocurrent returns after the annealing step (CZTS/CdS_a) and recombination within the film is not as prevalent. Even though a temperature range between 200 and 550 °C was tested, 250 °C was chosen because it was the lowest temperature at which the return of photocurrent occurred. While a photo-enhancement does not occur as reported by Ye et al., the heterojunction no longer has a negative impact on the performance of the thin films.³² This could identify a possible structural change in either the CZTS or the CdS, returning the photocurrent. In order to determine if the CZTS/CdS PECM decrease was an artefact of a poorly deposited CZTS layer, an annealing step was added before the addition of the CdS (**Figure 5.7b**). This annealing step most likely leads to a more crystalline film with a more uniform surface area this is seen in the increased initial photoresponse. When the CZTS_a/CdS interface was created, a decrease in photocurrent occurs similarly to CZTS/CdS films. The post-processing annealing (CZTS_a/CdS_a) returns the photoresponse in a similar fashion to CZTS/CdS_a. This trend confirms that the addition of a CZTS/CdS heterojunction has similar photoresponse properties irrespective of the pre-CBD annealing. Similarly, the return in photoresponse is also concerted when annealed post-CBD, identifying a potential reversal of negative effects occurring from aqueous CBD of CdS.

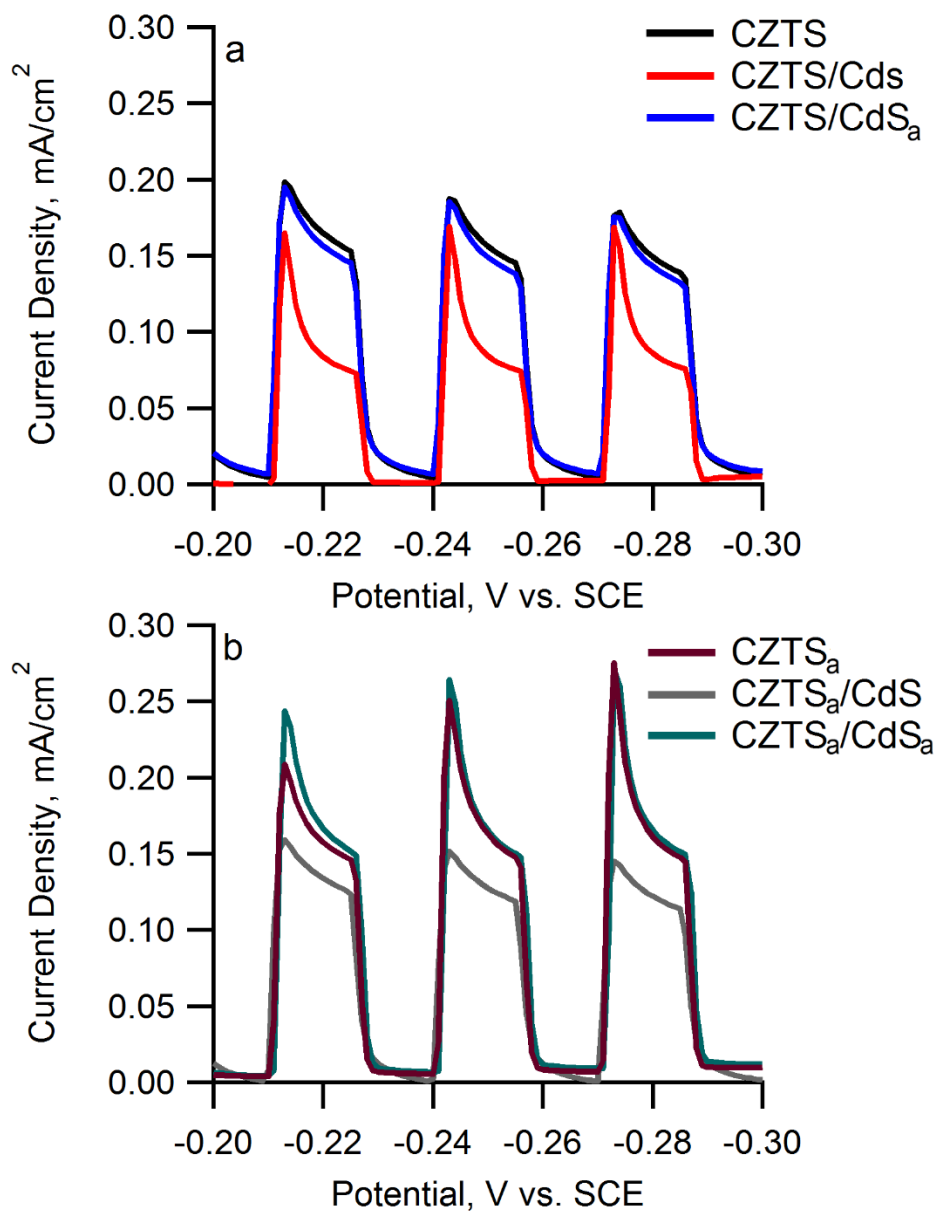


Figure 5.7 Comparative PECMs for different post-processing steps. After CdS addition the general trend is for the photocurrent to decrease. This is apparent with films deposited using a) only EPD and b) EPD with annealing (denoted by subscript a). Photocurrent returned consistently after a post-CBD annealing step

Figure 5.8 shows the Zn $L_{3,2}$ -edge on both sets of CZTS interfaces in order to identify if this change was also occurring at the atomic level. The annealed variations of the CZTS

thin films in order to identify if this trend was still apparent. The white-line absorption typically can give information on electronic structure and unoccupied densities of states with mostly s character and some d influence.⁶⁹ **Figure 5.8a** has the CZTS sample showing a weak, narrow peak above the absorption edge followed by a relatively featureless region. The CZTS/CdS heterojunction is significantly different with respect to its absorption edge as it decreased significantly in its intensity. The post-edge features of CZTS are dissimilar to the ones expressed in the CZTS/CdS sample and support a change in local environment. Upon annealing (CZTS/CdS_a), a return in the peak intensity occurs, however the long range oscillations are not congruent with the CZTS sample. This would be mostly due to a change in the crystallinity of the CZTS as a result of annealing. These long range oscillations do fit well with the annealed CZTS (CZTS_a) samples (**Figure 5.8b**). The CZTS_a absorption peak is slightly sharper in the denoting a possibly more crystalline CZTS. A similar tendency for the change in edge and post-edge features with the addition of a CdS layer (CZTS_a/CdS). The post-CBD annealing sample (CZTS_a/CdS_a) shows the most optimal return to the initial CZTS_a sample, indicating the most conserved local and long range order.

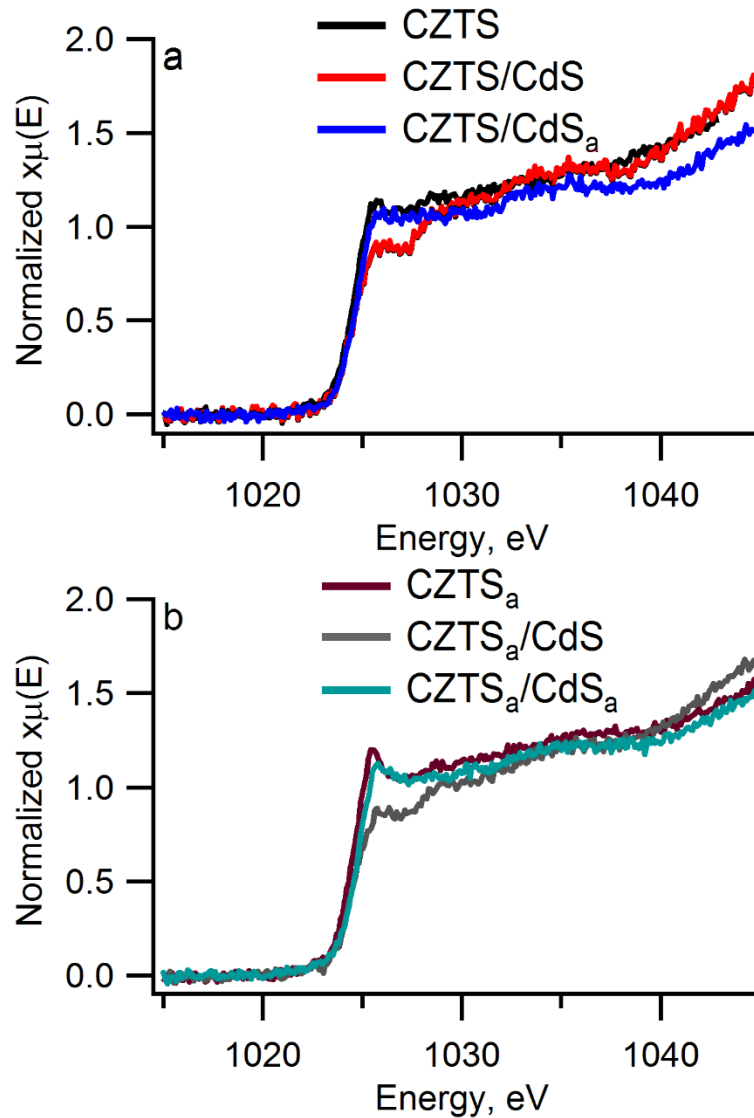


Figure 5.8 Zn $L_{3,2}$ -edge for CZTS thin films. The addition of a CdS layer decreases the intensity of the absorption peak as well as changes the shape of the near-edge absorption. The return in sharpness occurs after annealing in samples that were a) not annealed before CdS and b) samples that were annealed before the CdS addition

The Zn L_3 -edge probes the $2p_{3/2}$ electronic transition to the unoccupied electronic states.⁷⁰ These states are typically a mixture of s and d characteristics with a larger component being s due to inner valence energies below the Fermi level. The full d band in zinc also shows a broad resonance in the post absorption edge/Fermi level region.⁷¹⁻⁷³

The CZTS/CdS samples have a weaker hybridization between Zn 4s, 4p, 3d and S 3p shown through the decrease in the absorption edge intensity, which corroborates the findings from the Zn K-edge.⁷⁴⁻⁷⁵ Moreover the second broad absorption edge at approximately 1030-1035 eV could be attributed to coordination of water and the hybridization of the molecular orbitals with the valence orbitals of water molecules to form partially empty molecular orbitals. Upon X-ray absorption, these orbitals can be filled by excited p electrons.⁷⁶ A return to a similar local environment is seen after the annealing process occurs on the CdS layer. This would indicate that the effect of the CBD process on the zinc is most likely no longer a factor. These changes are also retained at higher temperatures of annealing.

5.3.5 Copper K- and L-Edge Analysis

The Cu K-edge was probed for the CZTS and CZTS/CdS samples showing no significant change with the addition of the buffer layer (**Figure 5.9**). Similarly, the Cu L_{3,2}-edge showed little variation upon the addition of the CdS with and without post-processing steps (**Figure 5.10**).

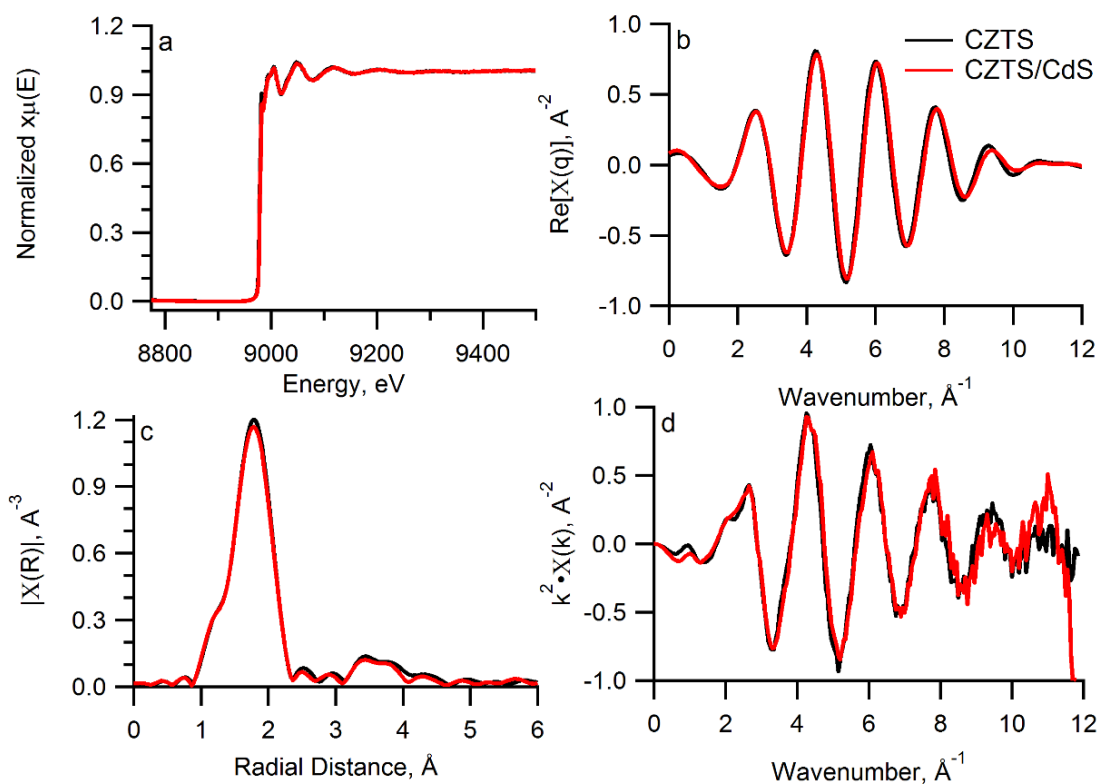


Figure 5.9 Cu K-edge data for CZTS (black) and CZTS/CdS (red) thin films a) extended absorption fine structures. b) Absorption energies converted into k^3 -space c) R space profiles of the thin films obtained after Fourier transforming using a Hanning window over k -range of 3 to 11, d) and k -space

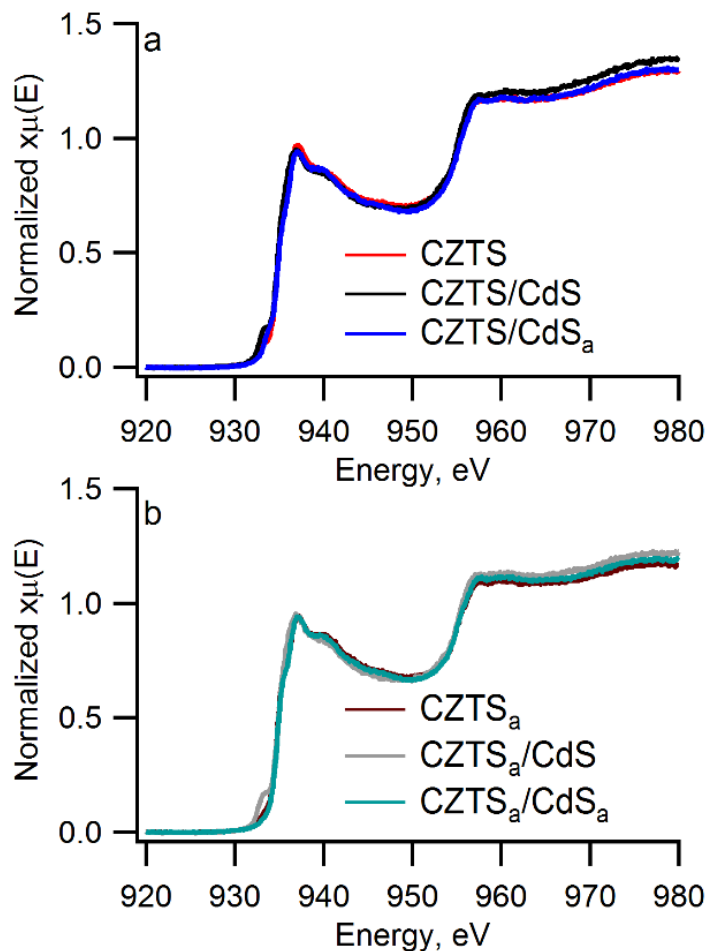


Figure 5.10 Cu $L_{3,2}$ -edge for CZTS thin films. The addition of a CdS layer decreases the intensity of the absorption peak as well as changes the shape of the near-edge absorption. The return in sharpness occurs after annealing in samples that were a) not annealed before the CdS addition

The corroboration of the EXAFS data and the PECM data allowed for an in-depth analysis of the interface for CZTS and CdS. A post-processing annealing step is most likely necessary for CZTS thin films deposited through the EPD of NCs after CdS is added. The annealing step performed before CBD only allowed for some increased photocurrent in CZTS thin films but did not change the local environment of the CZTS when a CZTS/CdS heterojunction is formed. Annealing after the addition of the CdS

changes the electronic structure of the Zn allowing for the return of photocurrent. The use of a relatively low temperature also allows for an energetically favourable procedure when considering future, large-scale processing. Additionally, the use of a single atom to accurately depict changes in local structure within the CZTS upon interfacing with other layers is of great importance for future works.

5.4 Conclusions

The CZTS/CdS heterojunction was explored through the use of photoelectrochemistry and X-ray absorption spectroscopy synchrotron radiation. It was determined that the addition of CdS through CBD reduced the photocurrent produced through the cathodic reduction of methyl viologen upon chopped illumination. Zn K- and L_{3,2}-edges show the change in local environment and indicate a coordination with something at a shortened bond length from CZTS. The decomposition of a cadmium metastable complex in the growth mechanism for CdS is most likely a cause for the coordination of water to zinc in CZTS. The use of annealing after the addition of CdS recovers the photoresponse and optimizes the local and extended structure of the CZTS at temperatures as low as 250 °C. Annealing allows for the elimination of negative effects with the addition of the CdS layer at a photoelectrochemical and physical level with the return of local structure as well as photocurrent. This could ultimately allow for a possible photovoltaic device that is both more efficient and has more longevity. Utilizing the Zn L-edge as a probe in CZTS, changes in the local structure can be seen at an interfacial level and are a critical tool for creating more efficient solar cells.

5.5 References

- (1) Shin, B.; Gunawan, O.; Zhu, Y.; Bojarczuk, N. A.; Chey, S. J.; Guha, S.; *Prog. Photovoltaics*, (2013), 21, 72-76.
- (2) McCandless, B. E.; Dobson, K. D.; *Sol. Energy*, (2004), 77, 839-856.
- (3) Harati, M.; Jia, J.; Giffard, K.; Pellarin, K.; Hewson, C.; Love, D. A.; Lau, W. M.; Ding, Z.; *Phys. Chem. Chem. Phys.*, (2010), 12, 15282-15290.
- (4) Katagiri, H.; Jimbo, K.; Maw, W. S.; Oishi, K.; Yamazaki, M.; Araki, H.; Takeuchi, A.; *Thin Solid Films*, (2009), 517, 2455-2460.
- (5) Mitzi, D. B.; Gunawan, O.; Todorov, T. K.; Wang, K.; Guha, S.; *Sol. Energ. Mat. Sol. Cells*, (2011), 95, 1421-1436.
- (6) Wang, W.; Winkler, M. T.; Gunawan, O.; Gokmen, T.; Todorov, T. K.; Zhu, Y.; Mitzi, D. B.; *Adv. Energy Mater.*, (2014), 4, 1301465 1-5.
- (7) Jackson, P.; Hariskos, D.; Wuerz, R.; Kiowski, O.; Bauer, A.; Friedlmeier, T. M.; Powalla, M.; *Phys. Status Solidi RRL*, (2015), 9, 28-31.
- (8) Yoo, H.; Kim, J.; *Sol. Energ. Mat. Sol. Cells*, (2011), 95, 239-244.
- (9) Shockley, W.; Queisser, H. J.; *J. Appl. Phys.*, (1961), 32, 510-519.
- (10) Fernandes, P. A.; Salomé, P. M. P.; da Cunha, A. F.; *Semicond. Sci. Technol.*, (2009), 24, 105013 1-7.
- (11) Azimi, H.; Hou, Y.; Brabec, C. J.; *Energy Environ. Sci.*, (2014), 7, 1829-1849.
- (12) Wang, J.; Zhang, P.; Song, X.; Gao, L.; *RSC Adv.*, (2014), 4, 27805-27810.
- (13) Pawar, S. M.; Moholkar, A. V.; Kim, I. K.; Shin, S. W.; Moon, J. H.; Rhee, J. I.; Kim, J. H.; *Curr. Appl. Phys.*, (2010), 10, 565-569.

- (14) Tsai, H. W.; Chen, C. W.; Thomas, S. R.; Hsu, C. H.; Tsai, W. C.; Chen, Y. Z.; Wang, Y. C.; Wang, Z. M.; Hong, H. F.; Chueh, Y. L.; *Sci. Rep.*, **(2016)**, *6*, 19102 1-9.
- (15) Woo, K.; Kim, Y.; Moon, J.; *Energy Environ. Sci.*, **(2012)**, *5*, 5340-5345.
- (16) Zhou, J.; You, L.; Li, S.; Yang, Y.; *Mater. Lett.*, **(2012)**, *81*, 248-250.
- (17) Yang, W.; Duan, H.-S.; Bob, B.; Zhou, H.; Lei, B.; Chung, C. H.; Li, S. H.; Hou, W. W.; Yang, Y.; *Adv. Mater.*, **(2012)**, *24*, 6323-6329.
- (18) Chen, S.; Tao, H.; Shen, Y.; Zhu, L.; Zeng, X.; Tao, J.; Wang, T.; *RSC Adv.*, **(2015)**, *5*, 6682-6686.
- (19) Zhou, H.; Hsu, W.-C.; Duan, H.-S.; Bob, B.; Yang, W.; Song, T.-B.; Hsu, C.-J.; Yang, Y.; *Energ. Environ. Sci.*, **(2013)**, *6*, 2822-2838.
- (20) Vaccarello, D.; Tapley, A.; Ding, Z.; *RSC Adv.*, **(2013)**, *3*, 3512-3515.
- (21) Tapley, A.; Vaccarello, D.; Hedges, J.; Jia, F.; Love, D. A.; Ding, Z.; *Phys. Chem. Chem. Phys.*, **(2013)**, *15*, 1431-1436.
- (22) Khoshmashrab, S.; Turnbull, M. J.; Vaccarello, D.; Nie, Y.; Martin, S.; Love, D. A.; Lau, P. K.; Sun, X.; Ding, Z.; *Electrochim. Acta*, **(2015)**, *162*, 176-184.
- (23) Turnbull, M. J.; Khoshmashrab, S.; Wang, Z.; Harbottle, R.; Sham, T.-K.; Ding, Z.; *Catal. Today*, **(2016)**, *260*, 119-125.
- (24) Vaccarello, D.; Liu, L.; Zhou, J.; Sham, T.-K.; Ding, Z.; *J. Phys. Chem. C*, **(2015)**, *119*, 11922-11928.
- (25) Perini, L.; Vaccarello, D.; Martin, S.; Jeffs, K.; Ding, Z.; *J. Electrochem. Soc.*, **(2015)**, *163*, H3110-H3115.
- (26) Courel, M.; Andrade-Arvizu, J. A.; Vigil-Galán, O.; *Solid State Electron.*, **(2015)**, *111*, 243-250.

- (27) Sim, H.; Lee, J.; Cho, S.; Cho, E.-S.; Kwon, S. J.; *J. Semicond. Tech. Sci.*, **(2015)**, *15*, 267-275.
- (28) Morkel, M.; Weinhardt, L.; Lohmüller, B.; Heske, C.; Umbach, E.; Riedl, W.; Zweigart, S.; Karg, F.; *Appl. Phys. Lett.*, **(2001)**, *79*, 4482-4484.
- (29) O'Brien, P.; McAleese, J.; *J. Mater. Chem.*, **(1998)**, *8*, 2309-2314.
- (30) Mugdur, P. H.; Chang, Y. J.; Han, S. Y.; Su, Y. W.; Morrone, A. A.; Ryu, S. O.; Lee, T. J.; Chang, C. H.; *J. Electrochem. Soc.*, **(2007)**, *154*, D482.
- (31) Voss, C.; Chang, Y. J.; Subramanian, S.; Ryu, S. O.; Lee, T. J.; Chang, C. H.; *J. Electrochem. Soc.*, **(2004)**, *151*, C655-C660.
- (32) Ye, H.; Akhavan, V. A.; Goodfellow, B. W.; Panthani, M. G.; Korgel, B. A.; Bard, A. J.; *J. Phys. Chem. C*, **(2011)**, *115*, 234-240.
- (33) Tapley, A.; Hart, C.; Vaccarello, D.; Love, D. A.; Ding, Z.; *J. Electrochem. Soc.*, **(2014)**, *161*, H725-H729.
- (34) Bär, M.; Schubert, B. A.; Marsen, B.; Wilks, R. G.; Pookpanratana, S.; Blum, M.; Krause, S.; Unold, T.; Yang, W.; Weinhardt, L.; Heske, C.; Schock, H. W.; *Appl. Phys. Lett.*, **(2011)**, *99*, 222105.
- (35) Ji, S.; Shi, T.; Qiu, X.; Zhang, J.; Xu, G.; Chen, C.; Jiang, Z.; Ye, C.; *Sci. Rep.*, **(2013)**, *3*, 2733.
- (36) Toyama, T.; Konishi, T.; Tsuji, R.; Maenishi, R.; Arata, A.; Yudate, S.; Shirakata, S.; *Phys. Status Solidi C*, **(2015)**, *12*, 721-724.
- (37) Hartman, K.; Newman, B. K.; Johnson, J. L.; Du, H.; Fernandes, P. A.; Chawla, V.; Bolin, T.; Clemens, B. M.; Cunha, A. F.; Teeter, G.; Scarpulla, M. A.; Buonassisi, T.; *IEEE Phot. Spec. Conf.*, **(2011)**.
- (38) Vayssieres, L.; Sathe, C.; Butorin, S. M.; Shuh, D. K.; Nordgren, J.; Guo, J.; *Adv. Mater.*, **(2005)**, *17*, 2320-2323.

- (39) Petty, J. T.; Sergev, O. O.; Ganguly, M.; Rankine, I. J.; Chevrier, D. M.; Zhang, P.; *J. Am. Chem. Soc.*, (2016), 138, 3469-3477.
- (40) Saravanan, K.; Kao, C. H.; Shao, Y. C.; Wang, Y. F.; Wang, B. Y.; Wang, H. T.; Tsai, C. J.; Lin, W. C.; Pao, C. W.; Tsai, H. M.; Jang, L. Y.; Lin, H. J.; Lee, J. F.; Pong, W. F.; *RSC Adv.*, (2015), 5, 19014-19019.
- (41) Just, J.; Lützenkirchen-Hecht, D.; Frahm, R.; Schorr, S.; Unold, T.; *Appl. Phys. Lett.*, (2011), 99, 262105 1-3.
- (42) Di Benedetto, F.; d'Acapito, F.; Bencistà, I.; De Luca, A.; Fornaciai, G.; Frizzera, S.; Innocenti, M.; Montegrossi, G.; Pardi, L. A.; Romanelli, M.; *Phys. Status Solidi C*, (2013), 10, 1055-1057.
- (43) Di Benedetto, F.; Cinotti, S.; Guerri, A.; De Luca, A.; Lavacchi, A.; Montegrossi, G.; Carla, F.; Felici, R.; Innocenti, M.; *ECS Trans.*, (2013), 58, 59-65.
- (44) Mendis, B. G.; Shannon, M. D.; Goodman, M. C. J.; Major, J. D.; Claridge, R.; Halliday, D. P.; Durose, K.; *Prog. Photovoltaics*, (2014), 22, 24-34.
- (45) Vaccarello, D.; Hedges, J.; Tapley, A.; Love, D. A.; Ding, Z.; *J. Electroanal. Chem.*, (2015), 738, 35-39.
- (46) Schwartz, C.; Nordlund, D.; Weng, T.-C.; Sokaras, D.; Mansfield, L.; Krishnapriyan, A. S.; Ramanathan, K.; Hurst, K. E.; Prendergast, D.; Christensen, S. T.; *Sol. Energ. Mat. Sol. Cells*, (2016), 149, 275-283.
- (47) Murali, K. R.; Thilagavathy, K.; Vasantha, S.; Gopalakrishnan, P.; Rachel Oommen, P.; *Sol. Energy*, (2010), 84, 722-729.
- (48) Ravel, B.; Newville, M.; *J. Synchrotron Radiat.*, (2005), 12, 537-41.
- (49) Teo, B. K. *EXAFS: Basic Principles and Data Analysis*; Springer: Berlin, 1986.
- (50) Teo, B. K.; Joy, D. C. *EXAFS Spectroscopy: Techniques and Applications*; Plenum Press: New York, 1981.

- (51) Newville, M.; *Rev. Mineral. Geochem.*, (2014), 78, 33-74.
- (52) Momma, K.; Izumi, F.; *J. Appl. Crystallogr.*, (2011), 44, 1272-1276.
- (53) Muhunthan, N.; Singh, O. P.; Thakur, M. K.; Karthikeyan, P.; Singh, D.; Saravanan, M.; Singh, V. N.; *J. Sol. Energy*, (2014), 2014, 1-8.
- (54) Fermin, D. J.; Duong, H. D.; Ding, Z. F.; Brevet, P. F.; Girault, H. H.; *Phys. Chem. Chem. Phys.*, (1999), 1, 1461-1467.
- (55) Siebentritt, S.; *Thin Solid Films*, (2013), 535, 1-4.
- (56) Polizzotti, A.; Repins, I. L.; Noufi, R.; Wei, S.-H.; Mitzi, D. B.; *Energy Environ. Sci.*, (2013), 6, 3171-3182.
- (57) Siah, S. C.; Chakraborty, R.; Erslev, P. T.; Sun, C.-J.; Weng, T.-C.; Toney, M. F.; Teeter, G.; Buonassisi, T.; *IEEE J. Photovolt.*, (2015), 5, 372-377.
- (58) Clark-Baldwin, K.; Tierney, D. L.; Govindaswamy, N.; Gruff, E. S.; Kim, C.; Berg, J.; Koch, S. A.; Penner-Hahn, J. E.; *J. Am. Chem. Soc.*, (1998), 120, 8401-8409.
- (59) Wei, S.-H.; Zunger, A.; *J. Appl. Phys.*, (1995), 78, 3846-3856.
- (60) Park, C. H.; Zhang, S. B.; Wei, S.-H.; *Phys. Rev. B*, (2002), 66, 073202 1-3.
- (61) Espinosa-Faller, F. J.; Conradson, D. R.; Riha, S. C.; Martucci, M. B.; Fredrick, S. J.; Vogel, S.; Prieto, A. L.; Conradson, S. D.; *J. Phys. Chem. C*, (2014), 118, 26292-26303.
- (62) Garino, C.; Borfecchia, E.; Gobetto, R.; van Bokhoven, J. A.; Lamberti, C.; *Coord. Chem. Rev.*, (2014), 277-278, 130-186.
- (63) Ohtaki, H.; Yamaguchi, T.; Maeda, M.; *B. Chem. Soc. Jpn*, (1976), 49, 701-708.
- (64) Ohtaki, H.; Radnai, T.; *Chem. Rev.*, (1993), 93, 1157-1204.

- (65) Fatmi, M. Q.; Hofer, T. S.; Randolf, B. R.; Rode, B. M.; *J. Chem. Phys.*, (2005), 123, 054514.
- (66) Chang, Y. J.; Munsee, C. L.; Herman, G. S.; Wager, J. F.; Mugdur, P.; Lee, D. H.; Chang, C. H.; *Surf. Interface Anal.*, (2005), 37, 398-405.
- (67) Kostoglou, M.; Andritsos, N.; Karabelas, A. J.; *Ind. Eng. Chem*, (2000), 39, 3272-3283.
- (68) Furlong, M. J.; Froment, M.; Bernard, M. C.; Cortes, R.; Tiwari, A. N.; Krejci, M.; Zogg, H.; Lincot, D.; *J. Cryst. Growth*, (1998), 193, 114-122.
- (69) Leapman, R. D.; Grunes, L. A.; Fejes, P. L.; *Phys. Rev. B*, (1982), 26, 614-635.
- (70) Muller, J. E.; Jepsen, O.; Wilkins, J. W.; *Solid State Commun.*, (1982), 42, 365-368.
- (71) Murphy, M. W.; Zhou, X. T.; Ko, J. Y. P.; Zhou, J. G.; Heigl, F.; Sham, T. K.; *J. Chem. Phys.*, (2009), 130, 084707 1-8.
- (72) Chiou, J. W.; Kumar, K. P. K.; Jan, J. C.; Tsai, H. M.; Bao, C. W.; Pong, W. F.; Chien, F. Z.; Tsai, M.-H.; Hong, I.-H.; Klauser, R.; Lee, J. F.; Wu, J. J.; Liu, S. C.; *Appl. Phys. Lett.*, (2004), 85, 3220-3222.
- (73) Wang, Z.; Wang, J.; Sham, T.-K.; Yang, S.; *J. Phys. Chem. C*, (2012), 116, 10375-10381.
- (74) Chen, S.; Gong, X. G.; Walsh, A.; Wei, S.; *Appl. Phys. Lett.*, (2010), 96, 021902 1-4.
- (75) Ahn, S.; Jung, S.; Gwak, J.; Cho, A.; Shin, K.; Yoon, K.; Park, D.; Cheong, H.; Yun, J. H.; *Appl. Phys. Lett.*, (2010), 97, 021905 1-3.
- (76) Lauermaun, I.; Kropp, T.; Vottier, D.; Ennaoui, A.; Eberhardt, W.; Aziz, E. F.; *Chemphyschem*, (2009), 10, 532-5.

6 Electrophoretically Deposited $\text{Cu}_2\text{ZnSnS}_4$ Thin Films as a Light Absorbing Layer in Solar Cells

Scalable methods of producing solar cells are a key component to being able to have an impact on whether they are viable for industrialization. Electrophoretic deposition (EPD) has already had success in the automotive industry and in ceramics, creating a basis for which solar cells could be manufactured in with pre-existing equipment. Successful $\text{Cu}_2\text{ZnSnS}_4$ (CZTS) film development from nanocrystal solutions can offer an alternative to high cost method currently in place for solar cell production. The formation, characterization and optimization of CZTS and CZTS/CdS films were previously optimized. The implementation of window layers ZnO and Al:ZnO have been performed using atomic layer deposition. The characteristics of a full solar cell device constructed through the layer-by-layer approach has resulted in solar cells with efficiencies of 1.28%.

6.1 Introduction

Solar energy materials are becoming increasingly popular as the need for alternative sources of energy becomes more readily apparent. Ternary and quaternary solar cells based on the $\text{CuIn}_x\text{Ga}_{(1-x)}\text{S}/\text{Se}_2$ (CIGS) archetype have gained much headway due to their increased performance and variability of their development.¹⁻⁴ Unfortunately, their reliance on materials and methods that are costly and not environmentally friendly make them unsuitable for long term global usage. $\text{Cu}_2\text{ZnSnS}_4$ (CZTS) is a p-type semiconductor with optimal 1.5 eV band gap and 10^4 cm^{-1} absorption coefficient for solar energy materials that seeks to alleviate the problems of CIGS.^{2, 5} The use of the earth-abundant elements and thin films is paramount to the desirability of CZTS-based solar cells. The utilization of hetero-junctions within a CZTS solar cell are typically comprised

of CZTS as the p-type absorber, CdS as the n-type buffer layer, i-type ZnO and aluminum doped zinc oxide (Al:ZnO, AZO) as window layers. Taking any route in creating these layers requires optimization and therefore, minor changes in the creation of one layer can lead to major changes in the next. In order to reach a balance between cost-effectiveness and efficiency, a balance of methods must be utilized.

With CZTS solar cells, the major factor playing into the efficiency and cost-effectiveness often comes with the CZTS layer itself. At present, a variety of different techniques exist to synthesize CZTS thin films. Some of these techniques include sputtering, thermal co-evaporation, pulsed laser deposition, electroplating, solution process, and solvothermal methods.⁵⁻¹² Solvothermal processing methods often allow for low temperature aspects to be included in the synthesis, and have been previously optimized.¹³⁻¹⁶ This processing has allowed for a low environmental impact approach to solar cell development with a focus on the aspect of scalability.

Utilizing a layer-by-layer approach, the formation of an FTO/CZTS/CdS/ZnO/AZO solar cell has been carefully optimized based on several different criteria. For the effectiveness of the absorbing CZTS layer, photoelectrochemical measurements (PECMs) employed a solution-phase oxidant to mimic a hetero-junction without fully processing the solar cell.^{13, 17} The interface of this material was also explored and characterized using intensity modulated photocurrent spectroscopy in order to facilitate minimal surface defects.^{14, 18} Additionally, the introduction of modifications to the CZTS/CdS heterojunction allowed for the enhancement of the photoelectrochemical response as well as the physical and structural properties of the layer (**See Chapter 5**).

In this article, a detailed performance analysis of FTO/CZTS/CdS/ZnO/AZO cell device with an efficiency of 1.28 % is reported. The cell device is analyzed by PECMs after the deposition of the CZTS and CdS layers. A detailed account of XRD peaks corresponding to CZTS kesterite phase, Raman mapping, and spectroscopy is also presented. The current density–voltage (J–V) characteristics of the device and capacitance–voltage (C–V) measurements were used to elucidate electronic properties of the cell. This is the first time a report of CZTS NCs prepared through the one-pot solvothermal approach have been incorporated into a working solar cell device.

6.2 Experimental

6.2.1 CZTS Film Preparation

The method for preparing CZTS NCs via the one-pot solvothermal method has been described elsewhere by our group.¹³ In brief, Cu(acac)₂ (Sigma-Aldrich, ≥99.9%), ZnCl₂ (Sigma-Aldrich, ≥98%), SnCl₂ (Sigma-Aldrich, 98%) were added to benzyl alcohol (BA, Alfa Aesar, ≥99%) in molar ratios of 1.44:4.02:1.00. The precursors were heated at 180 °C for two minutes to allow for the salts to fully dissolve. Thiourea (Sigma-Aldrich, ≥99%) and 2-mercapto-5-n-propylpyrimidine (MPP, Alfa Aesar, 98%) were added as the sulfur source and capping ligand at 7.5 mg/mL of BA. The reaction completed after 10 minutes. The resultant NCs were centrifuged and subsequently cleaned with isopropanol (Sigma-Aldrich, ≥99.7%) before being dried, weighed, and dispersed into isopropanol at 2 g/L. The resultant NCs had a stoichiometry of Cu_{1.8}Zn_{1.1}Sn_{1.0}S_{4.4}. The optimized NCs have a stoichiometry that is preferred for the production of high quality CZTS.^{2, 5, 8, 19-20}

The NC thin films were formed using electrophoretic deposition (EPD) with parameters previously optimized by our group.¹⁴ The setup is as follows, a standard glass beaker ($\emptyset = 4$ cm) containing the dispersion of the NCs in isopropanol. A Teflon cover held FTO coated glass slides (Sigma Aldrich with sheet resistance of $13 \Omega/\text{square}$) 0.5 cm apart and acted as the anodic working and cathodic counter electrode when attached to a power source. The films were deposited using a constant current of $0.24 \text{ mA}/\text{cm}^2$ for 40 seconds on a Keithley 2400 source meter (Tektronix, Beaverton, OR). This time and current corresponded to ~ 1 of CZTS deposition onto the FTO anode.

6.2.2 Chemical Bath Deposition (CBD) of CdS Films

CdS was deposited on the CZTS film via CBD. The bath employed was adapted from a previous method,²¹ with a 1.5 mM CdSO₄ (Fischer Scientific, 98%), 1.5 M NH₄OH (Caledon, $\geq 99\%$) and 7.5 mM thiourea (Sigma-Aldrich, $\geq 99\%$) in Milli-Q water (Millipore Corporation, $18.2 \text{ M}\Omega/\text{cm}$). The CdSO₄ and NH₄OH were stirred for approximately 30 minutes at room temperature, then heated up to 65°C and allowed to heat for 5 minutes before the addition of thiourea. The addition of thiourea was followed by lowering the CZTS thin film substrate into the solution and allowing the reaction to proceed for 10 minutes. This deposition time was optimized by us and accounted for approximately 50 nm of CdS on the top of the CZTS films.

6.2.3 Post-Process Annealing

Annealing was performed using a Thermoscientific Lindberg Blue M Tube Furnace (Asheville, NC) with a specially designed quartz tube under an inert argon atmosphere (**Chapter 5.2.3**). The tube was purged three times to ensure removal of oxygen by successively evacuating with a vacuum pump to below -200 kPa and refilling with Ar at

70 kPa. The annealing temperature was set at 250 °C, which was achieved through a ramp-up speed of 25 °C/min. At the set temperature and with the Ar pressure under 70 kPa, the annealing was processed for 50 minutes. After the annealing time was over, the furnace was opened, leaving the tube above the heating bed to cool to room temperature at a natural rate. After the tube achieved room temperature, a final vacuum-purge cycle was performed before opening the tube.

6.2.4 ZnO and Al:ZnO Atomic Layer Deposition

ZnO and Al:ZnO (AZO) were deposited using an Ultratech/CambridgeNanotech Savannah S200 ALD instrument (Waltham, MA). The deposition processes were optimized based on the manufacturer's ones. Briefly, the sample-loaded ALD chamber was pumped down to 2.6×10^{-4} atm before a purge with 5 sccm of medical grade nitrogen (Praxair, 99.999 %). The system was allowed to equilibrate for five minutes before proceeding to the deposition phase. For ZnO, deposition was carried out at a temperature of 150 °C. A cycle in the deposition consisted of alternating 0.15 s pulses of diethylzinc (Strem Chemicals, min. 95%) and Milli-Q water followed by an 8 s wait time between pulses. These alternating pulses accounted for a 1.6 Å growth/cycle of ZnO. 50 nm of ZnO were deposited onto the CdS layer. For AZO, a doping of 4.7 % was obtained through the following macrocycles. First, 10 cycles of ZnO were deposited, followed by a 0.15 s pulse of trimethylaluminum (Strem Chemicals, min. 98%), 8 s delay, 0.15 s pulse of Milli-Q water, another 8 s delay, and another 10 cycles of ZnO. Each macrocycle contributed to 33.1 Å growth/cycle of AZO. 350 nm was deposited onto the ZnO. The ALD processes were controlled by a LabVIEW program made by Ultratech/CambridgeNanotech.

6.2.5 Photoelectrochemical Measurements

Film quality was determined through the comparison of PECMs as reported by Ye et al. and our group.^{13, 21-22} Briefly, the films were immersed into a solution containing a 0.05 M methyl viologen dichloride (MV^{2+} , Sigma-Aldrich, 98%) and 0.1 M KCl (99%, Sigma Aldrich). A coiled platinum wire ($d = 0.5\text{cm}$) and a saturated calomel electrode (SCE) were used as a counter and reference electrode, respectively. The light source was a 150 W Newport lamp with an AM 1.5 D filter. A ThorLabs SC10 shutter was used to produce a square wave light stimulus to the system. A linear potential sweep was applied from 0.000 to -0.400 V at a scan rate of 0.005 Vs^{-1} using a CHI 832a electrochemical analyzer (CH Instruments, Austin TX).

6.2.6 Characterization Techniques

Scanning electron microscopy (SEM) was performed on a LEO 1540XB FIB/SEM (Zeiss, Germany). Powder X-ray diffraction (XRD) was examined on an Inel CPS Powder Diffractometer with Cu X-ray radiation source (Stratham, NH). The band gap and absorption coefficient was calculated from UV-Vis absorption spectra of the CZTS samples using a Varian Cary 50 spectrometer (Walnut Creek, CA) scanning from 1100 to 300 nm. Raman spectroscopy and mapping were collected with a LabRAM HR (Horiba Scientific, NJ, USA) spectrometer equipped with a liquid nitrogen cooled CCD. The collection of Raman backscattering at the spectrometer was focused using a pinhole opened to $200\text{ }\mu\text{m}$. All measurements were collected with a grating of 600 grooves/mm, and a 532 nm excitation source with a power output from the laser of 20 mW. A $40\times$ (NA = 0.7) microscope objective was used to collect the back scattered light. An acquisition time of 10 seconds per spectrum along with 5 accumulations was used for spot analyses.

For Raman mapping, an acquisition time of 5 seconds per spectrum at each pixel was used. The Raman maps were taken over an area of $25 \times 25 \mu\text{m}^2$, with a spectrum per pixel representing a 25×25 pixel image. Raman images were constructed by integrating the normalized intensities of characteristic Raman bands in the scan area in the X-Y orientation including a total of 625 spectra.²³ All Raman spectra are shown without a baseline correction.

Capacitance-Voltage (C-V) measurements were performed on a Keithley 2400 source meter (Tektronix, Beaverton, OR) with a measured input capacitance of 280 pF. By using current as a source and measuring the voltage as a function of time, capacitance can be measured as the product of the current and time divided by the measured voltage. The input capacitance was measured through removing the inputs and performing the same experiment with a $0.01 \mu\text{A}$ input current. The input capacitance is in parallel with the CZTS being tested and therefore is subtracted from the capacitance measured. I-V curves were measured using a 150 W Newport lamp with an AM 1.5 D filter operating at 0.7235 suns and collected using an IVIUM CompactStat (Fernandina Beach, FL).

6.3 Results and Discussion

6.3.1 PECMs

CZTS NC films made through the use of EPD were optimized based on parameters such as current density applied across electrodes, deposition time, solvent, and, NC concentration.¹⁴ The films produced through EPD were tested for their photoactivity through the use of photoelectrochemical measurements (PECMs). PECMs rely on the use of a solution-phase oxidant in order to accept electrons generated by the absorbing

layer. This current generated changes as a function of the introduction of light to the CZTS. The photoreduction of a solution-phase oxidant by the p-type CZTS film allows for an assessment and control in quality without making a full device. In fact the relative efficiency of electron capture and transport is monitored. **Figure 6.1** shows the photocurrent measurements in a linear sweep in potential for the CZTS NC thin film (black) as well as the CZTS/CdS heterojunction after annealing at 250 °C (red).

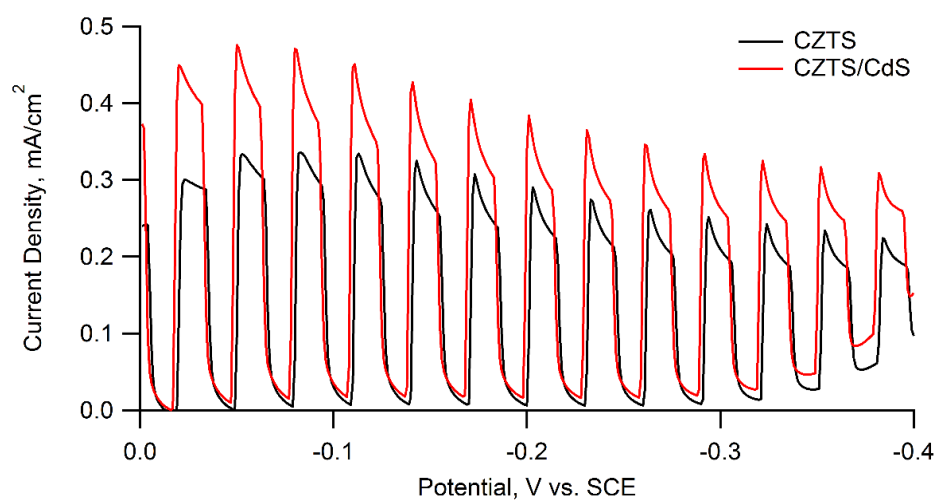


Figure 6.1 Photocurrent response of CZTS NC thin films (black) and the annealed CZTS/CdS thin films (red) along a linear sweep in potential with chopped light

When light is illuminated onto the CZTS, a flux of photons generated by light conversion occurs and electron transfer into the methyl viologen occurs. This is illustrated by a sharp increase in the current density. The electrons often transfer back into the CZTS NC thin films causing a decrease in the photocurrent. This is seen as a loss in current density after the maximum is reached. The kinetics of these photoreaction steps have been studied and quantified, identifying optimal interfacial parameters for high photoresponse films.^{14-15, 18}

The CdS buffer layer is utilized to facilitate electron transfer from the p-type layer to participate in current generation in a solar cell device.²⁴⁻²⁶ The addition of CdS has also been shown to increase photocurrent in cases of CIGSe and CISE.²¹ The deposition of CdS nanocrystals has been shown to influence not only the electrochemical properties of the thin film, but the physical properties as well (**Chapter 5**). The performance of the CZTS/CdS heterojunction has been optimized to yield higher photocurrent after the introduction of a post-process annealing step at 250 °C (**Chapter 5.3.4**). This is seen in the increase in difference between light on and light off stages. It is important to note that there is no sharp decrease or negative overshoot of photocurrent when the light turns off.¹⁵ The presence of the negative overshoot is indicative of a film with high recombination. In contrast, in the CZTS and CZTS/CdS thin films tested display a drop in current density followed by a gradual decline in photocurrent, returning to zero before subsequent illumination (**Figure 6.1**). Bulk diffusion of electrons to the surface of the liquid interface may be responsible, as photogenerated electrons deeper within the sample could overshadow the recombination effects when the light is off.²⁷ This diffusion is also more common among NC thin films owing to the path the electrons have to take in order to get to the surface.²⁷⁻²⁸ Samples with larger photoresponse were selected to continue with the addition of window layers and front contacts for the full devices as well as the continued evaluation of its properties.

6.3.2 Physical Properties of CZTS NC Solar Cells

The CZTS film was assessed using X-ray diffraction. **Figure 6.2** shows the XRD pattern for the thin films produced through EPD as well as the nanocrystals alone. Due to the anisometry and lack of directional order caused by using NCs, an increase in the

contributions from multi-scatter pathways and interference occurs, resulting in broadening.²⁹⁻³⁰ It is important to note that the EPD of the CZTS does not change the crystallinity of NCs deposition, although it has been shown to affect orientation of NCs.¹⁴

The patterns were compared against the reference data for CZTS (JCPDS # 026-0575) and were found to be in agreement with the kesterite structure. The 2θ peak values at 28.0° , 47.3° and 56.1° correspond to the (112), (200) and (312) planes of the established CZTS kesterite structure. In-depth studies of the nanocrystals produced by the synthesis have yielded a pure-phase material without the presence of common secondary phases in the detection limit (Refer to **Chapter 5**).¹⁷ The XRD patterns in **Figure 6.2** also support our previous findings of a lack of noticeable secondary phases present in the NC films.^{13,}

17

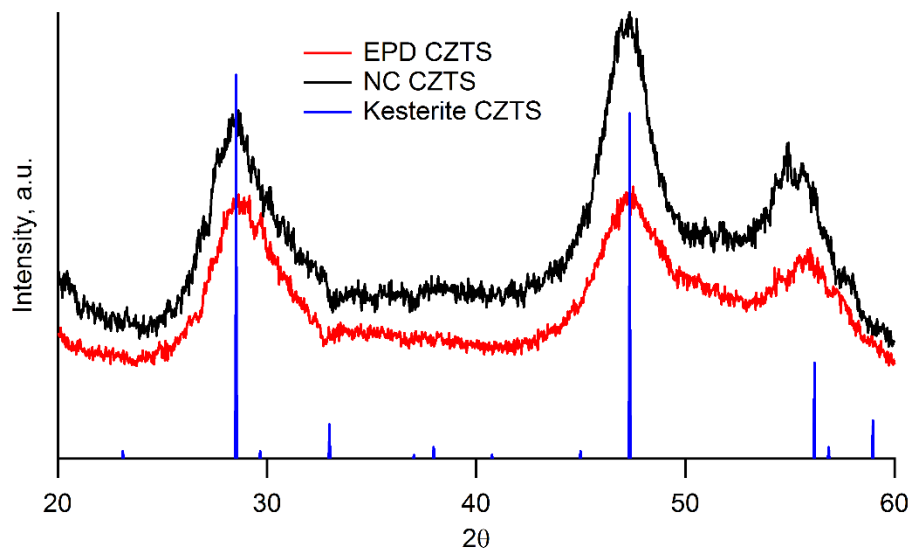


Figure 6.2 XRD pattern of EPD CZTS NC thin films (black) on FTO and NC CZTS powder (red). The JCPDS # 026-0575 shows the reference pattern obtained for pure phase kesterite CZTS (blue)

Raman spectroscopy was also performed on the thin film samples in order to identify possible secondary phases as well as map the surface chemically. The main Raman mode that is characteristic of CZTS is approximately 338 cm^{-1} .³¹⁻³² This corresponds to the *A* symmetric vibrational mode.³³ The 288 cm^{-1} peak is another common *A* symmetry mode and the 374 cm^{-1} peak is due to the *B* antisymmetric vibrational mode.³⁴⁻³⁵ A Raman map of a film area was taken. Using the sum of the normalized Raman intensities between 334 and 342 cm^{-1} an image was constructed in **Figure 6.3a**. The spots highlighted as blue and black squares on the image correspond to the two spectra shown in **Figure 6.3b**. These spots represent relatively high and low normalized counts on the map. The total normalized counts differ only slightly in intensity with a total of 6 counts for the blue-outlined pixel versus 4 for the black-outlined pixel. The spectra shown in **Figure 6.3b** indicate that these spots still contain CZTS. This would denote that the image is most likely affected to a change in physical morphology, such as the height or closeness to the detector, rather than a chemical change in the CZTS itself. All three CZTS peaks are present in both spectra and clearly corroborate the formation of CZTS.

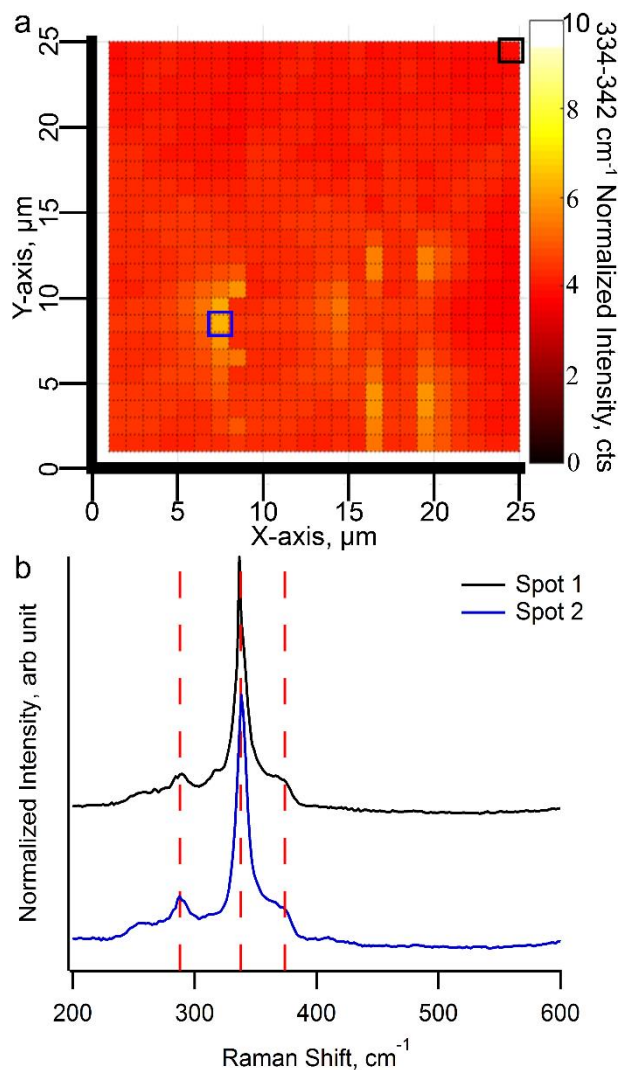


Figure 6.3 a) a 25 x 25 μm contour map of summed normalized Raman intensities between 334 and 342 cm^{-1} . b) Raman spectra of highest and lowest normalized Raman intensities from the map. The lowest summed intensity (blue) and highest (black) correspond to Spot 1 and 2 respectively

SEM was performed on a cross section of the FTO/CZTS/CdS/ZnO/AZO NC thin films (Figure 6.4a). The image shows a 1 μm thick CZTS and approximately 0.500 μm of CdS/ZnO/AZO. EDX analysis verified that Cu/(Zn+Sn) and Zn/Sn ratios were of 0.78 and 1.19 respectively. These ratios are within the range reported in literature

corresponding to optimal cell efficiency.^{2, 36} **Figure 6.4b-f** shows the EDX elemental maps for the various elements within the solar cell device.

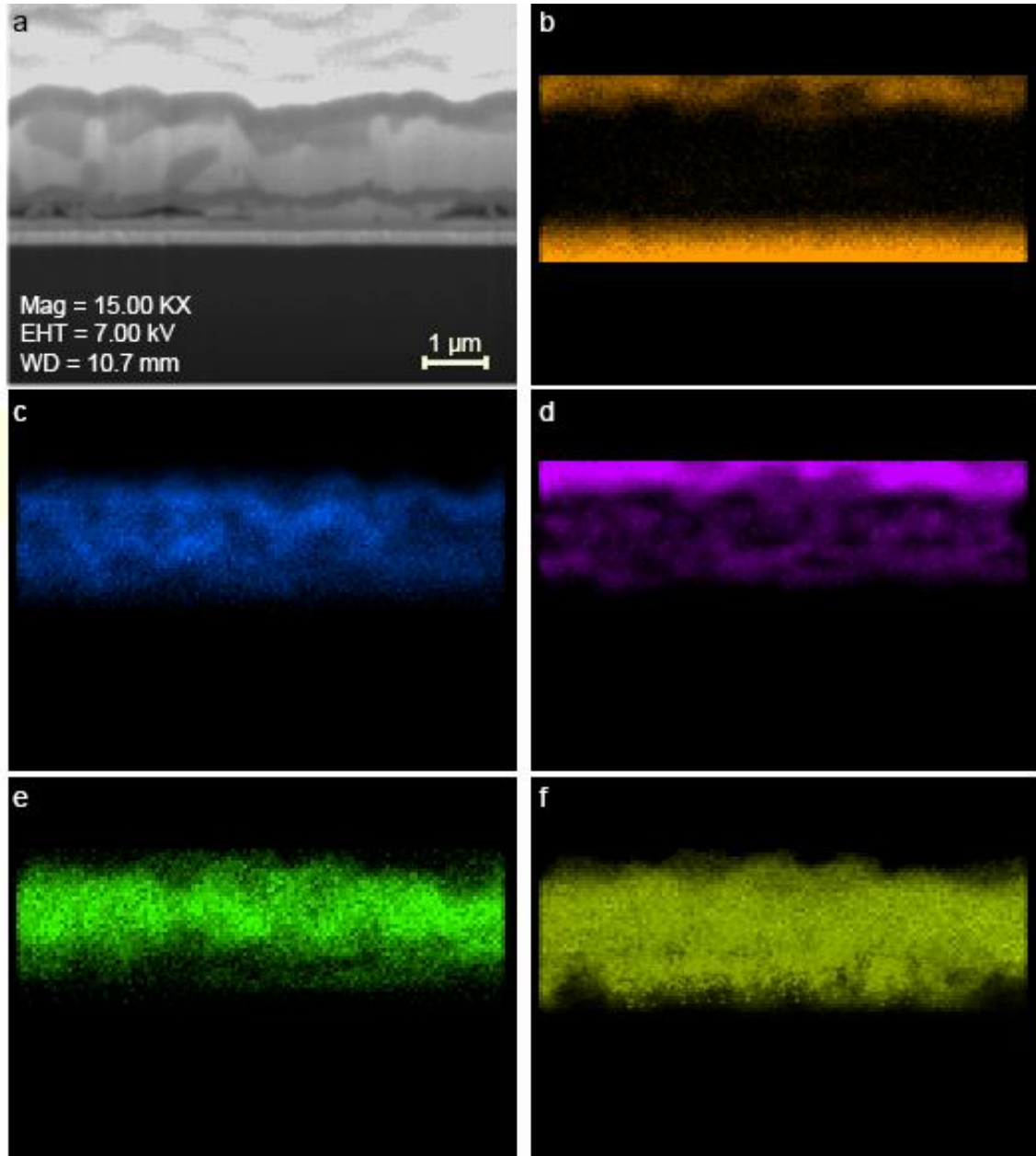


Figure 6.4 a) SEM cross-section of an FTO/CZTS/CdS/ZnO/AZO thin film solar cell b) O $K_{\alpha 1}$ map c) Cu $L_{\alpha 1,2}$ map d) Zn $L_{\alpha 1,2}$ map e) Sn $L_{\alpha 1}$ map and f) S $K_{\alpha 1}$ map

When contrasted with the cross-sectional SEM image, the EDX maps give insight into the compositional framework of the CZTS solar cells. The O $K\alpha_1$ map in **Figure 6.4b** shows the presence of oxygen in the upper, ZnO and AZO layers as well as in the FTO back contact. The lack of oxidation in the CZTS layer can be seen through the absence of intensity in the CZTS area of the O $K\alpha_1$ map. The Cu, Zn, and Sn can be seen constant throughout the film despite changes in colour and contrast seen in the SEM image (**Figure 6.4c-e**). The CdS layer can potentially be identified by the slightly larger region present in the S $K\alpha_1$ map in **Figure 6.4f**. Moreover, the ZnO and AZO are easily identified in both the SEM image as well as the Zn $L\alpha_1$ plot (**Figure 6.4d**). The precise deposition of these layers on top of varying topographical morphology are principal to the use of ALD for their deposition. The CZTS film does exhibit some gaps at the bottom of the image near the back contact however. This would identify an area that need to be improved upon for the EPD technique to be optimized further. The stability of the CZTS films despite these gaps is beneficial towards identifying EPD as a suitable candidate for deposition.

6.3.3 Absorbance Coefficient and Optical Band Gap of CZTS NC Solar Cells

For the CZTS NC thin films, the absorption coefficient was calculated to be between 4 and $6 \times 10^4 \text{ cm}^{-1}$ for 400-800 nm wavelengths (**Figure 6.5a**). A high absorption coefficient is desirable because it denotes that a small penetration depth of the visible light spectrum is needed before absorption of the photon.³⁷ A Tauc plot (**Figure 6.5b**) was constructed from the absorbance data. The band optical band gap measurements were calculated through extrapolating the linear portion of the $(\alpha h\nu)^2$ to the x-axis

between 1.7 and 2.1 eV (red). The optical band gap was determined as 1.47 eV; this matches acceptable literature values for CZTS.³⁸⁻³⁹ It should be noted that the CZTS were in nanocrystalline form and while Tauc plots assumes bulk, it has been noted that very few differences between surface and bulk exists in the NCs.¹⁷ Both the absorption coefficient and optical band gap correspond values essential for optimal photoconversion of light.^{2, 40}

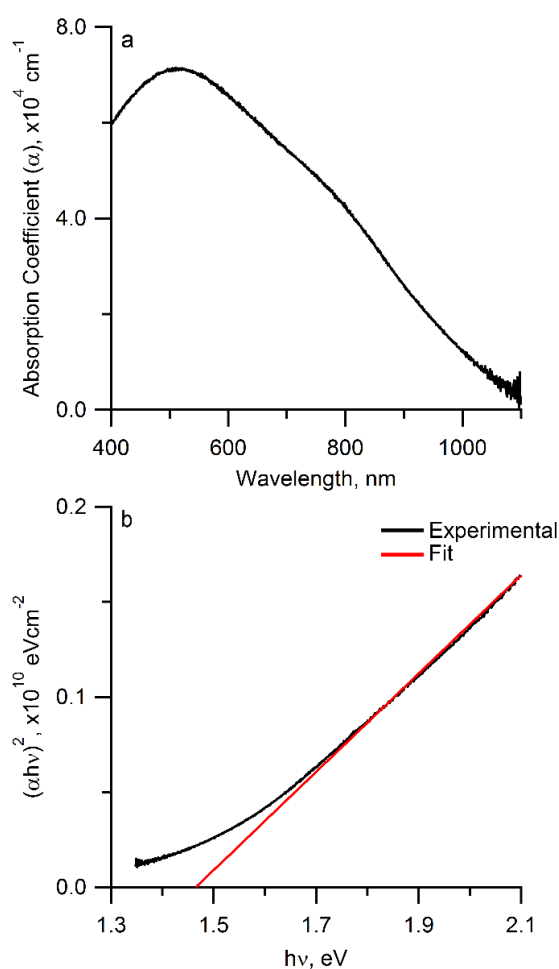


Figure 6.5 a) Absorption coefficient of the CZTS NC thin film deposited onto FTO using EPD b) Tauc plot for optical band gap measurement (black) and linear extrapolation between 1.7 and 2.1 eV (red)

6.3.4 Electrical Properties of CZTS NC Solar Cells

Some fundamental properties of the FTO/CZTS/CdS/ZnO/AZO/Ag device can be exposed through the utilization of C-V measurements. The dopant density (N_a) and built-in-charge (V_{bi}) at the junction of the solar cell can be derived using **Equations 6.1 and 6.2**.⁴¹⁻⁴²

$$\frac{1}{C^2} = \frac{2}{qN_a\epsilon_o\epsilon_sA^2}(V_{bi} - V) \quad \mathbf{6.1}$$

$$N_a = \frac{2}{q\epsilon_o\epsilon_sA^2 \left[\frac{d}{dV} \left(\frac{1}{C^2} \right) \right]} (V_{bi} - V) \quad \mathbf{6.2}$$

where q is the electron charge (1.60219×10^{-19} C), ϵ_o is the permittivity of free space (8.85×10^{-14} F/cm), ϵ_s is the dielectric constant for CZTS are based on first principle calculations (7)⁴³, A is the area of the solar cell in square centimeters, C is the measured capacitance and V is the applied DC voltage.

From these equations, the dopant density as well as the V_{bi} can be extracted from the slope and the extrapolated intercept of a $1/C^2$ vs. V plot (**Figure 6.6**). The V_{bi} of 0.56 V was slightly higher than the V_{OC} for the device measured and the N_a was measured at $3.98 \times 10^{16}/\text{cm}^3$. The depletion width (W_d) of the p-n junction was then estimated at 108 nm using V_{bi} and N_a and with **Equation 6.3**.⁴⁴⁻⁴⁵

$$W_d = (2\epsilon_o\epsilon_sV_{bi}/qN_a)^{1/2} \quad \mathbf{6.3}$$

Similarly, the carrier diffusion length (L_n) can be estimated utilizing **Equation 6.4**

$$L_n \sim \sqrt{D_n \tau} = \sqrt{\mu_n \frac{kT}{q} \tau}$$

6.4

Where τ is photogenerated electron lifetime of CZTS (3 ns), D_n is the diffusivity of electrons, kT/q is the value of thermal voltage at room temperature (25.85 mV), and μ_n is the electron mobility ($6 \text{ cm}^2/\text{Vs}$).⁴⁴⁻⁴⁵ The carrier diffusion length represents the average distance at which a photogenerated electron will travel before recombining. The calculated value of 215 nm shows that the total thickness that is contributing to the photocurrent is 323 nm ($L_n + W_d$). This suggests a relatively good collection of photogenerated electrons for over half of the CZTS NC thin film.

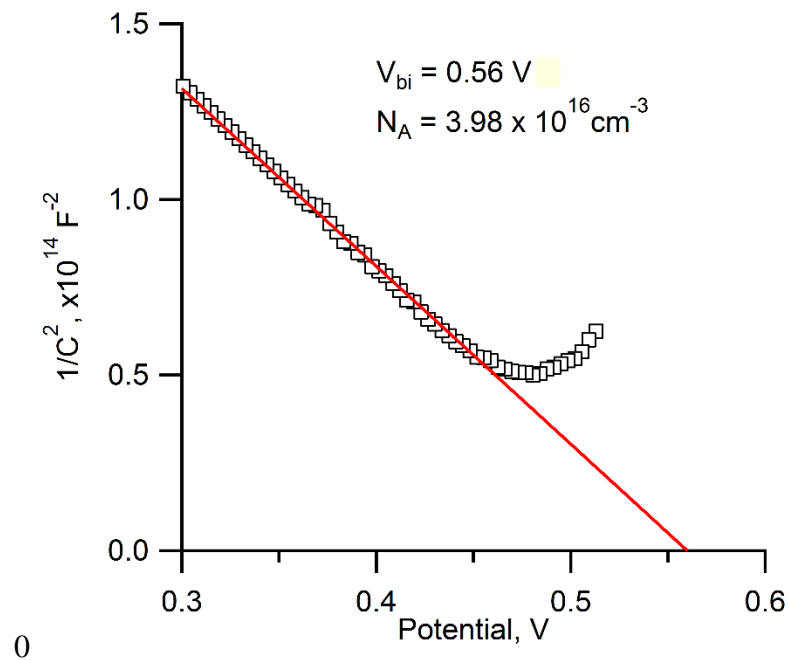


Figure 6.6 $1/C^2$ vs. potential plot obtained from a C-V measurement

Figure 6.7 shows the J-V graph of the currently optimized device assembled layer-by-layer. The efficiency of the FTO/CZTS/CdS/ZnO/AZO/Ag devices were measured at a

maximum of 1.28 %. The open circuit voltage (V_{OC}) was measured at 424 mV and the short circuit current density was 4.69 mA/cm² (I_{SC}). Series (R_S) and shunt resistances (R_{SH}) were measured to be 214.4 Ω /sq and 17.6 Ω /sq respectively. The low R_{SH} is most likely due to the CZTS/CdS layer interface which often occurs on nucleation sites of CdS growth.⁴⁶ This could be in part owing to several factors: Fermi level pinning, defects, and lattice mismatch.⁴⁷ The film most likely can provide alternative pathways for current in areas where the interface has been damaged. The statistics for the full range of efficiencies from 95 working devices can be seen in **Table 6.1**.

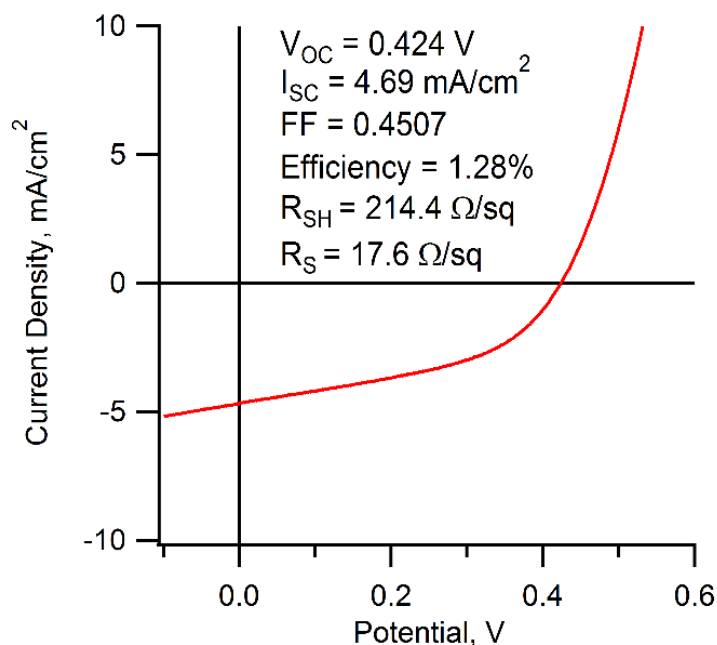


Figure 6.7 J-V curve of an ITO/CZTS/CdS/ZnO/AZO/Ag solar cell device

Table 6.1 Measurement statistics for ITO/CZTS/ZnO/AZO/Ag solar cell devices

Device Type	Voc (mV)	Isc (mA/cm ²)	FF	Efficiency (%)
Maximum	424	4.69	0.4507	1.28
Average	422 ± 1	4.37 ± 0.09	0.4179 ± 0.0021	1.01 ± 0.09
Minimum	420	3.79	0.3274	0.74

The overall performance of these solar cells is low when compared to highest laboratory efficiencies^{36, 44, 48}; however, these techniques greatly differ in the synthesis and deposition techniques applied to the creation of the devices reported. These NC solar cells operate using synthesized CZTS NCs that are applied to a substrate, removing high temperature annealing and the use of high vacuum.⁴⁹⁻⁵¹ The reported efficiencies are similar in magnitude to solar cells that are created via energy-saving routes such as laser-pulsed EPD and spin-coating.^{10, 52} The process used in this study is also reproducible and can achieve scalability due to the availability of many of these processes in industry. With this in mind, the ability to produce these solar cells on a large scale could allow them to be a viable candidate for cheaper, small scale electronics.

6.4 Conclusions

A 1.28 % efficient FTO/CZTS/CdS/ZnO/AZO/Ag solar cell device was fabricated using electrophoretic deposition of CZTS NCs synthesized via a one-pot method. The CZTS film showed a kesterite phase and a uniform deposition area. The EDX analysis confirmed Cu-poor and Zn-rich compositions. The physical, optical, and electronic properties of this unique FTO/CZTS/CdS/ZnO/AZO/Ag solar cell have been characterized and identified. Based on this information, a cheap and effective method of

manufacturing solar cell devices has become apparent based on the techniques applied towards the fabrication of this device.

6.5 References

- (1) McCandless, B. E.; Dobson, K. D.; *Sol. Energy*, (2004), 77, 839-856.
- (2) Mitzi, D. B.; Gunawan, O.; Todorov, T. K.; Wang, K.; Guha, S.; *Sol. Energ. Mat. Sol. Cells*, (2011), 95, 1421-1436.
- (3) Repins, I.; Contreras, M. A.; Egaas, B.; Dehart, C.; Scharf, J.; Perkins, C. L.; To, B.; Noufi, R.; *Prog. Photovoltaics*, (2008), 16, 235-239.
- (4) Green, M. A.; Emery, K.; Hishikawa, Y.; Warta, W.; Dunlop, E. D.; *Prog. Photovoltaics Res. Appl.*, (2013), 21, 1-11.
- (5) Katagiri, H.; Jimbo, K.; Maw, W. S.; Oishi, K.; Yamazaki, M.; Araki, H.; Takeuchi, A.; *Thin Solid Films*, (2009), 517, 2455-2460.
- (6) Fernandes, P. A.; Salomé, P. M. P.; da Cunha, A. F.; *Semicond. Sci. Technol.*, (2009), 24, 105013 1-7.
- (7) Azimi, H.; Hou, Y.; Brabec, C. J.; *Energy Environ. Sci.*, (2014), 7, 1829-1849.
- (8) Wang, J.; Zhang, P.; Song, X.; Gao, L.; *RSC Adv.*, (2014), 4, 27805-27810.
- (9) Pawar, S. M.; Moholkar, A. V.; Kim, I. K.; Shin, S. W.; Moon, J. H.; Rhee, J. I.; Kim, J. H.; *Curr. Appl. Phys.*, (2010), 10, 565-569.
- (10) Tsai, H. W.; Chen, C. W.; Thomas, S. R.; Hsu, C. H.; Tsai, W. C.; Chen, Y. Z.; Wang, Y. C.; Wang, Z. M.; Hong, H. F.; Chueh, Y. L.; *Sci. Rep.*, (2016), 6, 19102 1-9.
- (11) Woo, K.; Kim, Y.; Moon, J.; *Energy Environ. Sci.*, (2012), 5, 5340-5345.
- (12) Chen, S.; Tao, H.; Shen, Y.; Zhu, L.; Zeng, X.; Tao, J.; Wang, T.; *RSC Adv.*, (2015), 5, 6682-6686.

- (13) Vaccarello, D.; Tapley, A.; Ding, Z.; *RSC Adv.*, (2013), 3, 3512-3515.
- (14) Perini, L.; Vaccarello, D.; Martin, S.; Jeffs, K.; Ding, Z.; *J. Electrochem. Soc.*, (2015), 163, H3110-H3115.
- (15) Khoshmashrab, S.; Turnbull, M. J.; Vaccarello, D.; Nie, Y.; Martin, S.; Love, D. A.; Lau, P. K.; Sun, X.; Ding, Z.; *Electrochim. Acta*, (2015), 162, 176-184.
- (16) Turnbull, M. J.; Khoshmashrab, S.; Wang, Z.; Harbottle, R.; Sham, T.-K.; Ding, Z.; *Catal. Today*, (2016), 260, 119-125.
- (17) Vaccarello, D.; Liu, L.; Zhou, J.; Sham, T.-K.; Ding, Z.; *J. Phys. Chem. C*, (2015), 119, 11922-11928.
- (18) Vaccarello, D.; Hedges, J.; Tapley, A.; Love, D. A.; Ding, Z.; *J. Electroanal. Chem.*, (2015), 738, 35-39.
- (19) Todorov, T. K.; Reuter, K. B.; Mitzi, D. B.; *Adv. Mater.*, (2010), 22, E156-E159.
- (20) Araki, H.; Kubo, Y.; Jimbo, K.; Maw, W. S.; Katagiri, H.; Yamazaki, M.; Oishi, K.; Takeuchi, A.; *Phys. Status Solidi C*, (2009), 6, 1266-1268.
- (21) Ye, H.; Akhavan, V. A.; Goodfellow, B. W.; Panthani, M. G.; Korgel, B. A.; Bard, A. J.; *J. Phys. Chem. C*, (2011), 115, 234-240.
- (22) Tapley, A.; Vaccarello, D.; Hedges, J.; Jia, F.; Love, D. A.; Ding, Z.; *Phys. Chem. Chem. Phys.*, (2013), 15, 1431-1436.
- (23) Wang, F.; Zhou, X.; Zhou, J.; Sham, T.-K.; Ding, Z.; *J. Phys. Chem. C*, (2007), 111, 18839-18843.
- (24) Morkel, M.; Weinhardt, L.; Lohmüller, B.; Heske, C.; Umbach, E.; Riedl, W.; Zweigart, S.; Karg, F.; *Appl. Phys. Lett.*, (2001), 79, 4482-4484.
- (25) Siah, S. C.; Chakraborty, R.; Erslev, P. T.; Sun, C.-J.; Weng, T.-C.; Toney, M. F.; Teeter, G.; Buonassisi, T.; *IEEE J. Photovolt.*, (2015), 5, 372-377.

- (26) Courel, M.; Andrade-Arvizu, J. A.; Vigil-Galán, O.; *Solid State Electron.*, **(2015)**, *111*, 243-250.
- (27) Riha, S. C.; Fredrick, S. J.; Sambur, J. B.; Liu, Y.; Prieto, A. L.; Parkinson, B. A.; *ACS Appl. Mater. Interfaces*, **(2010)**, *3*, 58-66.
- (28) Peter, L. M.; *Chem. Rev.*, **(1990)**, *90*, 753-769.
- (29) Guo, Q.; Hillhouse, H. W.; Agrawal, R.; *J. Am. Chem. Soc.*, **(2009)**, *131*, 11672-11673.
- (30) Regulacio, M. D.; Ye, C.; Lim, S. H.; Bosman, M.; Ye, E.; Chen, S.; Xu, Q.-H.; Han, M.-Y.; *Chemistry*, **(2012)**, *18*, 3127-3131.
- (31) Ahmad, R.; Distaso, M.; Azimi, H.; Brabec, C. J.; Peukert, W.; *J. Nanopart. Res.*, **(2013)**, *15*, 1886 1-16.
- (32) Grossberg, M.; Krustok, J.; Raudoja, J.; Timmo, K.; Altosaar, M.; Raadik, T.; *Thin Solid Films*, **(2011)**, *519*, 7403-7406.
- (33) Grossberg, M.; Raadik, T.; Raudoja, J.; Krustok, J.; *Curr. Appl. Phys.*, **(2014)**, *14*, 447-450.
- (34) Dimitrievska, M.; Fairbrother, A.; Fontané, X.; Jawhari, T.; Izquierdo-Roca, V.; Saucedo, E.; Pérez-Rodríguez, A.; *Appl. Phys. Lett.*, **(2014)**, *104*, 021901 1-5.
- (35) Gürel, T.; Sevik, C.; Çağın, T.; *Phys. Rev. B*, **(2011)**, *84*, 205201 1-7.
- (36) Guo, Q.; Ford, G. M.; Yang, W.-C.; Walker, B. C.; Stach, E. A.; Hillhouse, H. W.; Agrawal, R.; *J. Am. Chem. Soc.*, **(2010)**, *132*, 17384-17386.
- (37) Rajkanan, K.; Singh, R.; Schewchun, J.; *Solid State Electron.*, **(1979)**, *22*, 793-795.
- (38) Tauc, J.; Grigorovici, R.; Vancu, A.; *Phys. Status Solidi B*, **(1966)**, *15*, 627-637.
- (39) Dhakal, T. P.; Peng, C.; Reid Tobias, R.; Dasharathy, R.; Westgate, C. R.; *Sol. Energy*, **(2014)**, *100*, 23-30.

- (40) Guo, L.; Zhu, Y.; Gunawan, O.; Gokmen, T.; Deline, V. R.; Ahmed, S.; Romankiw, L. T.; Deligianni, H.; *Prog. Photovoltaics*, (2014), 22, 58-68.
- (41) Tripathi, S. K.; Sharma, M.; *J. Appl. Phys.*, (2012), 111, 074513 1-10.
- (42) Yakuphanoglu, F.; *Sol. Energy*, (2011), 85, 2518-2523.
- (43) Zhao, H.; Persson, C.; *Thin Solid Films*, (2011), 519, 7508-7512.
- (44) Shin, B.; Gunawan, O.; Zhu, Y.; Bojarczuk, N. A.; Chey, S. J.; Guha, S.; *Prog. Photovoltaics*, (2013), 21, 72-76.
- (45) Sze, S. M.; Ng, K. K. *Physics of Semiconductor Devices* 3ed.; John Wiley & Sons: New Jersey, 2006.
- (46) Hasoon, F. S.; Al-Jassim, M. M.; Swartzlander, A.; Sheldon, P. In *IEEE Phot. Spec. Conf.*; 1997, p 543-546.
- (47) Tajima, S.; Kataoka, K.; Takahashi, N.; Kimoto, Y.; Fukano, T.; Hasegawa, M.; Hazama, H.; *Appl. Phys. Lett.*, (2013), 103, 243906 1-4.
- (48) Wang, W.; Winkler, M. T.; Gunawan, O.; Gokmen, T.; Todorov, T. K.; Zhu, Y.; Mitzi, D. B.; *Adv. Energy Mater.*, (2014), 4, 1301465 1-5.
- (49) Ahmed, S.; Reuter, K. B.; Gunawan, O.; Guo, L.; Romankiw, L. T.; Deligianni, H.; *Adv. Energy Mater.*, (2012), 2, 253-259.
- (50) Bag, S.; Gunawan, O.; Gokmen, T.; Zhu, Y.; Mitzi, D. B.; *Chem. Mater.*, (2012), 24, 4588-4593.
- (51) Altamura, G.; Grenet, L.; Bougerol, C.; Robin, E.; Kohen, D.; Fournier, H.; Brioude, A.; Perraud, S.; Mariette, H.; *J. Alloy. Compd.*, (2014), 588, 310-315.
- (52) Suryawanshi, M. P.; Ghorpade, U. V.; Shin, S. W.; Pawar, S. A.; Kim, I. Y.; Hong, C. W.; Wu, M.; Patil, P. S.; Moholkar, A. V.; Kim, J. H.; *ACS Appl. Mater. Interfaces*, (2016), 8, 11603-14.

7 Fabricating Low-Cost $\text{Cu}_2\text{ZnSnS}_4$ Thin Films Through Galvanostatic Electroplating and Sulfurization for Solar Cells

Having set standards for the formation of solar cells utilizing $\text{Cu}_2\text{ZnZnS}_4$ (CZTS) nanocrystals, a similar approach was undertaken to identify if the same principles could be applied to galvanostatic electrodeposition. Inexpensive CZTS films using a two-step method have been developed for use in photovoltaic devices.¹ Galvanostatic electrodeposition of precursors from environmentally friendly electrolytes and sulfurization were implemented in this method. Optimized sequential electrodepositions of Cu, Sn, and Zn films were carried out on Mo-coated glass, while the sulfurization of Mo/Cu/Sn/Zn precursors was performed at 550 °C under Ar. The CZTS films produced through this method were characterized in detail by photoelectrochemical measurements (PECMs), Raman spectroscopy, X-ray diffraction (XRD), and UV-Vis spectroscopy. However, the monitoring the Cu/(Zn+Sn) and Zn/Sn ratios allowed for morphologies of films with optimal photoresponse. Raman imaging revealed the lack of secondary phases in samples with optimal Cu/Zn/Sn ratios. The results of both XRD and Raman depicted that all CZTS films possessed kesterite structure. An optical band gap of approximately 1.45 eV for the produced CZTS film was determined from UV-Vis spectroscopy. All the measurements demonstrated that the CZTS film fabricated by galvanostatic electrodeposition meets the requirements for a light-absorbing layer and is a potential candidate in CZTS solar cells. The deposition of subsequent layers followed the same conventions as previously applied to CZTS with nanocrystals. Solar cell based on these CZTS films demonstrated that the conversion efficiency of the CZTS solar cell is 2.21 %

and photoresponse is not conserved with the methodology applied. This may now act as a basis for continued research into this area of CZTS fabrication as the potential can still be enhanced further.

7.1 Introduction

Thin film solar cells based on $\text{Cu}_2\text{ZnSnS}_4$ (CZTS) have been attracted much attention in recent years due to their composition of earth-abundant, inexpensive and environmentally friendly copper, zinc, tin and sulfur.²⁻⁵ In contrast, elements contained with $\text{CuIn}_x\text{Ga}_{(1-x)}\text{Se}_2$ or CdTe, the current leader in solar efficiencies, are either toxic, scarce, or expensive.⁶⁻⁷ CZTS is a p-type semiconductor with an optimum direct band gap of about 1.5 eV and possesses an absorption coefficient of more than 10^4 cm^{-1} .⁸ At present, the efficiency of CZTS has reached 12.6%, not only lower than those of its counterparts, CIGS and CdTe, but also much lower than its theoretical limit of ~30%.⁹⁻¹⁰ Therefore, systematic research on the preparation and characterization of CZTS films is urgently needed.

CZTS films can be prepared by a multitude of techniques such as magnetron sputtering, electrodeposition, spray pyrolysis, co-evaporation, pulse laser deposition, solution-processing, or direct nanocrystal film formation.¹¹⁻²⁷ The first two methods allow for large area deposition making them the most advanced deposition techniques for CZTS in industry. Many research groups focus on the preparation and characterization of CZTS films prepared by magnetron sputtering due to the high quality films produced and ability for in-line coatings. Fernandes *et al* reported the optimized multilayer Mo/Zn/Sn/Cu precursor prepared by sputtering and then sulfurization to form CZTS,¹² with atomic ratios of the precursors controlled by the thickness of films. The main drawback of

magnetron sputtering is the requirement of high vacuum and therefore fabrication costs are elevated and the technique is difficult to scale up. Electrodeposition is much less expensive non-vacuum method that can be considered a viable alternative. Pawar *et al* reported CZTS preparation by single step potentiostatic electrodeposition of the Cu, Zn, Sn, and S with annealing in an Ar atmosphere.²⁸ Ennaoui *et al* showed a CZTS solar cell fabrication from potentiostatic deposition of metallic Cu/Zn/Sn alloy precursors, to which sulfur was added by annealing using a gas mixture of Ar with 5 % H₂S at 550 C for 2 h.²⁹ Potentiostatic deposition of the 3-metal films with sulfurization have already been heavily detailed.³⁰⁻³¹ CZTSe film preparation via galvanostatic deposition and selenization have also been demonstrated.¹⁷ In the case of stacked metallic layers by electrodeposition, the galvanostatic mode is expected to be superior to potentiostatic mode owing to the control of the electric charge that passes through the deposition substrate.^{1, 16, 30} Furthermore, the galvanostatic mode is more suitable to scale up than potentiostatic mode to meet industrial requirements.³² The versatility of electrodeposition offers control over a wide range of parameters such as substrates, the composition, environmental impact of the electrolyte, controlled overpotentials and pH as demonstrated through the electrodeposition of copper.³³⁻³⁴ When control over morphology is less pertinent to the technique, galvanostatic deposition can be useful such as in the single step deposition of CZTS with subsequent sulfurization.¹⁷ Mechanistic investigations for the deposition of copper³⁵⁻³⁶ and other metals³⁷ can be performed with the use of potentiostatic techniques. CZTS and CZTSe devices with an efficiency of 7-8% have been produced via sulfurization or selenization of electroplated stacked metal layers or co-plated metal alloys at 585-600 °C.

In this study, the exploration of galvanostatic electrodeposition of stacked metallic films (Cu/Zn/Sn) on molybdenum-coated glass using low-cost, nontoxic and sustainable electrolytes is reported. Additionally, the application of techniques and information of layer depositions from Chapters 5-6 were applied to the electrodeposited CZTS. The demonstration of sulfurization of stacked films at 550 °C in a sealed quartz tube furnace filled with Ar are able to form CZTS photovoltaic films. These films were able to be tested for quality prior to full device construction when compared by photoelectrochemical measurements.^{26,38} The method created CZTS with the best photoresponse of 4.0 mA/cm². The characterization of the CZTS films were then described by means of scanning electron microscopy (SEM), Raman spectroscopy, X-ray diffraction (XRD), and UV-Vis spectroscopy. It is finally shown that CZTS thin film solar cell devices were fabricated with an efficiency of 2.21 % reached. While the device fabrication needs to be improved to increase the efficiency, this work emphasizes electrodeposition and sulfurization as a cost-effective strategy for CZTS thin film solar cell fabrication with a minimized negative impact to our environment and utilization of optimized standards for CZTS nanocrystals.

7.2 Experimental

7.2.1 Sample Preparation

Mo-coated glass (Guardian, Bertrange) was cleaned through sonication in a series of baths of 2% Hellmanex III detergent, deionized water, acetone, and ethanol, and finally dried with Ar gas flow.

Copper baths comprised of an electrolyte solution containing 25 g/L $\text{CuSO}_4 \cdot 5\text{H}_2\text{O}$ (99.995%, Sigma Aldrich), 120 g/L NaOH (97% pellets, Sigma-Aldrich) , and 37.5 g/L D-sorbitol ($\geq 98\%$, Sigma-Aldrich).³⁹ Sn and Zn electrolyte baths utilized methods from previous literature with slight modifications.⁴⁰ Briefly, tin baths from an environmental friendly electrolyte solution containing 100 g/L of methanesulfonic acid ($\geq 99.0\%$ Sigma-Aldrich), 35~65 g/L of stannous methanesulfonate (50% wt. in H_2O , Sigma-Aldrich), 2.86 g/L of the surfactant Empigen BB (35% active substance in H_2O , Sigma-Aldrich) and 1~3 g/L of hydroquinone ($\geq 99\%$, Sigma-Aldrich).⁴¹⁻⁴² The zinc layer was electrodeposited from a non-toxic solution containing 8 g/L of ZnCl_2 (99.999%, Sigma-Aldrich), 150 of g/L KCl ($\geq 99.0\%$, Sigma-Aldrich), 8 g/L of poly [bis(2-chloroethyl)ether-alt-1,3-bis[3-(dimethylamino)propyl-urea] (62 wt% in H_2O , Sigma-Aldrich), and 40 g/L of hydrion as a pH buffer (pH=3).

The Mo-coated glass was used as the working electrode and the metallic precursor with a stacked order of Cu/Sn/Zn was electrodeposited on this electrode. A EG&G PAR 363 potentiostat (EG&G Princeton Applied Research, Oak Ridge, TN) with a 3-electrode system were utilized to fabricate metallic precursors. The corresponding chronopotentiometry was acquired by programs written in LabVIEW (National Instruments, Austin, TX) through a computer interface (SR 245, Stanford Research, Sunnyvale, CA). The current density that passed though the working electrode was 2.5 mA/cm^2 for Cu, 6.0 mA/cm^2 for Sn and 3.0 mA/cm^2 for Zn, respectively. The atomic ratio of Cu/Sn/Zn in the precursor was controlled by electric charge consumed on the working electrode, based on the Faraday's law. After every electrodeposition, the films

were cleaned thoroughly in Milli-Q water (18.2 M Ω /sq., Milli-Q), and then dried with argon gas.

7.2.2 Sulfurization

The stacked metallic films were sulfurized in a quartz tube filled with sulfur vapor and argon gas. The sulfurization began with both sulfur powder and precursors put into a customer-made quartz tube, the ratio of mass of sulfur powder to area of precursors was fixed to 10 mg/cm². The quartz chamber was pumped down to vacuum using rotatory pump for ten minutes. The tube was then filled with Ar to 1.5 bar. This flush cycle for argon purge and pump was repeated at least three times to expel any remaining oxygen in the quartz tube. The tube was refilled with Ar with a pressure of 0.75 bar, and then heated the sulfur and precursors through a Thermoscientific Lindberg Blue M tube furnace (See Chapter 5.2.3). The temperature was ramped from room temperature to 250°C and then to 550°C at 50°C/min. The two temperatures at were held for 20 min and 30 min, respectively. After sulfurization, the CZTS films were cooled down to room temperature at a natural rate.

7.2.3 CdS, ZnO, and Al:ZnO Deposition

CdS was deposited with the same methodology as described in Chapter 5 and 6. Briefly, 1.5 mM CdSO₄ (98%, Fischer Scientific) and 1.5 M NH₄OH (\geq 99%, Caledon) were stirred for approximately 30 minutes at room temperature, then heated up to 65°C and allowed to heat for 5 minutes before the addition of 7.5 mM thiourea (\geq 99%, Sigma-Aldrich). The addition of thiourea was followed by lowering the CZTS into the solution and allowing the reaction to proceed for 10 minutes. This deposition time accounted for 50 nm of CdS on the CZTS.

Likewise, 50 nm of ZnO and 350 nm of Al:ZnO with sheet resistance of 12.3 Ω /sq were deposited through the atomic layer deposition method in Chapter 6.4

7.2.4 Characterization of Metallic Precursors and CZTS Films

The morphologies and composition of the metallic precursors and CZTS films were measured by SEM using a Hitachi S-4500 field emission microscope with an EDX system. XRD was carried out using an Inel CPS powder diffractometer with an Inel XRG 3000 Cu generator and an Inel CPS 120 detector. Photoelectrochemical measurements were performed using a 3-electrode system in 0.025 M MVCl_2 and 0.1 M KCl solution with a platinum coil and saturated calomel electrode (SCE) as counter and reference electrodes. The light source was a 150 W Newport lamp with an AM 1.5 D filter. A ThorLabs SC10 shutter was used to produce a square wave light stimulus to the system. A linear potential sweep was applied from 0.000 to -0.400 V at a scan rate of 0.005 Vs^{-1} using a CHI 832a electrochemical analyzer (CH Instruments, Austin TX).

The collection of Raman backscattering at the spectrometer was focused using a pinhole opened to 200 μm . All measurements were collected with a grating of 600 grooves/mm, and a 532 nm excitation source with a power output from the laser of 20 mW. A 40 \times (NA = 0.7) microscope objective was used to collect the back scattered light. An acquisition time of 10 seconds per spectrum along with 5 accumulations was used for spot analyses.

7.2.5 J-V Curve

In order to test the conversion efficiency of the CZTS absorber, a complete solar cell (active area 0.5 cm^2) with Mo/CZTS/CdS/ZnO/AZO/Ag layers was fabricated. A 150 W Newport lamp with an AM 1.5 D filter operating at 0.7235 suns was used as the light

source and J-V measurements were collected using an IVIUM CompactStat (Netherlands).

7.3 Results and Discussion

7.3.1 PECM Characterization

Samples were prepared by varying the thickness of individual layer of the electrodeposited metal. The relative masses (m) of the stacked films could be calculated through the use of Faraday's Law (**Equation 7.1**)

$$m/MM = \left(\frac{Q}{Fz} \right) \quad \mathbf{7.1}$$

Where Q is the electric charge passed through the working electrode, F is the Faraday constant (96485 Cmol^{-1}), MM is the molar mass of the substance in gmol^{-1} , and z is the number of electrons transferred.

The atomic ratios of the films (**Table 7.1**) were calculated based on optimal $\text{Cu}/(\text{Zn}+\text{Sn})$ and Zn/Sn ratios, 0.8 and 1.2 respectively (CZTS1). These ratios were based on the Cu-poor, Zn-rich optimal stoichiometries for CZTS that were found through RF sputtering and co-evaporation techniques.^{11, 43} The alteration of the films were done through changes in composition. The $\text{Cu}/(\text{Zn}+\text{Sn})$ ratio was changed from 0.7-1.5. The Zn/Sn ratio was also changed from 0.7-1.5. These changes in stoichiometry corresponded to changes in copper, zinc and tin content. CZTS2-Cu reflects the best working samples of the altered copper profile. CZTS3-Sn is the highest tin ratio that had PECMs. CZTS4-Zn represented the zinc content (other than 1.2) that were able to achieve photoactivity.

Table 7.1 Metallic film compositions

Sample	Cu/(Zn+Sn)	Zn/Sn
CZTS1	0.84	1.23
CZTS2-Cu	1.05	1.23
CZTS3-Sn	0.85	0.81
CZTS4-Zn	0.85	1.55

The films were compared via PECMs (**Figure 7.1**). A marked performance difference occurs between samples in their PECMs. The photocurrent of the CZTS1 and CZTS3-Sn is approximately 10 times higher than that of the CZTS2-Cu with the increased Cu content. CZTS4-Zn showed poor photoresponse and often formed visibly poor films. The photocurrent of CZTS1 by galvanostatic electrodeposition is also approximately one order of magnitude larger than that of NC CZTS by one-pot method reported in **Chapter 6**. Some of the PECMs for the samples exhibit a change in the non-zero current values when the light is off (dark current), known as band bending.^{28, 37} When the CZTS film is in contact with the MV^{2+} , the change in energy offset of the CZTS valence and conduction band structure near a junction occurs.⁴⁴ This band bending can cause the valence band to overlap with the redox potential of the MV^{2+} . The transfer of electrons from the valence band into the MV^{2+} increases the current expressed despite a lack of photogeneration. It can be seen that the dark current of CZTS1 (black) is small and near the zero line, indicating a lack of obvious band bending. However, the dark current CZTS2-Cu (blue), CZTS3-Sn (red), CZTS4-Zn (green) increases at negative potentials, indicating that some band bending may occur.

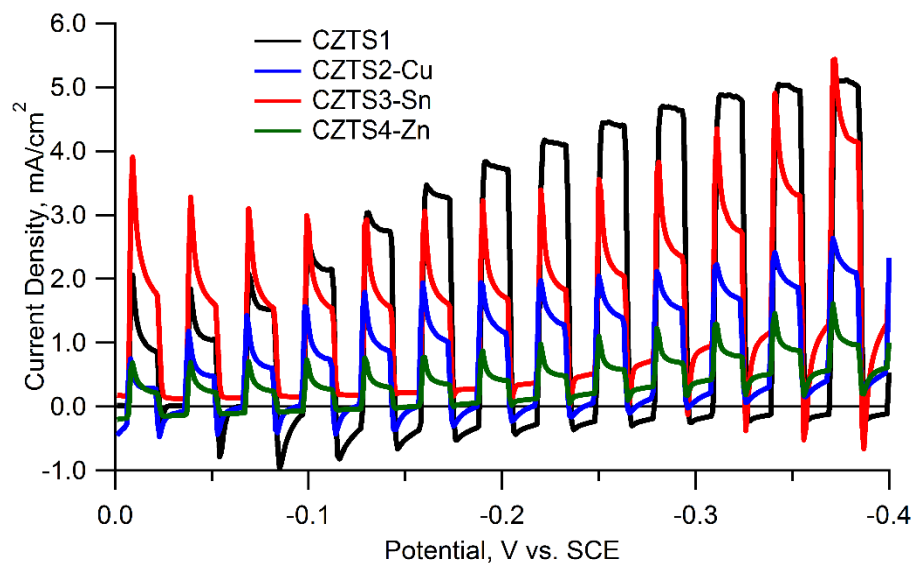


Figure 7.1 PECMs of CZTS samples with different stoichiometries

The criteria established for PECMs implies that higher photocurrent samples to be representative of better absorber layers.²⁵⁻²⁶ Based on the criteria of higher photocurrent being a requisite for efficient solar energy conversion CZTS2-Cu and CZTS3-Zn were not characterized due to their poor performance and low photoresponse (~ 2.0 and 1.5 mA/cm^2 respectively). CZTS1 and CZTS3-Sn were further distinguished to identify differences between them owing to their record photoresponse of ~ 4.0 mA/cm^2 .

7.3.2 Raman Spectroscopy of CZTS Films

Figure 7.2 shows the Raman spectroscopy results for CZTS1 (a) and CZTS3-Sn (b). The CZTS1 films were often uniform in appearance and is reflected in the average Raman spectra presented. CZTS3-Sn however, often had protrusions along the surface and were visible even at lower magnification objectives. The Raman spectrum in **Figure 7.2b** in red are characteristic Raman intensities when those protrusions were probed. The Raman spectrum in black were taken on the flat areas of the CZTS, and accounted for the

majority of the films' surface. The black dashed lines in both figures correspond to Raman peaks for CZTS referenced in the literature at 288, 338, and 378 cm^{-1} .⁴⁵⁻⁴⁶ The red dashed line matched the Raman peaks associated with SnS_2 .⁴⁷⁻⁴⁸

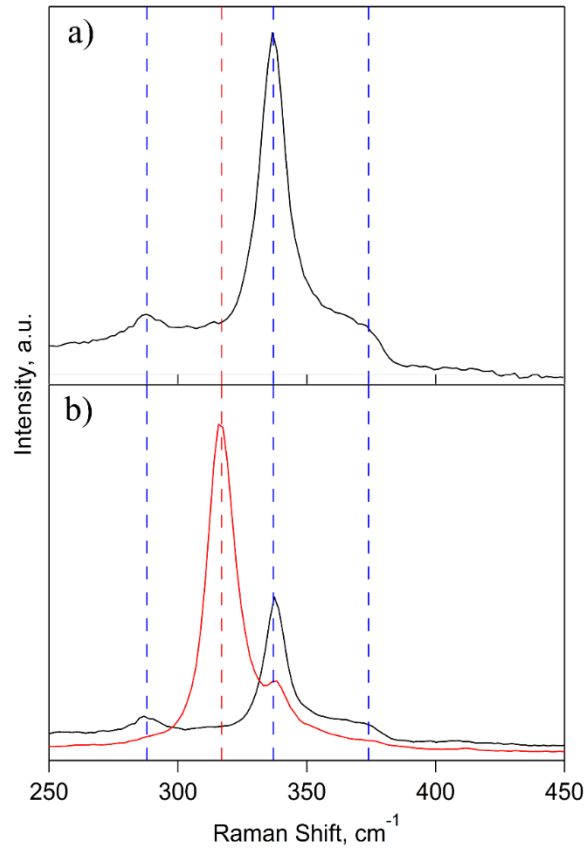


Figure 7.2 a) Average Raman spectra of CZTS1 b) Raman spectra of CZTS3-Sn taken from flat areas (black) versus protrusions (red)

The majority of the film had Raman spectra were indicative of kesterite CZTS when compared with the reference values. However, when the protrusions were examined and indicated the presence of SnS_2 , a secondary phase often related to decreases in photocurrent intensity as well as possible sources of shunts.⁴⁹ Possible reasons for the formation of this phase exist due to the low temperatures at which it can occur. At approximately 280 $^{\circ}\text{C}$, the formation of SnS_2 is preferential.⁵⁰⁻⁵¹ The synthesis has a

holding step at 250 °C that may account for this as well as be influenced by the larger Sn content. Due to this formation, the availability of sulfur to the rest of the CZTS may decrease and provide the drop in the ability to produce photocurrent and a CZTS that is sulfur deficient. These results are most likely indicative of the formation of SnS₂ in high tin environments, and despite its high PECM performance, it is not suitable for CZTS solar cells.

Following the identification of the secondary phase present in CZTS₂-Sn by Raman spectroscopy, CZTS₁ remained the best candidate in terms of purity and photoresponse. For this reason, its structural and optical properties were characterized and used as a basis for solar cell efficiency testing.

7.3.3 CZTS X-ray Diffraction Patterns

Stoichiometric CZTS films are generally difficult to obtain using two-step method, i.e. preparation of the precursor and then sulfurization, because undesired binary and/or ternary phases maybe exist in the films.³⁷

Figure 7.3 shows the X-ray diffraction pattern for CZTS₁ samples (black). The peak positions centered at 18.10°, 28.53°, 32.97°, 47.29°, 55.93° are in agreement with the pure kesterite CZTS 2θ values of the planes (101), (112), (200), (220), (312) in JCPDF 026-0575 (red), respectively. It is important to note that CZTS peaks heights are similar to the Mo (110) peak indicating a highly ordered kesterite CZTS and is in agreement with literature responses.^{11, 29, 52} From the diffraction pattern, the theoretical size of CZTS crystals can be estimated through the Scherrer equation (7.2).⁵³

$$D = \frac{K\lambda}{\beta_{1/2}\cos\theta} \quad 7.2$$

Where, K is the crystallite shape factor (0.94), λ is the wavelength of Cu $K\alpha$ X-ray, $\beta_{1/2}$ is the full width at half maximum of the selected peak, θ is the diffraction angle of the selected peak. The CZTS1 films had approximately 35 nm theoretical crystal sizes based on the (112) peak. When compared with CZTS NCs prepared in the previous chapters, a large difference in theoretical crystal size is seen. The CZTS NCs were calculated to have 2-3 nm nanocrystals.²⁶ The diffraction patterns also reveal a much more crystalline CZTS product. It may be due to these factors that the photoresponse in these samples were much larger by comparison.

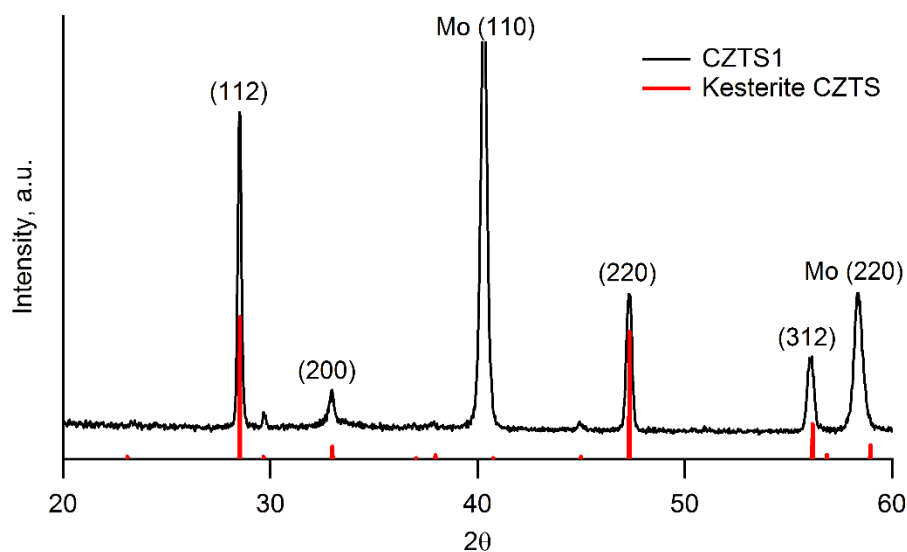


Figure 7.3 XRD patterns of Cu-rich CZTS (red), Cu-poor CZTS (black), and kesterite CZTS reference pattern JCPDS 026-0575 (red)

7.3.4 Absorbance Coefficient and Optical Band Gap

To study the band gap of CZTS1, the composition was successively fabricated on fluorine doped tin oxide (FTO) glass by galvanostatic electrodeposition and then sulfurized at 550 °C under the protective argon gas. This was done so that absorption data could be obtained through the film instead of reflected off of it. The optical properties of CZTS1 on FTO were measured via UV-Vis absorption spectroscopy.

Figure 7.4a shows the absorbance of a CZTS film as a function of wavelength of incident light. Using the absorption spectrum of CZTS, the band gap can be deduced by

Equation 7.3.⁵⁴

$$\alpha = \frac{A(h\nu - E_g)^{1/2}}{h\nu} \quad 7.3$$

where α is absorption coefficient, E_g is the band gap, and A is a constant. Extrapolation of a plot of $(\alpha h\nu)^2$ vs. $h\nu$ yields the band gap of CZTS. As shown in **Figure 7.4b**, by extrapolating the tangent line of $(\alpha h\nu)^2$ vs. $h\nu$ curve to zero, the optical band gap of CZTS is about 1.45 eV.

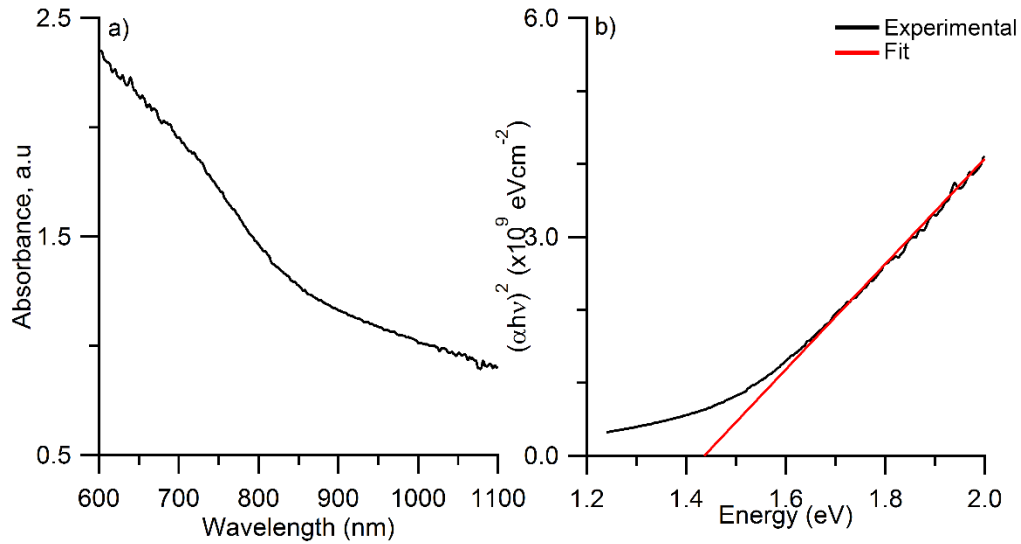


Figure 7.4 a) The plots of absorbance as a function of wavelength and $(\alpha h\nu)^2$ vs. $h\nu$ of sulfurized CZTS film at 500 °C with linear extrapolation fit

7.3.5 Solar Cell Construction

In order to investigate the effectiveness of CZTS1 fabricated by galvanostatic electrodeposition and sulfurization, the conversion efficiency of CZTS solar cell with Mo/CZTS/CdS/ZnO/AZO was evaluated. The ideal factor would be to have similar behavior to the addition of the layers and produce similar results. However, though CZTS1 had PECMs over a magnitude higher than that of CZTS NC thin films, and had a similar increase in PECM response to CdS addition, it ultimately did not transfer to efficiency measurements.

Figure 7.5 shows a typical photocurrent-potential dependence (J-V) response of the CZTS thin film solar cells constructed. The displayed open-circuit voltage (V_{oc}) is 0.486 V and short circuit current density (J_{sc}) is 5.52 mA/cm² with a fill factor (FF) of 0.456 and conversion efficiency of 2.21 %. This value was the highest obtained from over 86

working samples with CZTS1 stoichiometries. The statistics and variations in the values of the J_{SC} , V_{OC} , FF and efficiencies (η) can be seen in Error! Reference source not found..

Figure 7.5 J–V characteristic of a CZTS thin film solar cell

Table 7.2 Measurement statistics for Mo/CZTS/CdS/ZnO/AZO/Ag solar devices

Efficiency	V_{oc} (mV)	I_{sc} (mA/cm ²)	FF	Efficiency (%)
Highest	487	6.59	0.4831	2.21
Average	488 ± 1	6.54 ± 0.09	0.4076 ± 0.0011	1.87 ± 0.09
Lowest	482	6.03	0.3891	1.62

The results of the Mo/CZTS/CdS/ZnO/AZO films do not seem to be the maximum efficiencies that are possible. The PECMs indicate that a higher value is achievable, however the conditions utilized for CZTS NC solar cells are not congruent with the more crystalline films deposited through the galvanostatic electroplating. In order to maximize

the efficiencies out of this type of deposition, a similar layer-by-layer approach may have to be undertaken for these types of CZTS films as well.

7.4 Conclusions

This work shows galvanostatic electrodeposition is an attractive method suitable to fabricate high quality CZTS films for solar cells. While still in its development stages, the confirmation of high quality CZTS films has been established through PECMs.

Controlling the stoichiometry to match the ratios mentioned in the literature worked best for the galvanostatic electrodeposition. Raman images showed uniform compositions in CZTS1 samples and XRD confirmed the CZTS films possess kesterite structure consisting of about 35 nm crystals. The band gap of CZTS1 was approximately 1.45 eV and produced solar cells with an efficiency 2.21 %. While this can be improved greatly, it does indicate that the methods developed for CZTS NCs are not optimal for stacked metallic films. It does however serve as a starting point for continued studies into the CZTS produced by this method.

7.5 References

- (1) Ahmed, S.; Reuter, K. B.; Gunawan, O.; Guo, L.; Romankiw, L. T.; Deligianni, H.; *Adv. Energy Mater.*, (2012), 2, 253-259.
- (2) Wang, C.-L.; Manthiram, A.; *ACS Sustainable Chem. Eng.*, (2014), 2, 561-568.
- (3) Azimi, H.; Hou, Y.; Brabec, C. J.; *Energy Environ. Sci.*, (2014), 7, 1829-1849.
- (4) Suryawanshi, M. P.; Agawane, G. L.; Bhosale, S. M.; Shin, S. W.; Patil, P. S.; Kim, J. H.; Moholkar, A. V.; *Mater. Technol.*, (2013), 28, 98-109.
- (5) Kobayashi, T.; Jimbo, K.; Tsuchida, K.; Shinoda, S.; Oyanaoi, T.; Katagiri, H.; *Jpn. J. Appl. Phys., Part 1*, (2005), 44, 783-787.

- (6) Todorov, T. K.; Gunawan, O.; Gokmen, T.; Mitzi, D. B.; *Prog. Photovoltaics Res. Appl.*, (2013), 21, 82-87.
- (7) Jackson, P.; Wuerz, R.; Hariskos, D.; Lotter, E.; Witte, W.; Powalla, M.; *Phys. Status Solidi RRL*, (2016), DOI: 10.1002/pssr.201600199.
- (8) Hossain, M. I.; *Chalcogenide Lett.*, (2012), 9, 231-242.
- (9) Wang, W.; Winkler, M. T.; Gunawan, O.; Gokmen, T.; Todorov, T. K.; Zhu, Y.; Mitzi, D. B.; *Adv. Energy Mater.*, (2014), 4, 1301465 1-5.
- (10) Yoo, H.; Kim, J.; *Sol. Energ. Mat. Sol. Cells*, (2011), 95, 239-244.
- (11) Katagiri, H.; Jimbo, K.; Maw, W. S.; Oishi, K.; Yamazaki, M.; Araki, H.; Takeuchi, A.; *Thin Solid Films*, (2009), 517, 2455-2460.
- (12) Fernandes, P. A.; Salomé, P. M. P.; da Cunha, A. F.; *Semicond. Sci. Technol.*, (2009), 24, 105013 1-7.
- (13) Fairbrother, A.; García-Hemme, E.; Izquierdo-Roca, V.; Fontané, X.; Pulgarín-Agudelo, F. A.; Vigil-Galán, O.; Pérez-Rodríguez, A.; Saucedo, E.; *J. Am. Chem. Soc.*, (2012), 134, 8018-8021.
- (14) Scragg, J. J.; Dale, P. J.; Peter, L. M.; Zoppi, G.; Forbes, I.; *Phys. Status Solidi B*, (2008), 245, 1772-1778.
- (15) Sarswat, P. K.; Snure, M.; Free, M. L.; Tiwari, A.; *Thin Solid Films*, (2012), 520, 1694-1697.
- (16) Guo, L.; Zhu, Y.; Gunawan, O.; Gokmen, T.; Deline, V. R.; Ahmed, S.; Romankiw, L. T.; Deligianni, H.; *Prog. Photovoltaics*, (2014), 22, 58-68.
- (17) Jeon, J. O.; Lee, K. D.; Seul Oh, L.; Seo, S. W.; Lee, D. K.; Kim, H.; Jeong, J. H.; Ko, M. J.; Kim, B.; Son, H. J.; Kim, J. Y.; *ChemSusChem*, (2014), 7, 1073-7.

- (18) Deligianni, H.; Ahmed, S.; Romankiw, L. T.; *Electrochem. Soc. Interface*, (2011), 20, 47-53.
- (19) Kumar, K. Y. B.; Babu, G. S.; Bhaskar, P. U.; Raja, V. S.; *Sol. Energ. Mat. Sol. Cells*, (2009), 93, 1230-1237.
- (20) Repins, I.; Beall, C.; Vora, N.; Dehart, C.; Kuciauskas, D.; Dippo, P.; To, B.; Mann, J.; Hsu, W. C.; Goodrich, A.; Noufi, R.; *Sol. Energ. Mat. Sol. Cells*, (2012), 101, 154-159.
- (21) Pawar, S. M.; Moholkar, A. V.; Kim, I. K.; Shin, S. W.; Moon, J. H.; Rhee, J. I.; Kim, J. H.; *Curr. Appl. Phys.*, (2010), 10, 565-569.
- (22) Bag, S.; Gunawan, O.; Gokmen, T.; Zhu, Y.; Mitzi, D. B.; *Chem. Mater.*, (2012), 24, 4588-4593.
- (23) Yang, W.; Duan, H.-S.; Bob, B.; Zhou, H.; Lei, B.; Chung, C. H.; Li, S. H.; Hou, W. W.; Yang, Y.; *Adv. Mater.*, (2012), 24, 6323-6329.
- (24) Zhou, W.-H.; Jiao, J.; Zhao, Y.; Cheng, X.-Y.; Kou, D.-X.; Zhou, Z.-J.; Wu, S.-X.; *RSC Adv.*, (2014), 4, 7617-7622.
- (25) Vaccarello, D.; Liu, L.; Zhou, J.; Sham, T.-K.; Ding, Z.; *J. Phys. Chem. C*, (2015), 119, 11922-11928.
- (26) Vaccarello, D.; Tapley, A.; Ding, Z.; *RSC Adv.*, (2013), 3, 3512-3515.
- (27) Zhou, M.; Gong, Y.; Xu, J.; Fang, G.; Xu, Q.; Dong, J.; *J. Alloys Compd.*, (2013), 574, 272-277.
- (28) Pawar, S. M.; Pawar, B. S.; Moholkar, A. V.; Choi, D. S.; Yun, J. H.; Moon, J. H.; Kolekar, S. S.; Kim, J. H.; *Electrochim. Acta*, (2010), 55, 4057-4061.
- (29) Ennaoui, A.; Lux-Steiner, M.; Weber, A.; Abou-Ras, D.; Kotschau, I.; Schock, H. W.; Schurr, R.; Holzing, A.; Jost, S.; Hock, R.; Voß, T.; Schulze, J.; Kirbs, A.; *Thin Solid Films*, (2009), 519, 2300-2304.

- (30) Araki, H.; Kubo, Y.; Jimbo, K.; Maw, W. S.; Katagiri, H.; Yamazaki, M.; Oishi, K.; Takeuchi, A.; *Phys. Status Solidi C*, (2009), 6, 1266-1268.
- (31) Ge, J.; Wu, Y.; Zhang, C.; Zuo, S.; Jiang, J.; Ma, J.; Yang, P.; Chu, J.; *Appl. Surf. Sci.*, (2012), 258, 7250-7254.
- (32) Rashidi, A. M.; *J. Mater. Sci. Technol.*, (2012), 28, 1071-1076.
- (33) Maksimović, V. M.; Pavlović, L. J.; Pavlović, M. G.; Tomić, M. V.; *J. Appl. Electrochem.*, (2009), 39, 2545-2552.
- (34) Tatiparti, S. S. V.; Ebrahimi, F.; *Mater. Lett.*, (2011), 65, 2413-2415.
- (35) Nikolić, N. D.; Popov, K. I.; Pavlović, L. J.; Pavlović, M. G.; *Surf. Coat. Technol.*, (2006), 201, 560-566.
- (36) Popov, K. I.; Pavlović, M. G.; Maksimović, V. M.; *J. Appl. Electrochem.*, (1982), 12, 525-531.
- (37) Scragg, J. J., PhD Thesis, University of Bath, 2010.
- (38) Ye, H.; Akhavan, V. A.; Goodfellow, B. W.; Panthani, M. G.; Korgel, B. A.; Bard, A. J.; *J. Phys. Chem. C*, (2011), 115, 234-240.
- (39) Barbosa, L. L.; de Almeida, M. R. H.; Carlos, R. M.; Yonashiro, M.; Oliveira, G. M.; Carlos, I. A.; *Surf. Coat. Technol.*, (2005), 192, 145-153.
- (40) Scragg, J. J.; Berg, D. M.; Dale, P. J.; *J. Electroanal. Chem.*, (2010), 646, 52-59.
- (41) Gernon, M. D.; Wu, M.; Buszta, T.; Janney, P.; *Green Chem.*, (1999), 1, 127-140.
- (42) Martyak, N. M.; Seefeldt, R.; *Electrochim. Acta*, (2004), 49, 4303-4311.
- (43) Jimbo, K.; Kimura, R.; Kamimura, T.; Yamada, S.; Maw, W. S.; Araki, H.; Oishi, K.; Katagiri, H.; *Thin Solid Films*, (2007), 515, 5997-5999.

- (44) Krishnan, R., Fundamentals of Semiconductor Electrochemistry and Photoelectrochemistry. In *Encyclopedia of Electrochemistry*, Wiley-VCH Verlag GmbH & Co. KGaA: 2007.
- (45) Ahmad, R.; Distaso, M.; Azimi, H.; Brabec, C. J.; Peukert, W.; *J. Nanopart. Res.*, **(2013)**, *15*, 1886 1-16.
- (46) Grossberg, M.; Krustok, J.; Raudoja, J.; Timmo, K.; Altosaar, M.; Raadik, T.; *Thin Solid Films*, **(2011)**, *519*, 7403-7406.
- (47) Gürel, T.; Sevik, C.; Çağın, T.; *Phys. Rev. B*, **(2011)**, *84*, 205201 1-7.
- (48) Dimitrievska, M.; Fairbrother, A.; Fontané, X.; Jawhari, T.; Izquierdo-Roca, V.; Saucedo, E.; Pérez-Rodríguez, A.; *Appl. Phys. Lett.*, **(2014)**, *104*, 021901 1-5.
- (49) Patel, M.; Mukhopadhyay, I.; Ray, A.; *J. Phys. D. Appl. Phys.*, **(2012)**, *45*, 445103 1-10.
- (50) Matsushita, H.; Maeda, K.; Katsui, A.; Takizawa, T.; *J. Cryst. Growth*, **(2000)**, *208*, 416-422.
- (51) Kumar, K. S.; Manoharan, C.; Amalraj, L.; Dhanapandian, S.; Kiruthigaa, G.; Vijayakumar, K.; *Cryst. Res. Technol.*, **(2012)**, *47*, 771-779.
- (52) Tanaka, K.; Oonuki, M.; Moritake, N.; Uchiki, H.; *Sol. Energ. Mat. Sol. Cells*, **(2009)**, *93*, 583-587.
- (53) Tapley, A.; Vaccarello, D.; Hedges, J.; Jia, F.; Love, D. A.; Ding, Z.; *Phys. Chem. Chem. Phys.*, **(2013)**, *15*, 1431-1436.
- (54) Tauc, J.; Grigorovici, R.; Vancu, A.; *Phys. Status Solidi B*, **(1966)**, *15*, 627-637.

8 Concluding Remarks and Future Works

Photovoltaic cells can provide a viable alternative as a way to convert a renewable energy source like sunlight into electricity that can meet the world's increasing energy demands.¹⁻⁵ While current methods offer good energy conversion and efficiencies, they still suffer from the same setback as non-renewable sources: they on materials and methods that are not sustainable.⁶ This thesis investigated thin film chalcogenide solar cells such as $\text{Cu}_2\text{ZnSnS}_4$ and CuInS_2 (CZTS and CIS). It seeks to provide another pathway for solar energy conversion that focuses on a layer-by-layer approach while continuing to keep environmental impact in mind. The integration of different methods into the synthesis and characterization of each layer is critical for optimizing them towards a maximum efficiency.

An introduction into the concept and design of light absorbing nanocrystals and the physical and electrochemical properties contained therein are expressed in Chapter 2. This research highlights the conception of a solvothermal method for CZTS nanocrystals (NCs). It also utilizes a photoelectrochemical method of quantitation for the NCs in order to determine increased conversion of photons without full device preparation. This process allowed for economic use of resources and time in order to identify stoichiometries of CZTS that were the most beneficial. Physical characteristics of this synthesis were confirmed through the use of several analytical techniques and compared against literature values. Analogous tests were also performed on CIS NCs synthesized in the same way.⁷

Continuing with the layer-by-layer approach to the construction of these chalcogenide absorbing layers, Chapter 3 introduces the concept of the interfacial dynamic processes. These photoreactions occur simultaneously and have marked effects on the photocurrent of CIS and its properties. Through the determination of the rates of these kinetic photoreactions, it is possible to describe the interface at which an absorber performs optimally. Through enhancing and modifying the surface of the CIS, the ability to create uniform thin films with smaller magnitudes of recombination is realized. Through the successful modelling of intensity modulated photocurrent spectroscopy transients with a simple equivalent circuit, an area of analysis has been introduced that offers crucial insight into quality thin films. Likewise, the exploration and optimization of these photoreactions in CZTS thin films was also completed.⁸⁻⁹

Chapter 4 included a detailed stoichiometric analysis of CZTS NCs and related its photoelectrochemistry to physical changes present in high quality and low quality samples. Through the use of synchrotron based X-ray absorption near-edge structures, the revolving of key distinctions to high-photoresponse (hp-CZTS) and low-photoresponse (lp-CZTS) were made through the atomic probing of the Zn L-edge, S K-edge, and N K-edge. This study established that the coordination of Zn was fundamental into the presence of electron traps that reduced photocurrent response. Similarly the interaction of the capping ligand demonstrated influence over the photoresponse of the CZTS films. Lastly, the confirmation of a pure-phase CZTS was present irrespective of photoresponse. These key aspects allowed for a reconciliation between the physical characteristics of CZTS NCs produced via the one-pot synthesis and their considerable

disparity in photocurrent. Parallel studies probed similar characteristics within CIS films as well.¹⁰

The introduction of a CdS buffer layer and its effects on the physical and electrochemical properties were elucidated in Chapter 5. The application of the chemical bath deposition (CBD) technique as it had been found in literature had ultimately shown to negatively affected photocurrent for CZTS NCs made via the one-pot synthesis.¹¹⁻¹² The reduction in photocurrent was removed after a post-processing annealing step at 250 °C. These films' X-ray absorbance was measure using synchrotron radiation as an X-ray source. Extended X-ray fine structures (EXAFS) of the Zn K- and L- edge identified a discrepancy in the local structure of the Zn atoms in the CZTS when CdS was applied without annealing after. The modelling of the EXAFS spectra allowed for the identification of –OH/–OH₂ coordination with the Zn after CBD. This was found to be mostly contributed by the aqueous nature of the CBD as well as the formation and degradation of a metastable dihydroxothiourea-cadmium complex in the synthesis of CdS. This coordination and its negative effect on photocurrent was mitigated through the post-process annealing step. Although energetically unfavourable, the annealing step was carried out at the lowest possible temperature in order to return and eventually increase photocurrent.

Chapters 6 and 7 was the culmination of the previous chapters in the application of two different types of CZTS solar cells. Chapter 6 pertained to the solar cells developed through the NC route with optimized depositions for CdS, ZnO, and Al:ZnO. Chapter 7 tried to utilize the parameters for the buffer and window layers optimized via CZTS NCs and apply them towards CZTS films obtained through galvanostatic electrodeposition and

sulfurization of stacked metallic films. The structural, optical, and electronic properties of these solar cells were explored and the resultant efficiencies were recorded as 1.28 % and 2.21 % for NCs and electrodeposition respectively. It was identified that the full potential of the electrodeposited samples was not at its optimal level and that the methods developed for CZTS NCs were not conducive to highly efficient electrodeposited solar cells. Consequently, while the efficiency of the CZTS NC solar cells does not reach the same level as current highest laboratory efficiencies obtained through more energy intensive techniques, it does surpass similar CZTS NC solar cells.¹³⁻¹⁴ Both chapters however, can serve as a platform for further optimization of these types of solar cells while trying to retain the aspect of cost-effectiveness and scalability.

In order to continue the work being done on further modifying a route towards cheap sustainable solar cells, a few factors can be elucidated. Continued efforts into increasing the absorber layer efficiency through varied deposition techniques, minor stoichiometric changes, and crystal modifications are suitable options. Further discussion on the surface morphology of applied films and how they relate to efficient electron transfer across a heterojunction may also be necessary. A deeper probe into the CZTS/CdS heterojunction may give information on the large shunt resistances occurring in the final device. Being the primary cause of the lowered efficiency of the CZTS NC solar cells, the shunt resistance could be a result of uneven CdS deposition on the surface. With this in mind, further modification of the deposition technique is necessary in order to increase the efficiency of the overall solar cell. Moreover, the removal of CdS is beneficial to the environmental aspect of the solar cell itself. A Cd-free solar cell is possible with the use

of Zn(O,S) as a buffer layer.¹⁵ Utilizing Zn(O,S) as a buffer layer eliminates not only Cd but also serves as a smoother junction for the CZTS absorber and ZnO window layers.

Similarly, further development into low-cost techniques for optimized galvanostatically deposited CZTS films is also a necessity. While an improvement over CZTS NCs was apparent, a non-uniform increase in the current density was seen when PECMs were compared to final J-V characteristics. The use of industry-supplied solutions for galvanostatic plating have already shown some promise.¹⁶ The ability to reduce the probability of secondary phases and structures that lead to shunts is of the utmost importance for increasing the performance of these types of devices.

Chalcogenide solar cells have garnered increasing attention due to their prospective high-efficiency and earth-abundance.^{3, 13, 17-18} The contents of the chapters reported contain an approach heavily rooted in cost-effectiveness and scalability. Successful optimization of many of the layers present in CIS and CZTS NC solar cells have been detailed. The culmination of these optimizations has been shown in CZTS NC solar cells with efficiencies of 1.28 %. While not large in magnitude, the implications of a solar cell fashioned with energy-efficient processes are great. The cost of manufacturing solar cells is one of the main struggles facing the solar industry and a source of trepidation for large scale implementation.¹⁹ At its current status, the world's energy demand is approximately 18.5 TWy/year (one terawatt year/year is 8760 terawatt hours) and projected to increase to 28 TWy/year by 2050.²⁰ Solar irradiance striking the Earth at its maximum can provide for 23,000 TWy/year, distinguishing that efficient collection of solar energy is not as paramount as cost-effectiveness. With this in mind, the use of

CZTS NC solar cells, given further optimization and introducing more effective techniques, may be effective for larger scale implementation.

8.1 References

- (1) Siebentritt, S.; *Thin Solid Films*, (2013), 535, 1-4.
- (2) Peter, L. M.; *J. Phys. Chem. Lett.*, (2011), 2, 1861-1867.
- (3) Jackson, P.; Wuerz, R.; Hariskos, D.; Lotter, E.; Witte, W.; Powalla, M.; *Phys. Status Solidi RRL*, (2016), DOI: 10.1002/pssr.201600199.
- (4) Todorov, T. K.; Gunawan, O.; Gokmen, T.; Mitzi, D. B.; *Prog. Photovoltaics Res. Appl.*, (2013), 21, 82-87.
- (5) King, R. R.; Bhusari, D.; Larrabee, D.; Liu, X. Q.; Rehder, E.; Edmondson, K.; Cotal, H.; Jones, R. K.; Ermer, J. H.; Fetzer, C. M.; Law, D. C.; Karam, N. H.; *Prog. Photovoltaics*, (2012), 20, 801-815.
- (6) Shah, A.; Torres, P.; Tscharnner, R.; Wyrsh, N.; Keppner, H.; *Science*, (1999), 285, 692-698.
- (7) Tapley, A.; Vaccarello, D.; Hedges, J.; Jia, F.; Love, D. A.; Ding, Z.; *Phys. Chem. Chem. Phys.*, (2013), 15, 1431-1436.
- (8) Perini, L.; Vaccarello, D.; Martin, S.; Jeffs, K.; Ding, Z.; *J. Electrochem. Soc.*, (2015), 163, H3110-H3115.
- (9) Khoshmashrab, S.; Turnbull, M. J.; Vaccarello, D.; Nie, Y.; Martin, S.; Love, D. A.; Lau, P. K.; Sun, X.; Ding, Z.; *Electrochim. Acta*, (2015), 162, 176-184.
- (10) Tapley, A.; Liu, L.; Cui, X.; Zuin, L.; Love, D. A.; Zhou, J.; Sham, T.-K.; Ding, Z.; *J. Phys. Chem. C*, (2015), 119, 20967-20974.
- (11) Zhou, H.; Hsu, W.-C.; Duan, H.-S.; Bob, B.; Yang, W.; Song, T.-B.; Hsu, C.-J.; Yang, Y.; *Energ. Environ. Sci.*, (2013), 6, 2822-2838.

- (12) Ye, H.; Akhavan, V. A.; Goodfellow, B. W.; Panthani, M. G.; Korgel, B. A.; Bard, A. J.; *J. Phys. Chem. C*, (2011), 115, 234-240.
- (13) Wang, W.; Winkler, M. T.; Gunawan, O.; Gokmen, T.; Todorov, T. K.; Zhu, Y.; Mitzi, D. B.; *Adv. Energy Mater.*, (2014), 4, 1301465 1-5.
- (14) Tsai, H. W.; Chen, C. W.; Thomas, S. R.; Hsu, C. H.; Tsai, W. C.; Chen, Y. Z.; Wang, Y. C.; Wang, Z. M.; Hong, H. F.; Chueh, Y. L.; *Sci. Rep.*, (2016), 6, 19102 1-9.
- (15) Lauermann, I.; Kropp, T.; Vottier, D.; Ennaoui, A.; Eberhardt, W.; Aziz, E. F.; *Chemphyschem*, (2009), 10, 532-5.
- (16) Deligianni, H.; Ahmed, S.; Romankiw, L. T.; *Electrochem. Soc. Interface*, (2011), 20, 47-53.
- (17) Chalapathy, R. B. V.; Jung, G. S.; Ahn, B. T.; *Sol. Energ. Mat. Sol. Cells*, (2011), 95, 3216-3221.
- (18) Panthani, M. G.; Akhavan, V.; Goodfellow, B.; Schmidtke, J. P.; Dunn, L.; Dodabalapur, A.; Barbara, P. F.; Korgel, B. A.; *J. Am. Chem. Soc.*, (2008), 130, 16770-16777.
- (19) Perez, R.; Zweibel, K.; Hoff, T. E.; *Energ. Policy*, (2011), 39, 7290-7297.
- (20) Briol, F. *World Energy Outlook 2015*; International Energy Agency: Paris, 2015.

Appendices

Appendix A: Copyrights

RE: Copyrights for "Optimization of the Cu₂ZnSnS₄ nanocrystal recipe by means of photoelectrochemical measurements"

CONTRACTS-COPYRIGHT (shared) [REDACTED]

Tue 2016-07-26 5:55 AM

To: Daniel Vaccarello [REDACTED]

Dear Daniel,

Thank you for your email.

The Royal Society of Chemistry (RSC) hereby grants permission for the use of your paper(s) specified below in the printed and microfilm version of your thesis. You may also make available the PDF version of your paper(s) that the RSC sent to the corresponding author(s) of your paper(s) upon publication of the paper(s) in the following ways: in your thesis via any website that your university may have for the deposition of theses, via your university's Intranet or via your own personal website. We are however unable to grant you permission to include the PDF version of the paper(s) on its own in your institutional repository. The Royal Society of Chemistry is a signatory to the STM Guidelines on Permissions (available on request). Please note that if the material specified below or any part of it appears with credit or acknowledgement to a third party then you must also secure permission from that third party before reproducing that material.

Regards,

Antonella Tesoro
Customer Sales Support
Royal Society of Chemistry

[REDACTED]
[REDACTED]
[REDACTED]
[REDACTED]
[REDACTED]

[REDACTED]
www.rsc.org

Winner of The Queen's Awards for Enterprise, International Trade 2013



DISCLAIMER:

This communication (including any attachments) is intended for the use of the addressee only and may contain confidential, privileged or copyright material. It may not be relied upon or disclosed to any other person without the consent of the Royal Society of Chemistry. If you have received it in error, please contact us immediately. Any advice given by the Royal Society of Chemistry has been carefully formulated but is necessarily based on the information available, and the Royal Society of Chemistry

**ELSEVIER LICENSE
TERMS AND CONDITIONS**

Jul 25, 2016

This Agreement between Daniel Vaccarello ("You") and Elsevier ("Elsevier") consists of your license details and the terms and conditions provided by Elsevier and Copyright Clearance Center.

License Number	3916151344694
License date	Jul 25, 2016
Licensed Content Publisher	Elsevier
Licensed Content Publication	Journal of Electroanalytical Chemistry
Licensed Content Title	Dynamic aspects of CuInS ₂ light absorbing nanocrystal thin films
Licensed Content Author	Daniel Vaccarello, Jason Hedges, Amy Tapley, David A. Love, Zhifeng Ding
Licensed Content Date	1 February 2015
Licensed Content Volume Number	738
Licensed Content Issue Number	n/a
Licensed Content Pages	5
Start Page	35
End Page	39
Type of Use	reuse in a thesis/dissertation
Portion	full article
Format	both print and electronic
Are you the author of this Elsevier article?	Yes
Will you be translating?	No
Order reference number	
Title of your thesis/dissertation	Designing and Customizing Chalcogenide Thin Films as Light-Absorbing Layers for Photovoltaics
Expected completion date	Sep 2016
Estimated size (number of pages)	200
Elsevier VAT number	GB 494 6272 12
Requestor Location	Daniel Vaccarello [REDACTED] [REDACTED] [REDACTED] Attn: Daniel Vaccarello
Total	0.00 CAD
Terms and Conditions	



RightsLink®

Home

Account
Info

Help

ACS Publications
Most Trusted. Most Cited. Most Read.

Title: Photoelectrochemical and
Physical Insight into Cu₂ZnSnS₄
Nanocrystals Using Synchrotron
Radiation

Logged in as:
Daniel Vaccarello

LOGOUT

Author: Daniel Vaccarello, Lijia Liu, Jigang
Zhou, et al

Publication: The Journal of Physical Chemistry
C

Publisher: American Chemical Society

Date: May 1, 2015

Copyright © 2015, American Chemical Society

PERMISSION/LICENSE IS GRANTED FOR YOUR ORDER AT NO CHARGE

This type of permission/license, instead of the standard Terms & Conditions, is sent to you because no fee is being charged for your order. Please note the following:

- Permission is granted for your request in both print and electronic formats, and translations.
- If figures and/or tables were requested, they may be adapted or used in part.
- Please print this page for your records and send a copy of it to your publisher/graduate school.
- Appropriate credit for the requested material should be given as follows: "Reprinted (adapted) with permission from (COMPLETE REFERENCE CITATION). Copyright (YEAR) American Chemical Society." Insert appropriate information in place of the capitalized words.
- One-time permission is granted only for the use specified in your request. No additional uses are granted (such as derivative works or other editions). For any other uses, please submit a new request.

BACK

CLOSE WINDOW

Copyright © 2016 Copyright Clearance Center, Inc. All Rights Reserved. [Privacy statement](#). [Terms and Conditions](#).
Comments? We would like to hear from you. E-mail us at [REDACTED]

Curriculum Vitae

- Name:** Daniel Vaccarello
- Education:** The University of Toronto
Mississauga, Ontario, Canada
2006-2011 H.B.Sc.
- The University of Western Ontario
London, Ontario, Canada
2011-2016 Ph.D.
- Honours and Awards:** Ontario Graduate Scholarship
2014-2015
- Queen Elizabeth II Graduate Scholarship in Science and
Technology
2015-2016
- Dr. Joseph Soltys Graduate Award in Chemistry
2015
- ASPIRE Award for Travel to Gwangju, South Korea
2013
- Western Graduate Research Scholarship
2011-2016
- Second Prize in Poster Competition. The Electrochemical Society
Inc. Canadian Section Canadienne,
2012
- Related Work Experience** Teaching Assistant
The University of Western Ontario
2011-2016
- Patents:**
1. Ding, Z., Jia, F., Love, D., Oh, M.I., Vaccarello, D. and Tapley, A., 2015. COPPER-CONTAINING NANOCRYSTALS AND METHODS OF PREPARATION THEREFOR. U.S. Patent 9346686.

Publications:

- (1) Vaccarello, D.; Wang, J.; Ding, Z. "Electrophoretically Deposited $\text{Cu}_2\text{ZnSnS}_4$ Thin Films as a Light Absorbing Layer in Solar Cells" (2016), Submitted
- (2) Wang, X.; Vaccarello, D.; Ding, Z. "Benign Fabrication of Low-cost $\text{Cu}_2\text{ZnSnS}_4$ Photovoltaic Films by Means of Nontoxic Galvanostatic Electroplating and Sulfurization" (2016), Submitted
- (3) Vaccarello, D.; Turnbull, M.J.; Yiu, Y.-M.; Sham, T.-K.; Ding, Z. "Probing the CZTS/CdS Heterojunction Utilizing Photoelectrochemistry and X-ray Absorption Spectroscopy" (2016), Submitted
- (4) Turnbull, M.J.; Vaccarello, D.; Sham, T.-K.; Ding, Z. "Identifying Barriers to Charge-Carriers in the Bulk and Surface Regions of $\text{Cu}_2\text{ZnSnS}_4$ Films through Synchrotron-Based EXAFS" (2016), Submitted
- (5) Perini, L.; Vaccarello, D.; Martin, S.; Jeffs, K.; Ding, Z. "Cost-Effective Electrophoretic Deposition of $\text{Cu}_2\text{ZnSnS}_4$ Nanocrystals for Photovoltaic Applications" *Electrochem. Soc.*, (2016), 163, H3110-H3115
- (6) Vaccarello, D.; Liu, L.; Zhou, J.; Sham, T.-K.; Ding, Z. "Photoelectrochemical and Physical Insight into $\text{Cu}_2\text{ZnSnS}_4$ Nanocrystals Using Synchrotron Radiation" *J. Phys. Chem. C*, (2015), 119, 11922-11928
- (7) Khoshmashrab, S.; Turnbull, M.J.; Vaccarello, D.; Martin, S.; Love, D.A.; Lau, P.K.; Ding, Z. "Effects of Cu content on the photoelectrochemistry of $\text{Cu}_2\text{ZnSnS}_4$ nanocrystal thin films" *Electrochim. Acta.*, (2016), 162, 176-184
- (8) Vaccarello, D.; Hedges, J.; Tapley, A.; Love, D.A.; Ding, Z. "Dynamic Aspects of CuInS_2 Nanocrystal Films for Photovoltaic Cells" *J. Electroanal. Chem.*, (2014), 738, 35-38
- (9) Tapley, A.; Hart, C.; Vaccarello, D.; Love, D.A.; Ding, Z. "Effect of Annealing on the Photoelectrochemical Behavior of CuInS_2 Nanocrystal Films" *J. Electrochem. Soc.*, (2014), 161, H725-H729
- (10) Vaccarello, D.; Tapley, A.; Ding, Z. "Optimization of $\text{Cu}_2\text{ZnSnS}_4$ Nanocrystal Recipe by means of Photoelectrochemical Measurements" *RSC Adv.*, (2013), 3, 3512-3515
- (11) Tapley, A.; Vaccarello, D.; Hedges, J.; Jia, F.; Love, D.A.; Ding, Z. "Preparation and Characterization of CuInS_2 Nanocrystals for Photovoltaic Materials" *Phys. Chem. Chem. Phys.*, (2013), 15, 1431-1436